Magnetic Induction Tomography for Non-destructive Evaluation and Process Tomography

Ma, Lu

Award date:
2014

Awarding institution:
University of Bath

Magnetic Induction Tomography for Non-destructive Evaluation and Process Tomography

Lu Ma

A thesis submitted for the degree of Doctor of Philosophy

University of Bath

Department of Electronic and Electrical Engineering

October 2014

Declaration

Signature of Author . . . . . .
Lu Ma

Date . . . . . .
21/10/2014

Abstract

Magnetic induction tomography (MIT) is an exciting yet challenging research topic. It is sensitive to all passive electromagnetic properties, and as such it has great appeal to many industries. This thesis presents an experimental investigation of MIT within two broad areas of application: non-destructive evaluation (NDE) and industrial process tomography.

Within both areas, MIT is presented as a low cost and non-invasive inspection tool with considerable developmental potential with regard to commercial applicability. Experimental investigations into the use of MIT demonstrate its versatility in imaging conductive substances ranging from metallic structures, such as pipelines ($\sigma \approx 10^6 - 10^8 S/m$) to new composite material, such as carbon fibre reinforced polymers ($\sigma \approx 10^4 - 10^5 S/m$), as well as substances in a state of flow ($\sigma < 10 S/m$).

Research innovations presented in this thesis constitute (i) the first experimental evaluation of MIT for pipeline inspection, an application never before attempted in the area of NDE, (ii) the development of a novel limited region algorithm, which can improve the traditional resolution from 10% to 2%, (iii) the first experimental 3D planar MIT study for subsurface imaging, which opens many opportunities for MIT as a limited access tomography technique, (iv) an in-depth experimental evaluation of the MIT system response towards various fluid measurements for the first time, while also reporting some of the first flow rig tests in this field.

In addition, for each specific application, the capabilities of the prototype MIT systems are assessed with regard to (v) their flexibility in accommodating different sensor geometries, including circular, dual planar, planar and arc, (vi) situations in which the imaging subject has limited access, and (vii) their capacity to reconstruct a viable image of the subject given limited measurement data.

Altogether, the results provide an evidential basis for future exploitation of this technique. From the experimental investigations, it is concluded that the major limitations of this technique lie in both the hardware development in order to meet the standards of widespread commercial applications and the software capability for fully automated real time image reconstruction and structural analysis of the imaging subject. Nevertheless, with consistent development in both aforementioned areas, MIT could eventually be used as a rapid NDE technique for structural health monitoring and process tomography, as such contributing both to the social economy and public safety.

I lovingly dedicate this thesis to my family

and

In memory of my grandfather

Ma Chang Jian

1931–2014

Acknowledgements

I would like to offer my sincere gratitude to, firstly, my supervisor, Dr. Manuchehr Soleimani, for his consistent support, encouragement and willingness in helping me develop as an independent researcher; I am truly grateful to have experienced his tutelage and my time in his laboratory is one in which I feel I have grown significantly as an individual. Without his influence and experience, I do not feel this PhD would have been possible, and most of all, I have been inspired for the future by his enthusiasm for, and dedication to, science.

Secondly, I am indebted to David Parker and Andy Matthews, technicians at the Department of Electronic and Electrical Engineering at the University of Bath, for sharing their knowledge regarding the necessary hardware for my research; I would especially like to acknowledge David for manufacturing all the pipeline samples used in my experiments, and for his all-round assistance and support.

I would also like to thank Dr. Duncan Allsopp and Dr. Weijia Yuan for their critical feedback on my interim report.

In addition, I owe many thanks to all my friends and fellow colleagues for their help throughout this journey. I would particularly like to thank Dr. Hsin-Yu Wei, with whom I had many in-depth discussions about various research problems, and Dr. Stephen J. Bush for taking the time to proofread my manuscripts and this thesis.

Finally, I would like to thank the UK Research Centre in Non-Destructive Evaluation for a feasibility grant for pipeline inspection, the Schlumberger Foundation for awarding a Faculty for the Future fellowship, and iPhase Ltd. for research funding with regard to the two-phase flow imaging project.

Contents

List of Figures

List of Tables

List of Symbols

A	—	Magnetic potential ($V \cdot s \cdot m^{-1}$)
B	—	Magnetic flux density (T)
D	—	Electric displacement field ($C \cdot m^{-2}$)
E	—	Electric field ($V \cdot m^{-1}$)
H	—	Magnetic field strength ($A \cdot m^{-1}$)
V	—	Electric potential (V)
δ	—	Skin depth (mm)
ε	—	Electrical permittivity ($F \cdot m^{-1}$)
μ	—	Magnetic permeability ($H \cdot m^{-1}$))
σ	—	Electrical conductivity ($S \cdot m^{-1}$)
ω	—	Angular frequency (rad/s)

Nomenclature

MIT — Magnetic Induction Tomography or Mutual Inductance Tomography

NDE — Non-destrutive Evaluation

MRI — Magnetic Resonance Imaging

ECT — Electrical Capacitance Tomography

EIT — Electrical Impedance Tomography

RMIT — Rotational Magnetic Induction Tomography

VMIT — Volumetric Magnetic Induction Tomography

PMIT — Planar Magnetic Induction Tomography

FEM — Finite Element Method

LBP — Linear Back Projection

NOSER — Newton One Step Error Reconstruction

LSS — Least Squares Solution

NI — National Instrument

NPFM — Narrowband Pass Filtering Method

CFRP — Carbon Fibre Reinforced Polymer

PBRM — Pixel Based Reconstruction Method

ROI — Region of Interest

SNR — Signal to Noise Ratio

CMOS — Complementary Metal-Oxide-Semiconductor

ADC — Analog to Digital Converter

DAC — Digital to Analog Converter

EC — Eddy Current

MFL — Magnetic Flux Leakage

RFT — Remote Field Testing

UI — Ultrasonic Inspection

EMAT — Electromagnetic Acoustic Transducer

ILI — In-Line Inspection

MPT — Magneto-static Permeability Tomography

Chapter 1

Introduction

1.1 Background

Tomography is a technique for displaying a cross-sectional representation of an object through the use of penetrating signals such as waves, electromagnetic fields or particles. Tomographic techniques are often divided into different categories according to the sensing techniques used. There are two main categories of tomographic technique, hard and soft field tomography [1]. The commonly used hard field tomography techniques include $\gamma - ray$, $X - ray$ and magnetic resonance imaging (MRI). The soft field tomographic techniques are primarily referred to as electrical tomography [2]. They differ in that, for hard field tomography, the path of the transmitting signal is in a straight line and the only factor that can affect the signal strength is the material along that path, regardless of position. In soft field tomography, the position of the material in the measuring region and the distribution of electrical parameters both inside and outside the measuring region can affect the transmitting signal. Each tomographic technique has its own characteristics, constraints and applications. There are also other tomography techniques, such as ultrasound, thermal conduction tomography, that are neither hard nor soft field, and use other sensing techniques for imaging.

Technique	Characteristics	Applications
$\gamma - ray$	Fast scanning speed Radioactive sources Potentially fast	Industrial applications Medical imaging
$X - ray$	High resolution Mechanically scanned Radiation confinement	Industrial applications Medical imaging
MRI	No use of radiation Detailed resolution Non-invasive	Medical diagnosis Clinical imaging

Table 1.1: Existing hard field tomographic techniques.

Electrical tomography techniques can image the passive electromagnetic properties of an object. In 1912, Conrad Schlumberger conducted the first electric field imaging experiment; which offered new possibilities for exploring the Earth. Over the past 100 years, electrical tomography has expanded to include work in the fields of geophysics, medical imaging and process tomography. Electrical tomography techniques have several advantages. Despite their relatively modest image resolution, they have gradually proved to be useful because of their imaging speed, low cost and non-invasive characteristics [3]. Three electrical imaging techniques are listed in Table 1.2 with their sensing techniques and applications.

Electrical Impedance Tomography (EIT) utilises multiple electrode sensors to measure the impedance changes between pairs of electrodes. The conductivity distribution of the imaging subject can then be computed based on the measured impedance changes [4]. EIT is sometimes also called electrical resistance tomography, if the reactive capacitive component of the measured impedance is negligible. Among the electrical imaging techniques, EIT is the most well-developed technique and has been applied in medical imaging as a diagnostic method [5].

Compared to the traditional electrode based technique, Electrical Capacitance Tomography (ECT) realises a contactless means of mapping the dielectric permittivity through the use of capacitive sensors [6]. Typical materials that can be imaged by ECT include plastic, water and wood. Its use has been proposed for numerous applications, including flame visualisation [7, 8, 9], visualisation of fluidised bed gas-solid concentration distributions [10], and two-phase flow identification [11, 12].

Magnetic Induction Tomography (MIT), also known as Mutual Inductance Tomography or Electromagnetic Induction Tomography (EMT), is a tomographic technique that can potentially map the distribution of all passive electromagnetic properties (conductivity, permeability and permittivity) of an object [3]. MIT is the most recent and least developed electrical imaging technique, compared to EIT and ECT. MIT does not require electrical contacts with the object and uses the interaction of an oscillating magnetic field with a conductive medium. This field, which is excited and registered by inductive coils arranged around the object, is perturbed by the generation of eddy currents in the object. The conductivity (and/or other passive electromagnetic properties) can be reconstructed from the measurements of perturbed fields outside the objects. MIT has been applied to a variety of diverse applications, but most of this interest has been in either medical imaging [13, 14, 15, 16], examining cross-sectional images of the human body [17], or in non-destructive evaluations (NDE) for industrial applications, to visualise and monitor the distribution of material in vessels and pipelines [18, 19, 20].

Technique	Sensors Measurement	Property	Applications
EIT	Electrodes Impedance	σ	Medical imaging Flow imaging
ECT	Capacitive plates Capacitance	ε	Flow imaging Flaw detection
MIT	Inductive coils Mutual inductance	σ, μ, ε	Medical imaging Industrial applications

Table 1.2: Existing soft field tomographic techniques.

1.2 Aims and Objectives

The aim of this study is to investigate the feasibility and sensitivity of MIT for non-destructive evaluation (NDE) and industrial process imaging. MIT is sensitive to electrical conductivity. As such it can be used for defect inspection of metallic and new composite materials. In addition, conductive flow in multiphase flow imaging is a challenging topic as the existing techniques either do not distinguish the conductivity property or require close contact to the flow substances. Due to the advantages of MIT, this suggests that MIT could be an alternative inspection and imaging technique for both fields. MIT has previously been considered as a potential candidate for NDE applications and industrial process tomography, however, the realisation of MIT remains limited. One of the major issues is that MIT is an inherently low resolution technique. This is due to the fact the inverse problem is an underdetermined ill-posed problem. In order to improve the resolution, efforts need to be made both in the forward problem and the image inversion. Furthermore, in order to meet the standard of NDE technique specification, the system should be equipped with the capability of real time data collection. These issues represent the most influential factors that limit MIT's applicability in the commercial arena.

The key questions relating to the use of MIT technique for NDE applications are:

- What is the intended application, and what is the motivation behind it?
- What are the fundamental and practical limitations of MIT for NDE applications?
- What is the design for the MIT coil array in order to facilitate the inspection?
- What type of damage and defect can be inspected?
- Can an image of the damage or defect be reconstructed?
- What is the imaging resolution that can be achieved?

The key questions relating to the use of MIT in industrial process tomography are:

- Where does MIT fit in the field of industrial process tomography?

- What is the advantage of MIT compared to existing techniques?
- How can MIT be used in multiphase flow imaging?
- What is the sensitivity level and capability of MIT in this field of study?
- What is the future direction of MIT?

In this study, the author will investigate how to employ the Bath MK-I and MK-II systems for the aforementioned applications. As such, the system design is not within the scope of this study. Nevertheless, there are improvements that can be made to accommodate the intended objective of the study. In general, the methodologies used in this research can be categorised in four aspects:

- Investigating different geometries of MIT coil arrays for the intended applications.
- Establishing the forward models and calculating the sensitivity maps accordingly to assist the imaging process and improve the imaging accuracy.
- Both adopting existing and developing novel algorithms for the image reconstruction to improve the resolution of MIT.
- Conducting both simulations and experimental work to establish the capability of MIT for the proposed applications.

1.3 Thesis Organisation

This thesis is organised in the following chapters. Chapter 2 introduces the methodologies of MIT, including the fundamental principles, eddy current modelling, image reconstruction algorithms and two types of MIT systems used throughout this research.

In chapter 3, MIT is proposed as a non-destructive evaluation (NDE) technique for pipeline imaging. The existing NDE techniques for pipeline inspection are reviewed and the merits and limitations of each technique are addressed. A Bath MK-I MIT system is proposed for this application. Experimental evaluations are carried out based on laboratory investigations. In addition, a localised algorithm, narrowband pass filtering method (NPFM), is developed specifically for the cylindrical pipe geometry. Comparative results using both traditional algorithms and this novel algorithm show that the NPFM can achieve an unprecedented resolution of 2%. Machined wall losses on metallic pipes are inspected and images are reconstructed based on this method.

In addition to metallic structures, chapter 4 studies the applicability of MIT in the inspection of carbon fibre reinforced polymers (CFRPs). One of the advantages of MIT is that it is flexible with coil geometry. This indicates that the coil array of the system can be designed according to a specific application. In this case, a dual planar array is developed and used for hidden defect inspection in CFRP plates, which commonly occur during the

initial manufacturing stage. Both single and multiple defects in CFRP plates are identified and 3D images reconstructed.

Expanding upon the concept of a dual planar MIT system, chapter 5 presents a single planar array MIT study for 3D near subsurface imaging as a means of limited access tomography. This is more challenging compared to a dual planar MIT study as the access is limited to one surface, resulting in limited measurement data. In this chapter, both simulated and experimental work are carried out. Qualitative evaluations of the 3D image reconstruction results show a penetrative depth of $3-4cm$ beneath the imaging subject. The system development, practical implications, capability and limitations of subsurface imaging are addressed.

Noticing that the coil geometry varies from circular, to dual planar to a single planar from chapters 3 to 5, this results in missing data as a result of limited access to the imaging subject. In chapter 6, the missing data effect is studied systematically in both 2D and 3D cases. The Bath MK-I system with 32 sensors is introduced, which is specifically designed to study the effect of missing data on the quality of reconstructed images in MIT. Missing data is investigated by systematically removing the coil sensors through an undersampling process and limited angle imaging. To examine a range of missing data sets, two experimental scenarios were completed: undersampling measurements and limited angle imaging. The former is carried out by evenly undersampling 4, 8, and 16 sensors from a 32 sensors coil array and the latter is investigated by using limited angles of 45°, 90°, 180° and 270°, compared to 360° full angle imaging. An image quality measure and 1D graph of the conductivity distribution are adopted to quantify the effect of missing data on MIT images through experimental evaluation. This study has also been further extended in 3D. A cube sensor is designed for this purpose. The information loss due to systematic removal of planes of sensors is evaluated using singular value decomposition and resolution matrix analysis. The observation of this 3D case study is consistent with that of a 2D case.

Chapter 7 presents an experimental evaluation of MIT in conductive phase flow imaging. Experiments are conducted covering as broad a range of conductivity contrasts as possible, so as to encompass several scenarios of potential interest in industrial flow environments. Our evaluation of fluid experiments includes (a) the smallest conductivity contrast in which image reconstruction in various non-conductive and conductive backgrounds is possible, (b) distinguishing three strata of non-homogenous conductive fluids in a free space, and (c) imaging a flow of non-homogenous bubbles of gas in various conductive backgrounds. Taken together, various capabilities of an MIT system in conductive phase imaging are demonstrated.

Chapter 8 summarises the research output in this thesis, discusses the direction of the future work and highlights the associated challenges. The future work includes image reconstruction improvement, system hardware enhancement and implementation of a multi-frequency MIT system.

Chapter 2

Methodologies of MIT

2.1 Fundamental Principles

Magnetic induction tomography utilises inductive coils to map the electromagnetic properties of an object. The fundamental principles of MIT can be explained by using basic mutual inductance and eddy current theories. As shown in Figure 2.1, by passing an alternating current into an excitation coil, a primary magnetic field can be generated, which induces an electric field that can be detected by a measuring coil. From this field the induced voltage can be measured. If there is a conductive object placed within this time-varying field, an eddy current arises, which can also generate a magnetic field, called the secondary magnetic field. As such, the electric field on the measuring coil can be induced, in part, by both the primary and secondary fields. The induced voltages on the measuring coil therefore differ depending on whether a conductive object is present within the field; if no such object is present, the induced voltage arises entirely due to the primary field, whereas if an object is present, the induced voltage arises due to both primary and secondary fields. By analysing the difference in the induced voltages, one can obtain the properties of the conductive object. Thus, the MIT problem is essentially an eddy current problem, hence it is also called eddy current tomography. Note that in the context of this research, the electrical conductivity of the object is the focus of the passive electromagnetic properties.

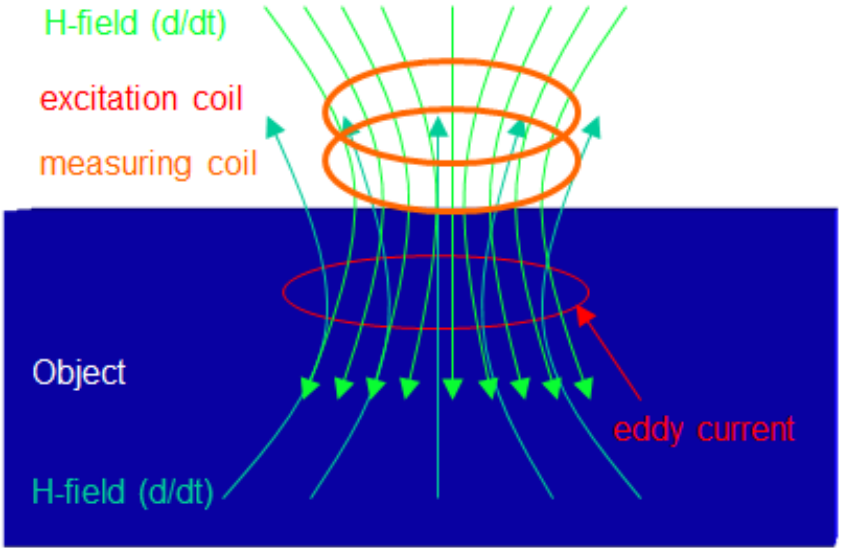

Figure 2.1: Fundamental principles.

The fundamental principles in Figure 2.1 can be interpreted in terms of a simplified electric circuit diagram (Figure 2.2). The excitation coil with a supplied alternating current can be seen as an AC source. Consider the excitation coil as inductor L_1 and the measuring coil as inductor L_2. The measured voltage on L_2 due to induction is $\dot{U}_2$. The properties of the imaging subject can be simplified using a $R-C$ circuit representation. As the eddy current is induced around the object, the imaging subject can be seen as a voltage source $\dot{U}_3$, whereby the inductance of the object is L_3. The mutual inductance among L_1, L_2 and L_3 are M_{12}, M_{13} and M_{23} respectively. The goal is to derive a relationship between the primary voltage and the secondary induced voltage using this circuit diagram.

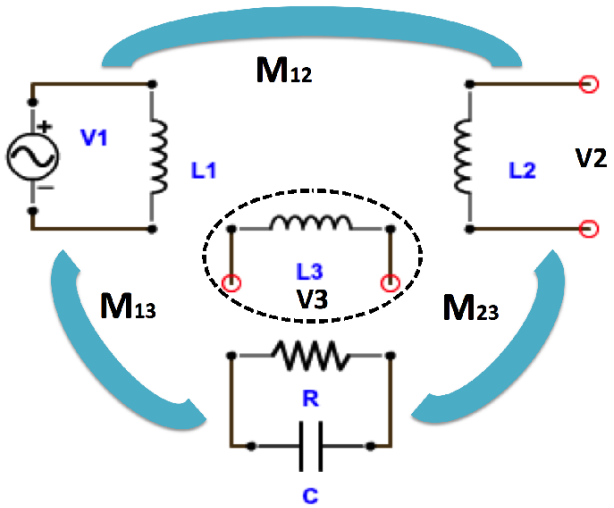

Figure 2.2: Equivalent circuit of mutual inductance theory.
Adapted from [21].

Using the magnetic flux equations, one can obtain

$$\dot{I} = \frac{di}{dt} = j\omega i = j\omega \frac{\dot{U}}{j\omega L} = \frac{\dot{U}}{L} \tag{2.1}$$

The induced voltage $\dot{U}_2$ on inductor L_2 consists of two parts, $\dot{U}_2^{'}$ and $\dot{U}_2^{''}$. $\dot{U}_2^{'}$ is the voltage directly induced by the primary voltage $\dot{U}_1$. This primary voltage also results in $\dot{U}_3$, which in turn induces $\dot{U}_2^{''}$.

$$\dot{U}_2^{'} = -M_{12}\frac{di_1}{dt} = -M_{12}\frac{\dot{U}_1}{L_1} \tag{2.2}$$

$$\dot{U}_2^{''} = -M_{23}\frac{di_3}{dt} = -M_{23}j\omega\dot{I}_3 \tag{2.3}$$

As $\dot{U}_3$ is also induced by the primary field, then:

$$\dot{U}_3 = -M_{13}\frac{di_1}{dt} = -M_{13}\frac{\dot{U}_1}{L_1} \tag{2.4}$$

It is readily seen that:

$$Z_3 = (R//\frac{1}{j\omega C}) = \frac{R}{1+j\omega RC} \tag{2.5}$$

Hence:

$$\dot{I}_3 = \frac{\dot{U}_3}{Z_3} \tag{2.6}$$

As $\dot{U}_2 = \dot{U}_2^{'} + \dot{U}_2^{''}$, then combining the above equations 2.2 to 2.6:

$$\dot{U}_2 = \{-M_{12} + M_{13}M_{23}(j\omega\frac{1}{R} - \omega^2 C)\}\frac{\dot{U}_1}{L_1} \tag{2.7}$$

where $\dot{U}_i$ and $\dot{I}_i$ are the voltages and currents passing through the inductors, and L_i and M_{ij} are the self inductance and mutual inductance coefficients for the inductors respectively. Equation 2.7 suggests that the induced voltage is dependent on the frequency and the properties of the imaging subject.

$$\frac{\dot{U}_2}{\dot{U}_1} \propto \omega(-j\frac{1}{R} + \omega C) \tag{2.8}$$

It is well known that both the resistance and capacitance of a given material (in this case, the imaging subject) can be defined using the electrical conductivity or permittivity of a uniform specimen of the material.

The conductivity of a given specimen can be defined using the resistance of a given section

of that specimen:

$$\sigma = \frac{1}{R}\frac{l}{A} \tag{2.9}$$

where l is the length of the section and A is the cross-sectional area of the section.

Similarly, the permittivity of a given specimen can be defined using the capacitance of a given section of that specimen. The definition for capacitance is

$$C = \varepsilon_0 \varepsilon_r \frac{A}{d} \tag{2.10}$$

where A is the area of overlap of the two plates and d is the separation between the plates for a given cross section of the material.

As both $\frac{l}{A}$ and $\frac{A}{d}$ can be considered constant for a specimen with given dimensions, then equation 2.8 can also be formulated in the following manner:

$$\frac{\dot{U}_2}{\dot{U}_1} \propto \omega(-j\sigma + \omega\varepsilon_0\varepsilon_r) \tag{2.11}$$

This indicates that if the imaging subject is highly conductive, the real part can therefore be neglected. The induced voltage can be considered proportionate to the amplitude of the conductivity $|\sigma|$. For biomedical applications, focusing on living tissue, this conductivity is usually very low. As such, the imaginary part cannot be ignored as the induced voltage depends on both the amplitudes and the phase shift of $-j\sigma + \omega\varepsilon_0\varepsilon_r$.

In [13], the authors considered the MIT problem from the point of view of electromagnetic field interaction, i.e., using a single channel MIT system to derive the relationship between the primary magnetic field generated by an excitation coil and the secondary magnetic field induced by the eddy currents, and also reached the same conclusion as shown in equation 2.11.

2.2 Forward Problem

For an electromagnetic tomography imaging system, two problems need to be solved, namely the forward and inverse problems. Given the distribution of conductivity (or other passive electromagnetic properties) with an excitation current, the forward problem is to solve the estimated measurement signals from the sensors [4, 22, 23]. This can be written in the following form [24]:

$$F = \int_v f(\hat{E}, \hat{H}) dv \tag{2.12}$$

where F is a function of the electric and magnetic fields at a given point. The fields are themselves implicit functions of the system parameters: the conductivity σ, the permeability μ, the permittivity ε, or any combination of the previous. The MIT forward model can be illustrated using Figure 2.3. In general, the fields and the system will take on dif-

ferent values at each point in space, which are determined by the eddy current induced in the system. Therefore, the forward problem is often called the eddy current problem.

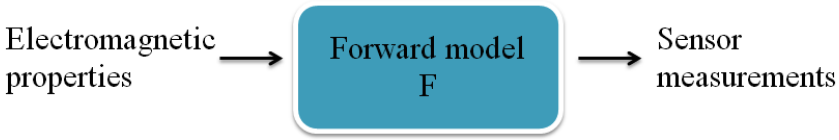

Figure 2.3: Illustration of MIT forward model.

2.2.1 Maxwell's Equations

The forward problem is solved under the condition of a quasi-static electromagnetic field. In this condition, a few assumptions need to be made. First, the displacement current is neglected; second, the material is considered to have an isotropic character; third, the eddy current effect in the current source is also neglected. Note that there are two regions in the quasi-static electromagnetic field, the non-conducting region and the eddy current region (shown in Figure 2.4).

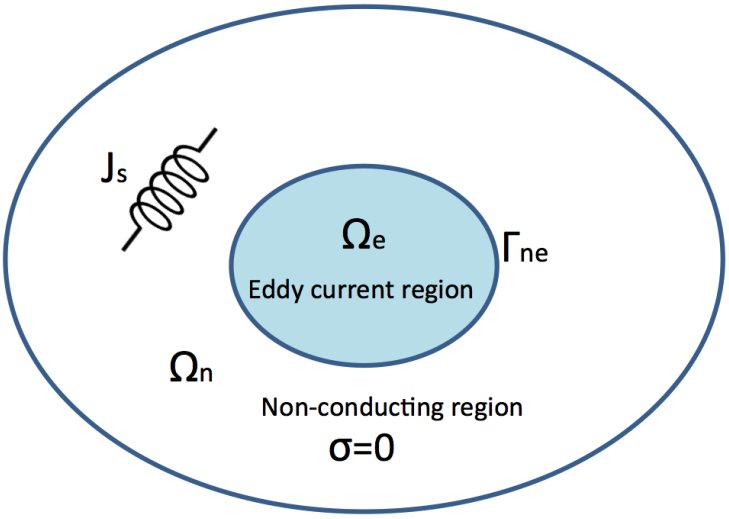

Figure 2.4: Eddy current region.

Using the time-harmonic notation of Maxwell's equations, in the eddy current region Ω_e:

$$\nabla \times H = J_{eddy} \tag{2.13}$$

$$\nabla \times E = -j\omega B \tag{2.14}$$

$$\nabla \cdot B = 0 \tag{2.15}$$

In the non-conducting region Ω_n:

$$\nabla \times H = J_s \tag{2.16}$$

$$\nabla \cdot B = 0 \tag{2.17}$$

In each region, the B and H fields satisfy that the normal component of the B field is zero and the tangential component of the H field is zero. On the boundary between the two regions Γ_{ne}:

$$B_e \cdot n_e + B_n \cdot n_n = 0 \tag{2.18}$$

$$H_e \times n_e + H_n \times n_n = 0 \tag{2.19}$$

where J_{eddy} is the eddy current density in Ω_e, J_s is the current density due to the excitation in the non-conducting region Ω_n, n is the normal vector on the boundary, and B_e, H_e, n_e, B_n, H_n, n_n refer to the the magnetic flux, magnetic field and normal vectors in regions of Ω_e and Ω_n respectively. The uniqueness of B and E are therefore ensured.

2.2.2 Eddy Current Formulation

Various eddy current formulations in three dimensions have been studied, using a combination of the magnetic vector potential, magnetic scalar potential and electric scalar potential [25, 26, 27, 28, 29, 30, 31]. Regardless of the formulation, it has to comply to the uniqueness of the fields and the boundary conditions. The work presented in this thesis is based on reduced magnetic vector potential formulations $(A_r, A_r - \phi)$ to avoid modelling the structure of the coils using edge finite element method (FEM) [32, 33, 34, 35].

$$\nabla \times \frac{1}{\mu} \nabla \times A + j\sigma\omega A = J_s \tag{2.20}$$

where the current density, J_s, can be prescribed by the magnetic vector potential according to the Biot-Savart Law.

The magnetic potential, A, is the sum of two parts: A_s, the impressed magnetic vector potential as result of current source J_s, and A_r the reduced magnetic vector potential in the eddy current region Ω_e.

In the non-conductive region Ω_n:

$$\nabla \times H_s = J_s \tag{2.21}$$

where H_s is the magnetic field generated by an excitation coil, which can be directly computed from in any point P in free space from J_s:

$$H_s = \int_{\Omega_n} \frac{J_s(Q) \times r_{QP}}{4\pi \mid r_{QP} \mid^3} d\Omega_Q \tag{2.22}$$

where r_{QP} is the vector pointing from the source point Q to the field point P.

The impressed magnetic vector potential A_s can be written as:

$$\nabla \times A_s = \mu_0 H_s \tag{2.23}$$

From equations 2.22 and 2.23, A_s is readily shown as:

$$A_s = \int_{\Omega_n} \frac{\mu_0 J_s(Q)}{4\pi \mid r_{QP} \mid^2} d\Omega_Q \tag{2.24}$$

In the entire region $\Omega_n + \Omega_e$, the magnetic flux density can be expressed by:

$$B = \mu_0 H_s + \nabla \times A_r \tag{2.25}$$

According to Faraday's Law of induction, ignoring the displacement current, the induced electric field can be written in the following form:

$$\nabla \times E = -j\omega \nabla \times A \tag{2.26}$$

The induced electric field can also be written using a magnetic vector potential and an electric scalar potential:

$$E = -j\omega(A + \nabla\phi) \tag{2.27}$$

The eddy current arises when a conductor is exposed in a time-varying magnetic field; therefore, in the eddy current region Ω_e:

$$J_{eddy} = \sigma E \tag{2.28}$$

In the region of $\Omega_n + \Omega_e$, the magnetic field can be expressed by:

$$\nabla \times H = J_{eddy} + J_s \tag{2.29}$$

It is known that:

$$B = \mu H \tag{2.30}$$

where μ is the permeability of the medium.

Combining equations 2.21, 2.25, 2.27,2.29 and 2.30:

$$\nabla \times (\frac{1}{\mu} \nabla \times A_r) + j\omega\sigma A_r + j\omega\sigma \nabla \cdot \phi = \nabla \times (\frac{1}{\mu_0} \nabla \times A_s) - j\omega\sigma A_s - \nabla \times (\frac{1}{\mu} \nabla \times A_s) \tag{2.31}$$

In MIT, the inductive coils are considered magneto-static not antennas; as such the wave propagation effect can be ignored. Edge FEM is a useful technique to solve such problems by approximating the system as a combination of linear equations in small elements with appropriate boundary conditions. In edge FEM on a tetrahedral mesh, a vector field is represented using a basis vector function N_{ij} associated with the edge between nodes i and j :

$$N_{ij} = L_i \nabla L_j - L_j \nabla L_i \tag{2.32}$$

where L_i is a nodal shape function. Applying the edge element basis function to Galerkin's approximation [36, 37, 38, 39], one can obtain:

$$\int_{\Omega_e} (\nabla \times N \cdot \frac{1}{\mu} \nabla \times A_r) dv + \int_{\Omega_e} j\omega\sigma N \cdot A_r dv =$$

$$\int_{\Omega_c} (\nabla \times N \cdot \frac{1}{\mu_0} \nabla \times A_s) dv - \int_{\Omega_c} (N \cdot j\omega\sigma A_s) dv - \int_{\Omega_c} \nabla \times (N \cdot \frac{1}{\mu} \mu_0 \nabla \times A_s) dv \quad (2.33)$$

where N is any linear combination of edge basis functions, Ω_e is the eddy current region, and Ω_c is the coil region. The right hand side in equation 2.33 can be solved by equations 2.22 and 2.24. The only unknown variable is the reduced vector potential A_r. By applying edge FEM, the second order partial differential equations can be computed by a combination of system linear equations, which can then be solved. The A_r can be obtained using the BiConjugate Gradients Stabilized Method to solve the system linear equation [40, 41, 42, 43]:

$$SA_r = b \quad (2.34)$$

where S is system matrix and b is the right hand side current density. Assuming the medium has a constant permeability characteristic, equation 2.34 can be written as a linear system matrix form as:

$$\begin{bmatrix} \nabla \times (\frac{1}{\mu} \nabla \times ()) + j\omega\sigma() & j\omega\sigma\nabla \cdot () \\ j\omega\sigma\nabla \cdot () & j\omega\sigma\nabla \cdot () \end{bmatrix} \begin{bmatrix} A_r \\ \phi \end{bmatrix} = \begin{bmatrix} -j\omega\sigma A_s \\ -j\omega\sigma\nabla \cdot A_s \end{bmatrix} \quad (2.35)$$

The boundary equation is satisfied by:

$$n \cdot (j\omega\sigma\nabla \cdot (A + \nabla\phi)) = 0 \quad (2.36)$$

By solving the reduced magnetic vector potential A_r, one is able to evaluate the induced voltages in the measuring coils. The induced voltages can be calculated by using a volume integration form:

$$V_{mn} = -j\omega \int_{\Omega_c} A \cdot J_0 dv \quad (2.37)$$

where $A = A_s + A_r$, and J_0 is a virtual unit current density passing through the coil.

The sensitivity matrix is essential in MIT as it realises the linearisation between the conductivity and the induced voltages. The elements of the Jacobian matrix can be expressed by [40, 42, 44]:

$$\frac{\partial V_{mn}}{\partial \sigma_k} = -\omega^2 \frac{\int_{\Omega_k} A_m \cdot A_n dv}{I_0} \quad (2.38)$$

where V_{mn} is the measured voltage, σ_k is the conductivity of pixel k, Ω_k is the volume of the perturbation (pixel k), A_m and A_n are, respectively, solutions of the forward problem when the excitation coil m is excited by I_0 and when the sensing coil n is excited with unit current.

2.3 Inverse Problem

For a given mapping J: $X \rightarrow B$ equation - for each $b \in B$, $\sqsupseteq x \in X$, such that $Jx = b$ is not always true - the solution is neither unique nor stable. A small arbitrary perturbation of the data can create an arbitrarily large perturbation of the solution. This is often referred to as an ill-posed problem. There are many inverse studies in MIT, where the sensitivity map computations and various image reconstruction algorithms are reported [18, 45, 46, 47, 48, 49, 50, 51, 52, 53, 54, 55, 56]. In this section, several well-known linear algorithms will be used for solving the MIT inverse problem. These algorithms are used for the later chapters based on the specific inverse problem one wishes to solve.

The inverse problem can usually be formulated in terms of optimising an object function. F represents physical measurements and the goal is to solve the distribution of conductivity (or the other passive electromagnetic properties) while the measurement signals are given [57, 58]. Solving the inverse problem includes starting with a trial configuration of the system parameters and subsequently modifying this configuration using iterative or non-iterative optimisation algorithms. The inverse problems can be illustrated in Figure 2.5.

Figure 2.5: Illustration of MIT inverse model.

The MIT inverse problem usually makes use of the forward model as part of the solving process, and it can be defined as:

$$Jx = b \tag{2.39}$$

where b is a column vector consisting of M induced voltages (measurements from sensors), x is a column vector representing K pixels in a 2D case, and J is a $M \times K$ matrix of the sensitivity map, which can be computed from the forward model. In most cases, b is far less than x, (i.e., $M < K$), with the consequence that J is non-reversible and non-unique, and the solution x is neither unique nor a continuous function of the data b. Therefore, the MIT inverse problem is an ill-posed problem. In addition to the ill-posedness of the MIT inverse problem, there are several difficulties associated with the inverse of the sensitivity matrix J such as having no direct inverse for the sensitivity matrix J, and a correlation between measurements and the pixels. Note that the sensitivity matrix is also known as a Jacobian matrix; in this thesis, both terms are used.

2.3.1 Linear Back Projection

Linear back projection (LBP) is a commonly used image reconstruction algorithm [59, 60, 61, 62, 63]. It can be interpreted as projecting the measured mutual inductance back to each pixel using the same weights as it contributed to the mutual inductance [63]. This approach is simple and effective for hard field tomography as the transmitting signal is in a straight line, i.e., if the sensitivity matrix has a rapidly oscillating sign. However the sensitivity map in a MIT problem usually varies slowly across the image region due to the correlation between the measurements and the pixels. As such, the reconstructed image using LBP is generally blurred. As discussed in equation 2.39, the J is non-reversible. The LBP takes the transpose of J as an approximation. As such it is a poor image reconstruction method and is simply written as:

$$x = J^T b \tag{2.40}$$

2.3.2 Newton One Step Error Reconstruction

The non-iterative methods are commonly used for image reconstruction, which are based on the assumption that the conductivity does not differ very much from a constant. They are widely applied due to their simple computation and real time performance [17, 22, 49, 50, 52, 64]. The Newton one step error reconstruction (NOSER) method approximates linearisation. As a consequence, errors will occur. Let the errors be e. The problem is therefore formulated as:

$$b = Jx + e \tag{2.41}$$

The goal is to minimise the sum of the squared errors which arise from the approximate linearisation. According to the least squares solution (LSS) [65], it takes the following manner to solve the ill-posed inverse problem:

$$min\|b - Jx\|^2 = (b - Jx)^T (b - Jx) \tag{2.42}$$

$$\frac{\partial}{\partial x}[(b - Jx)^T (b - Jx)] = -J^T (b - Jx) = 0 \tag{2.43}$$

$$x = (J^T J)^{-1} J^T b \tag{2.44}$$

From equation 2.44, it can be seen that the inverse of the sensitivity map can be approximated as:

$$J^{-1} = (J^T J)^{-1} J^T \tag{2.45}$$

The LSS guarantees the uniqueness and existence, but not the stability, of the solution, therefore a constant needs to be applied to ensure the stability [66]. According to the

regularisation approach, the solution can be formulated as the constrained minimisation:

$$min[\alpha\Omega(x) + \|b - Jx\|^2] \tag{2.46}$$

where $\Omega(x)$ is called a stabilising function and α is a constant known as a regularisation parameter. The NOSER algorithm uses $\Omega(x) = J^T J$ for the constraining matrix, thus the equation 2.44 becomes [67]:

$$x = (J^T J + \alpha J^T J)^{-1} J^T b \tag{2.47}$$

2.3.3 Tikhonov Regularisation

In order to overcome ill-posedness, it is common practice to regularise the problem by imposing additional information about the solution. As a nonlinear ill-posed inverse problem, it is often first simplified via linearisation. A simple choice for the regularisation penalty term is Tikhonov regularisation [45, 46, 53, 68, 69, 70]. The aim of this regularisation is to dampen the contribution of smaller singular values to the solution. The Tikhonov regularisation method uses a universal regularisation technique for solving the ill-posed inverse problem and it has better performance and produced sharper images than LBP [71]. The solving process of Tikhonov regularisation is similar to that of NOSER, apart from using an identity matrix as a constraining matrix.

$$x = (J^T J + \alpha I)^{-1} (J^T b) \tag{2.48}$$

Similarly with NOSER, this is also referred to as a one-step Tikhonov regularisation method, but note that the image quality is expected to be improved when an iterative process is introduced. This often requires *a priori* information for the initial estimate of the distribution of properties for the imaging subject. In this context only the conductivity distribution is considered. Assuming the initial estimate of the conductivity distribution is x_i, then inputting this into the forward model, one can calculate the simulated voltage measurements b_i and the corresponding sensitivity map J. The next step is to use Tikhonov regularisation to calculate the estimated conductivity distribution, i.e., an estimation of the image.

$$\triangle x_i = J^T (\triangle b_i) \tag{2.49}$$

Incorporating equations 2.45 and 2.48 into equation 2.49, then:

$$\triangle x_i = (J^T J + \alpha I)^{-1} J^T (b_{true} - b_i) \tag{2.50}$$

where the b_{true} is the measured voltages. The final step is to correct the image:

$$\triangle x_{i+1} = x_i + \triangle x_i \tag{2.51}$$

The iteration process stops when a predefined condition is met, otherwise it goes to the first step for the next iteration, as shown in Figure 2.6.

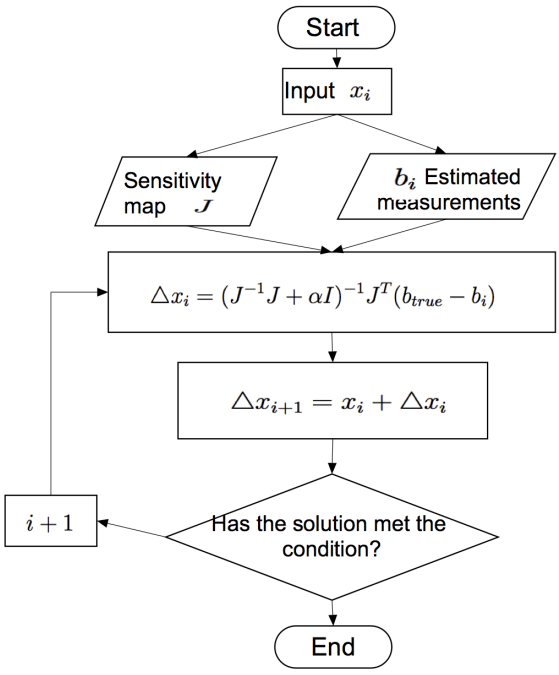

Figure 2.6: Flow chart for the solving process of an iterative Tikhonov method.

2.3.4 Landweber Iteration Method

The Landweber iteration method is widely used in optimisation theory. A good way of understanding it is that it is a method that looks for the steepest gradient descent [72]. Recall the problem in equation 2.42, the Landweber iteration method searches the direction in which $f(x)$ decreases most quickly as the new direction for the next iteration. As such instead of calculating the gradient of the whole equation, as, for instance, in equation 2.43, this method takes the gradient at the steepest point:

$$x_{i+1} = x_i + \alpha \frac{\partial}{\partial x_i}[(b - Jx_i)^T(b - Jx_i)] \tag{2.52}$$

$$x_{i+1} = x_i + \alpha J^T(b - Jx_i) \tag{2.53}$$

where the constant α is known as the gain factor and is used to control the convergence rate. When initialized with zero, i.e., $x_i = 0$, the iteration process converges to the minimum-norm least-squares solution. A suitable convergence criterion is provided by $\| \alpha J^T J \|_2 < 2$, from which a suitable size of the gain factor can be estimated as $\alpha = 2/\lambda_{max}$, where λ_{max} is the maximum eigenvalue of $J^T J$ [73]. The initial estimate can also be made by using a LBP algorithm.

2.3.5 Laplacian Regularisation Method

The Laplacian regularisation matrix adds smoothness to the solution of equation 2.46. Consider that the image region is formed by pixels at each point. The Laplacian regularisation matrix L smoothes the region as described by [74]:

$$L(i,i) = \frac{1}{N}\sum_{j=1}^{N} L(i,j) \tag{2.54}$$

where $L(i,j) = -1$ when j is a neighbouring pixel to pixel i, and zero otherwise. Note that $i \neq j$. Incorporating equation 2.54 into equation 2.46:

$$x = (J^T J + \alpha L)^{-1}(J^T b) \tag{2.55}$$

An additional regularisation matrix can also be added alongside with Laplacian matrix according to the target solution, i.e.,

$$x = (J^T J + \alpha L + \beta R)^{-1}(J^T b) \tag{2.56}$$

where α and β are the parameters of the regularisation matrix L and R respectively. This is sometimes also called the hybrid image reconstruction method [75, 76]. This algorithm offers a certain degree of flexibility. The algorithm equation 2.56 can be formulated into either equation 2.47 or equation 2.48 based on the selection of the regularisation parameters and matrices.

2.3.6 Selection of Regularisation Parameters

There are many methods can be used to select the regularisation parameters for a given inverse problem, such as generalised cross-validation method [77, 78, 79], discrepancy principles method [80], and L-curve method [81]. Among which, the L-curve method is the most recent and commonly used technique in electrical tomography research.

The underlying concept of L-curve accomplishes a trade-off between the two quantities of the objective function (2.41): the solution norm value versus the corresponding residual error norm for each of the regularisation parameter values. Figure 2.7 shows such a plot for a general inverse problem, where for larger values of regularisation parameter (i.e., more filtering), the residual increases without a significant reduction in the norm of the solution, and for smaller values of regularisation parameter (i.e., less filtering), the norm of the solution increases rapidly without prominent decrease in the residual. The best fit regularisation parameter lies in the corner of the curve [82]. However, one should note that not all curves have a pronounced corner to determine the best fit parameter, in which case the selection process is usually done empirically with the guidance from a L-curve plot.

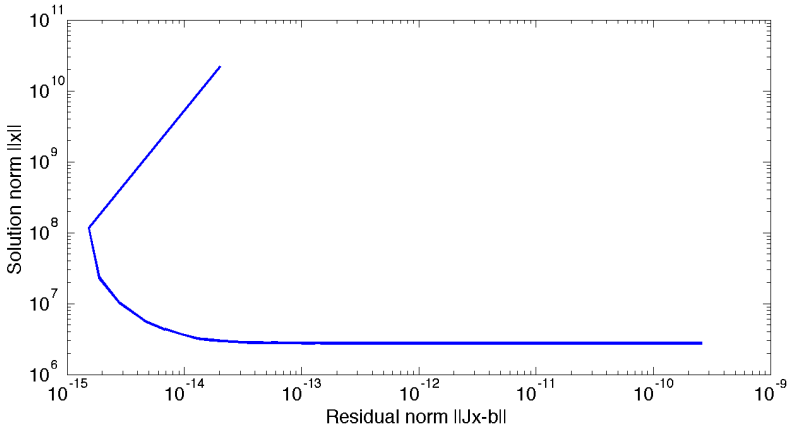

Figure 2.7: L-curve for selecting the regularisation parameter.

2.4 MIT Systems

Regardless of its intended application, a generic MIT system consists of (i) an array of inductive coils, (ii) a data acquisition component to obtain measurements from these coils, and (iii) a host PC for reconstructing images based on these measurements (Figure 2.8). Throughout this thesis, two in-house MIT systems, Bath MK-I and MK-II, are used for experimental work. The design of both systems have been reported in [83, 84]. One of the key differences between the two systems is that the MK-I system uses amplitudes of the induced voltages for image reconstruction, and as such is designed to image materials with high conductivity ($\sigma > 10^5 S/m$), whereas the MK-II system uses phase perturbations for image reconstruction, and as such is designed to image materials with low conductivity ($\sigma < 10 S/m$). This distinction is made because for $\sigma >> \omega\varepsilon$, the phase change caused by eddy currents can be ignored for highly conductive imaging subjects. It can also be seen from the literature review that for applications relating to metallic structures, the operational frequencies were chosen in the range of $5 - 500 kHz$, whereas for biomedical imaging applications, the operational frequencies are usually much higher, varying from $1 - 30 MHz$ [85]. As shown in equation 2.11, the conductivity of biological tissue is usually many orders of magnitude lower than that of metals. In these cases, the field perturbation caused by eddy currents has a phase lag of 90 degrees; as such, amplitude detection (i.e., use of the MK-I system) would lack sensitivity. Therefore it is common practice to supply higher frequencies for a MIT system for biomedical applications in an attempt to increase the signals [3]. Here we briefly introduce the architectures of both systems.

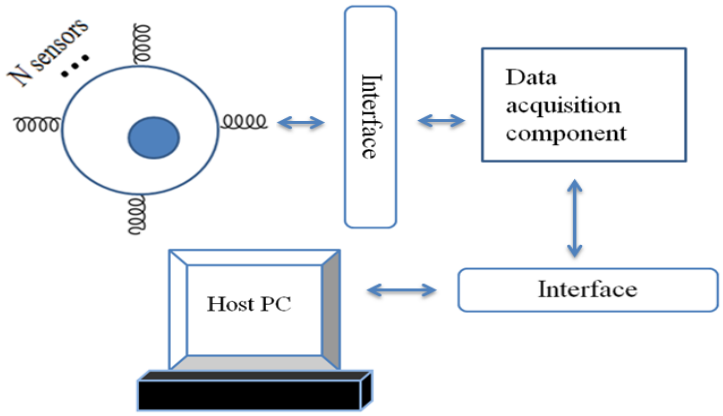

Figure 2.8: Generic MIT system architecture.

2.4.1 MK-I System

The MK-I system system consists of (i) a topward 8112 digital function generator, (ii) an array of inductive coils arranged around the object periphery, (iii) a National Instrument (NI) based data acquisition system and (iv) a host computer.

The data acquisition component consist of two parts, a multiplexer circuit for channel switching and a data acquisition card. An *ADG*406 multiplexer is used in this system to accomplish the channel switching process. The *ADG*406 is a monolithic *CMOS* analog multiplexer which switches one of the sixteen inputs to a common output that is controlled by a 4-bit binary address and control latches. An *EN* input on the device is used to enable the device. When disabled, all the channels are switched off. The *ADG*406 is designed on an enhanced LC^2MOS process that provides low power dissipation yet gives reasonable switching speed. Each channel conducts equally well in both directions when in the *ON* condition and has an input signal range which extends to the supplies. In the OFF condition, the signal to the supplies are blocked. All channels exhibit break-before-make switching action, preventing momentary shorting when switching channels.

An *NI*6295 data acquisition device is connected through USB ports to interface between the *ADG*406 multiplexer and a host PC. This device aims to collect individual data efficiently, combine data effectively and display data in images to suit the needs of the imaging process. The *NI*6295 contains 32 analog input channels and 4 analog output channels. The data acquisition card has 48 bi-directional digital I/O which can be used to control the *ADG*406 multiplexers. The built-in LabVIEW program is used to control the multiplexer and to acquire the signal outputs from *NI*6295. It measures the amplitudes of the induced voltages from the coils. The channel switching process is controlled by a table of binary codes written within the LabVIEW program.

Figure 2.9 shows the MK-I MIT system with an eight channel coil array. The coil array can be designed according to the intended application. Once designed, each of the inductive coils is in turn supplied with a $15V$ peak at a selected frequency from the signal

generator, while the remaining coils are floated as receivers. For a system with N coils, the unique coil pairs are: $1-2, 1-3, ..., 1-N, 2-3, 2-4, ..., (N-1)-N$, giving a full data set consisting of $M = N(N-1)/2$ independent measurements. The image reconstruction module extracts M independent measurements, performs the reconstruction algorithms, then displays and updates the images.

As this system is designed to image materials with high conductivity ($\sigma > 10^5 S/m$), under the condition of $\sigma >> \omega\varepsilon$, the phase change caused by eddy currents can be ignored (equation 2.11). Therefore MK-I MIT system uses the amplitudes of $\mid j\sigma \mid$ (i.e., induced voltages) for image reconstruction. Figure 2.10 shows the induced voltages measured from an eight channel coil array.

This system is employed in the applications presented in chapters 3 to 5. A missing data effect study is also conducted based on this system (chapter 6). Although the same system architecture is used in these chapters, their difference lies in the geometry of the coil array, which will be studied in more details in later chapters.

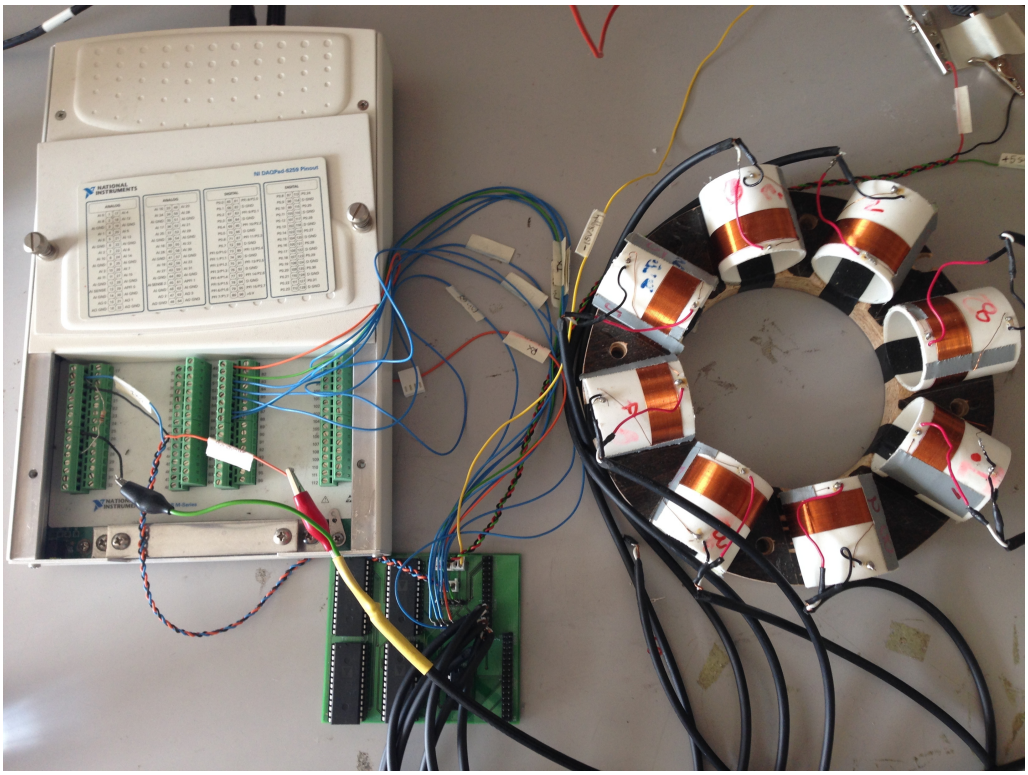

Figure 2.9: MK-I MIT system with 8 channel coil array.

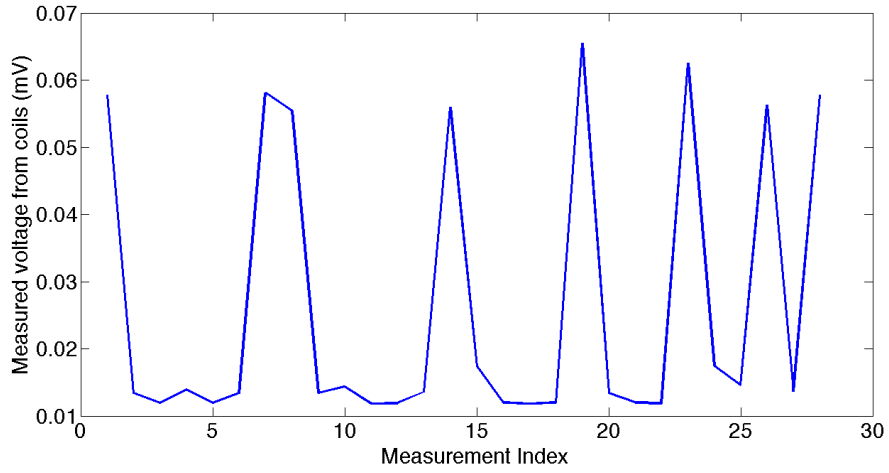

Figure 2.10: MK-I MIT system signals, measured from a 8-channel coil array.

2.4.2 MK-II System

The MK-II system consists of (i) a coil array of equally spaced 16 air-core sensors, (ii) a National Instrument (NI) based data acquisition system and (iii) a host computer (Figure 2.11). The sensing zone has a diameter of $25cm$. Each coil has 6 turns, a side length of $1cm$, and a radius of $2cm$. The coil resonance frequency is $45MHz$. Among 16 coils, 8 coils are dedicated for transmitting signals, and the remaining 8 coils are used for receiving signals. The total number of independent measurements is therefore 64. Noting that the neighbouring measurements are eliminated to reduce the capacitive coupling effect between the excitation and receiving coils,therefore 48 measurements are used in the inverse model to passively map the distributions of the imaging subject.

Unlike the MK-I MIT system, this system measures the phase change caused by imaging substances and uses that change for image reconstruction. Figure 2.12 shows the phase measurements collected from a free space background using this system. As the phase perturbation resulting from a conductive imaging subject is usually very low, it is essential to ensure low noise performance. A grounded aluminium shield is designed to ensure low noise perturbation by reducing the susceptibility to external magnetic field interference, undesired electric fields and the coupling between the coils.

Buffering electronics are also required between the sensors and the NI instrumentation devices for amplifying the signals. A fully differential amplifier $THS4500$ is selected to amplify the transmitting output amplitude from $0.5V$p–p single-ended to $8V$p–p differential signal in order to improve the field strength and phase stability. For the receivers, a low-noise, high-speed amplifier $THS4275$ is chosen to buffer the receiving signals due to its wide bandwidth, low voltage noise and high slew rate. It is worth noting that this buffer has a weak temperature coefficient, although this can be addressed for further system improvement.

As the signal perturbation caused by the secondary magnetic field is usually low, the mea-

surement system requires accurate measurement devices to improve the sensitivity. In addition to this, three additional criteria are considered to choose the appropriate devices. Firstly, the device is required to have the capability to generate a range of frequencies for operational purposes. Secondly, a high-speed direct digitization device is desirable for taking measurements from receiving coils without the need to down-convert the signal into a lower frequency range in order to reduce the system complexity. Thirdly, the devices need to be capable of expanding the system beyond 16 channels. Based on these, a $NI5781$ is chosen for signal generation. It has the ability to generate frequencies ranging from a few kHz to up to $20MHz$. The sampling rate is $100MS/s$. A $NI2953$ is employed to realise the multi-channel switching process. The $NI2953$ is a $500MHz$ $16:1$ multiplexer that controls all the channel switching tasks for the system. In order to improve the system efficiency, a $NI7951$ FlexRIO board is utilised to accelerate the data acquisition process. The driving frequency is 13MHz, with a 15V peak driving voltage and a driving current of 0.39A, the coil resonance frequency is 45MHz. The maximum thermal drift observed is 85 millidegrees over a period of 5 hours. The application proposed in chapter 7 is based on this system.

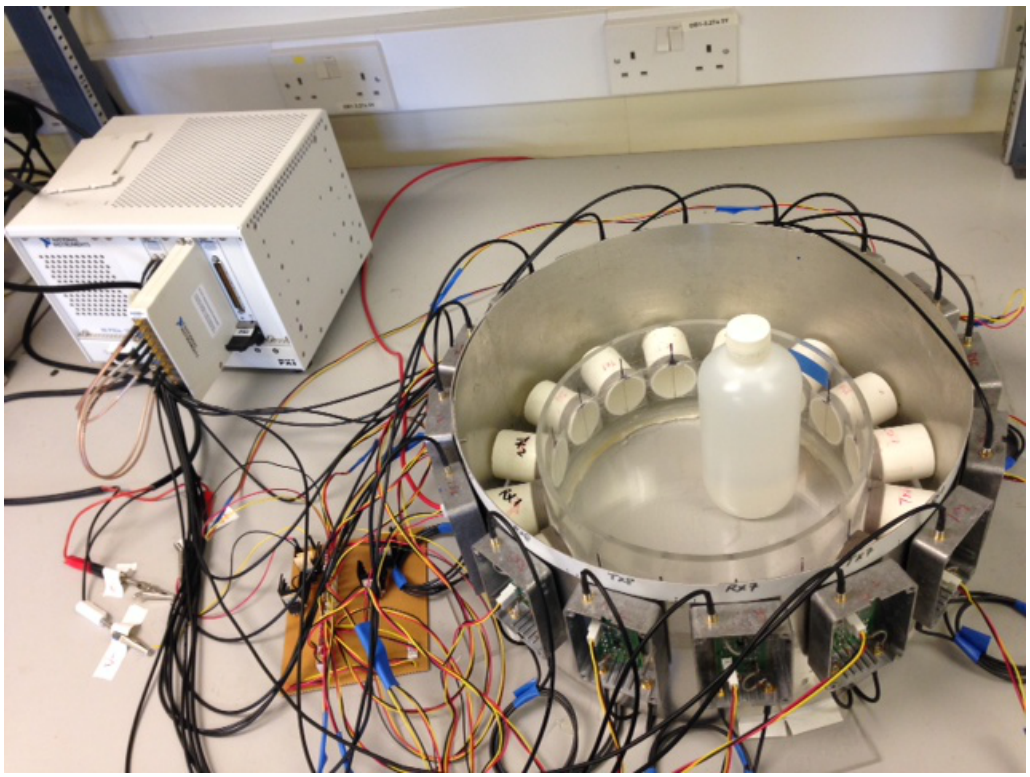

Figure 2.11: MK-II MIT system with 16 channel coil array.

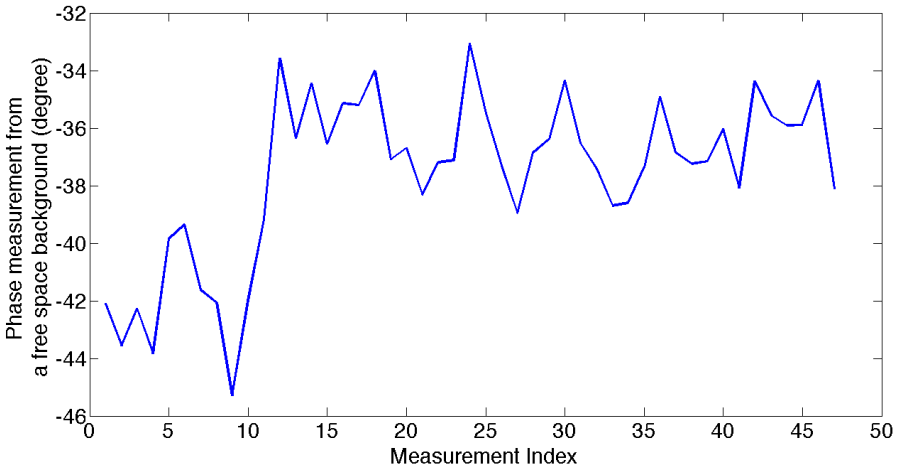

Figure 2.12: MK-II MIT system signal levels.

2.5 Literature Review

The historical development of MIT demonstrates its increasing versatility in terms of potential applications, illustrated by this overview of key studies in the field.

The first MIT imaging system was reported in [59]. The system consist of an 203mm diameter imaging space with 21 coils. An inner ferrite magnetic-confinement screen and an outer conducting electromagnetic screen were designed to prevent noise perturbation. The system operated at a frequency of 500kHz. The cross-sectional images of a copper bar and aluminium foil were obtained using a back projection algorithm.

A feasibility study of electromagnetic imaging for biological tissues was reported in [60]. An operational frequency of 2MHz was chosen to drive the excitation coil. Preliminary results presented in this study showed that objects with electrical conductivities corresponding to fat and fat-free tissues can be differentiated and that the internal and external geometry of simple objects can be sensed. The reconstructed images were obtained from the two coil system using a simple back projection algorithm.

A multiple pole MIT system with 16 coils arranged around an imaging space of 150mm diameter was studied in [86]. This system employed a frequency of 100kHz and a total of 480 measurements were achieved. It was shown to distinguish metallic objects (high conductivity, low permeability) from ferrite (low conductivity, high permeability) using the sign of the signal. The images were reconstructed using linear algorithms.

In [21], the authors presented a MIT measuring system mainly designed for biomedical applications. This system contained 16 inductor and detector coils, and was operated at a frequency of 20MHz. The image of a saline bottle in the measuring region was reconstructed.

An overview study of electromagnetic imaging was discussed in [61]. The authors presented a theoretical background to MIT and a general overview of MIT systems. The study reports that system developments were the focus of earlier MIT studies [59, 45].

Back projection algorithms were used for image reconstructions as they can be run almost in real time, although the quality of reconstructed images was modest. Later MIT studies started to address more specific issues, including sensor design [46, 47, 87], development of conditioning electronics [18], methods [88, 89], algorithms [57] and applications [90].

A number of coil designs were investigated in [46], including parallel, planar and ferrite core coils. The design of each type, and its advantages and limitations, were discussed. In the parallel coil design, the excitation coils surround the object space, which provides equally distributed excitation density. However, the independent measurements are limited. A planar coil design can avoid the background coupling between adjacent coils by overlapping the excitation and detection coils. Ferrite core coils have relatively high sensitivity compared to air core coils, but they experience flux loss due to ferromagnetic materials and eddy currents induced in conductive materials.

In [18], a MIT system with 8 coils for a high contrast metal process application was introduced. Eight coils were evenly spaced along the circumference of a 160mm diameter imaging space. This system operated at a frequency of 5kHz. Images of copper and aluminium rods located in various places of the imaging space were reconstructed using the Tikhonov regularisation method.

A 16 channel MIT system was presented in [91], where a low conductive object was imaged under an excitation frequency of 1MHz. This system researched the sensitivity and stability of a single sensor unit and the phase sensitivity of the system by simulating a human brain with oedema and haematoma.

A National Instrument-based MIT system with an excitation frequency of 13MHz was developed and proposed for biomedical applications [83], where 8 coils were used as transmitters and the remaining 8 coils were used as receivers. This system was later adapted for a feasibility study of cryosurgical monitoring using electromagnetic measurements [92].

A study of a digital MIT system based on half cycle demodulation was examined in [93]. This system employed 8 sensors to form an imaging region of 150mm diameter. The system performance was verified through experimental results. Images of various shaped metal objects were reconstructed.

A fast deterministic algorithm was applied to obtain optimum receiver array designs for a given specific excitation [94]. This design strategy was based on the iterative exclusion of receiver locations, which realises a regionally focused MIT to increase the image resolution in a particular region.

A rotational scheme based MIT (RMIT), where a 8 sensor coil array can be rotated with respect to a central axis perpendicular to the plane of the coil array was implemented in [95]. It was shown that the rotational scheme can increase the image quality through both simulation and experimental data. This paper presented a comparison of reconstructed images for two closely located screws under different rotation schemes. The images were reconstructed using Tikhonov regularisation through experimental data. The main contri-

bution of this paper is the adaptation of several image quality measures for MIT image quality evaluation.

A volumetric MIT (VMIT) system was developed to realise 3D imaging in [96]. In this paper, both the system architecture and the forward 3D sensitivity modeling were presented. Figure 2.13 gives an indication of the 3D visualisation of MIT using experimental data. This VMIT study was the first experimental volumetric study in the field and provided the fundamental background for a four dimensional MIT reconstruction study[97].

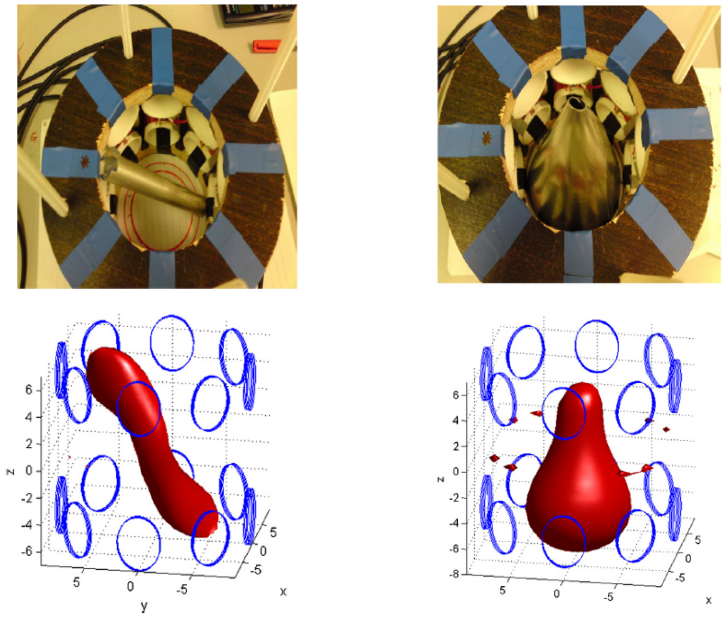

(a) (b)

Figure 2.13: Reconstructed images for (a) an aluminium rod lying diagonally across the measuring space, and (b) an aluminium cone-shaped object in the centre of the measuring space.

Chapter 3

Structural Inspection of Pipelines

3.1 Introduction

Pipelines are one of the most widely used and important apparatus in industry. They can be used to transport water, chemicals, petroleum oil, gas and so on. Pipelines are susceptible to internal and external corrosion, cracking, third party damage and manufacturing flaws. Damaged crude oil or chemical pipelines can have a catastrophic impact upon the environment and on public safety, alongside resulting in financial loss. As such, inspection during both the initial manufacturing stage and in subsequent operation is invaluable.

The structural health monitoring of pipelines has become a great engineering challenge since the 1950s [98]. The majority of pipeline inspection techniques require direct contact or pre-installed devices inside the pipes to carry out the investigation, especially when the pipelines are covered by cladding. Consequently, the inspection can be costly, necessitating highly skilled technicians. Developing a rapid, efficient and low cost technique for this application therefore has significant engineering importance.

In this chapter, MIT is proposed for pipeline inspection as a NDE technique. This chapter also reviews some of the most commonly used NDE techniques, summarising their respective strengths and weaknesses. It is argued that because of the low cost, contactless and non-invasive nature of MIT, MIT could provide a great advantage over existing techniques. The feasibility of MIT in this respect is demonstrated by the Bath MK-I MIT system using metallic pipe samples.

3.2 Overview of Existing NDE Techniques

Traditionally, pipeline inspections were carried out visually, although there has been an increasing reliance upon automated techniques. Visual inspection is the simplest and most cost-effective approach, however it is obvious that it has limited practicality. During the initial pipeline manufacturing stage, many pipelines are covered by layers of coating for protective purposes, along with a final layer of insulation. These usually amount to up to

$10 - 16mm$ of thickness outside the pipes (Figure 3.1). In these cases, inspecting pipes using direct visual inspection becomes impossible. Pipeline inspection engineers later developed a way of dealing with this problem by sending a device inside the pipe to carry out the inspection. This device is called a pipeline inspection gauge, often called pigs or a pigging device in the field. Pigs travel inside the pipe to inspect, maintain and clean the pipeline, and have been widely applied using various NDE techniques including eddy current (EC) testing, magnetic flux leakage (MFL), remote field testing (RFT), ultrasonic inspection (UI), radiograph (X-ray), and electromagnetic acoustic emission transducer (EAMT) techniques.

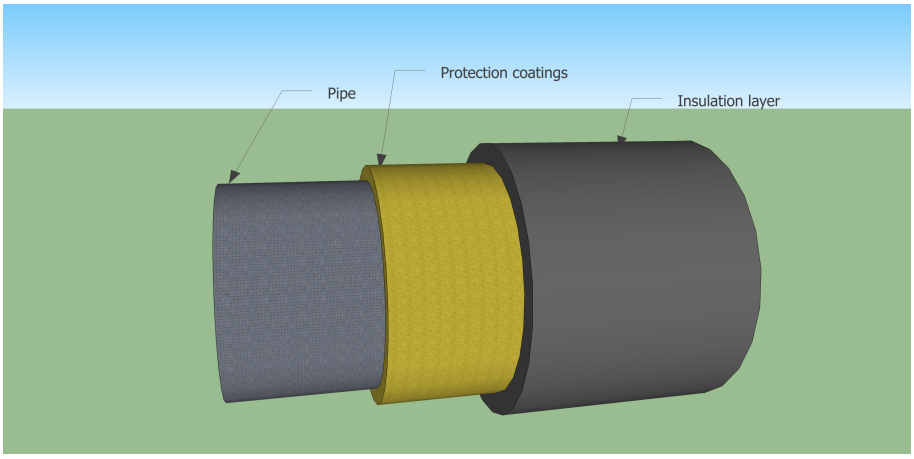

Figure 3.1: Structure of a pipeline.

The eddy current (EC) testing technique uses the interaction between the electromagnetic field and the electrical properties of the testing sample for inspection [99]. Eddy currents arise when applying alternating electromagnetic fields to a conductor through the use of probes or coils. The eddy currents thread around the conductor and in turn produce a secondary electromagnetic field. The conductor can be inspected by analysing the voltage measurements collected from the EC coils. This type of EC testing is also known as the conventional EC testing and is frequently recommended for crack detection on metallic structures [100, 101, 102, 103]. The applicability of this technique has also been further expanded to pipelines [104, 105, 106]. The advantages of this technique are that it is versatile and cost effective; however, it is not commonly used as an in-line inspection (ILI) tool for pipeline inspection due to speed limitations. Pulsed eddy current testing is a specialised eddy current method which overcomes the difficulties associated with the conventional eddy EC testing method, which is that the EC probes require intimate contact with the pipelines [107, 108, 109]. As such, pulsed eddy current testing has become a popular method for detecting corrosion under insulation. However, it has the drawback of not being as reliable for detecting ultra-localised corrosion, such as pitting [110].

Pigging devices based on the magnetic flux leakage (MFL) technique are the most widely used in-line inspection tools and have been used for oil and gas pipes since the 1960s

[111, 112, 113, 114, 115, 116, 117]. The operating principle of MFL is simple and straightforward. A strong magnetic field is established in the pipe wall using either permanent magnets or by supplying an electrical current into the steel. Damaged areas of the pipe cannot support as much magnetic flux as undamaged areas, and as such magnetic flux leaks out of the pipe wall at the damaged sites. This means that the MFL technique also replies upon electromagnetic induction, and as a consequence this technique would not work on non-ferromagnetic materials [118]. A typical MFL pig consists of a magnet, hall sensors and a data acquisition component. There are some external parts that are designed to hold the hall sensors against the inside of the pipe (fingers), which are essential as MFL requires intimate contact between the sensors and the pipe wall in order to achieve adequate sensitivity to defects. Therefore it is understandable that the fingers may get damaged when the pig passes through branches, valves and tees [98].

The technique of remote field testing (RFT) is relatively new, only having been commercialised since the late 1980s [98]. The basic principle of operation of a RFT tool is by energising the pipe with an AC sine wave at frequencies between $1Hz$ and $1kHz$. The electromagnetic wave passes through the pipe wall near an exciter and re-enters the tube at various distances from the exciter. At approximately 3 tube diameters, the field inside the tube is reduced to near zero, while the external field remains fairly strong. In areas of metal loss, the field arrives at the detector with a faster travel time (greater phase) and greater signal strength (amplitude) due to the reduced path through the pipe wall. Hence the dominant mechanism of RFT is through-transmission. It is because of this two-wall transmission path that RFT has gained its reputation of equal sensitivity to outside defect (O.D.) and inside defect (I.D.) wall loss [119, 120, 121]. One distinct disadvantage of RFT is its inability to measure wall thickness through scale, coatings and liners, with approximately equal sensitivity to O.D. and I.D. wall loss. The most common applications include the inspection of heat exchangers and boiler tubes using internal probes connected to an external instrument. In more recent years, larger tools have been developed for applications such as pipelines and water well casting [121].

Ultrasonic inspection (UI) is a useful and versatile NDE technique for pipeline inspection, which also became available in 1980s [122]. Ultrasonic inspection uses an array of transducers that emits a high frequency sound pulse perpendicular to the pipe wall and receives echo signals from the inner surface and the outer surface of the pipe. This technique measures the total time travelled between the arrival of the reflected echoes from the inner and outer surfaces in order to calculate the wall thickness. It can be used for flaw detection, flaw evaluation, dimensional measurements and material characterisation [123, 124, 125, 126].

X-ray inspection uses a source of radiation for material inspection. As the radiation can produce good penetration, it can be used to detect pipeline corrosion without requiring insulation removal; this is arguably the biggest advantage of this technique [127, 128, 129, 130, 131]. One distinct disadvantage is that X-rays, by definition, are radioactive,

and the precautions that need to be implemented during an inspection may be impractical in many environments. In addition, X-ray inspection does not detect cracking and pitting; however, it can be very useful for inspecting other kinds of defects.

Electromagnetic acoustic transducer (EMAT) inspection is a relatively new technique for pipeline inspection. It uses a magnet and an electric coil. The magnet can be a permanent magnet or an electromagnet, which produces a static or a quasi-static magnetic field. The electric coil is driven with an alternating current at ultrasonic frequency, typically in the range of $20kHz$ to $10MHz$. Based on the application requirements, the signal can be a continuous wave, a spike pulse, or a tone-burst signal. The electric coil, if supplied with AC current, also generates an AC magnetic field. Ultrasonic waves are generated close to the test material by the interaction of the two magnetic fields.

Each technique has its advantages and disadvantages, and as such there is no universally agreed approach in the field of pipeline inspection. Many factors need to be taken into consideration when choosing an appropriate technique, such as the material, dimensions and locations of the pipes under inspection, as well as the expected outcomes. Some combined methods have also been proposed in this area in an attempt to mitigate the disadvantages of one individual technique [132, 133]. So far, the techniques of MFL and X-ray have reached commercial standards in terms of their accuracy, resolution and wide applicability. As such, other NDE techniques also used in industrial environments are often evaluated by comparison to MFL or X-ray techniques. Table 3.1 lists the widely used NDE techniques for pipeline inspection.

Technique	EC testing	MFL	RFT
ILI	No	Yes	Yes
Material	Conductive Ferromagnetic Ferritic steel Austenitic steel Admiralty brass	Ferromagnetic Carbon steel	Ferromagnetic Non- ferromagnetic Cast/ductile steel Drill steel Carbon steel
Application	External inspection Near surface Sub-surface crack Flaw detection	Internal scale Corrosion Pits sizing	Heat exchanger Pressure tubes Stress corrosion Casting wells
Strength	Reliable for discontinuous detection Portable	High resolution Varying levels of sensitivity based on testing needs	No need for close contact/coating/ insulation removal Equal sensitivity to internal and external defects
Limitation	Slow response Limited depth Need for insulation/ coating removal	Generating very large data sets Intimate contact Prone to be damaged	Slow speed Unable to distinguish internal and external defects

Technique	UT	X-ray	EMAT
ILI	Yes	Yes	Yes/No
Material	All materials	All materials	Metallic and magnetic
Application	Well detection Crack detection	Corrosion and erosion detection Measure thickness Quality measure	Leak/flaw detection On-shore water/ metallic pipes
Strengths	High sensitivity No pipe wall thickness constrains Defect detection insulation/coating	High resolution Fast speed No requirement for close contact/ coating removal	No requirement for close contact/ insulation removal Measure metal loss Measure wall thickness
Limitations	Hard to pig Produce flow restriction	Radiation High cost Inability to detect cracking/pitting	Need for close contact Restrictions on high frequency

Table 3.1: Comparison of the existing NDE techniques for pipeline inspection.

In this chapter, pipeline inspection using MIT is proposed. From the above, it can be seen that MIT, EC testing, MFL and RFT have the same origins. Their fundamental principles are all based on the Michael Faraday's discovery of electromagnetic induction. All these techniques rely on voltages being generated and measured by sensors. There are several influencing factors on the induced voltages: the change in strength of the magnetic fields, the speed of the coil or device passing through a static magnetic field, the driving frequency, the volume of the metal loss and the proximity of the sensing device

to the source of the change in the magnetic field. These factors manifest in different ways for each technique. In this chapter, the author will investigate the feasibility of MIT for pipeline inspection through these factors and evaluate how MIT can be beneficial in this area.

3.3 Eight-channel Coil Array

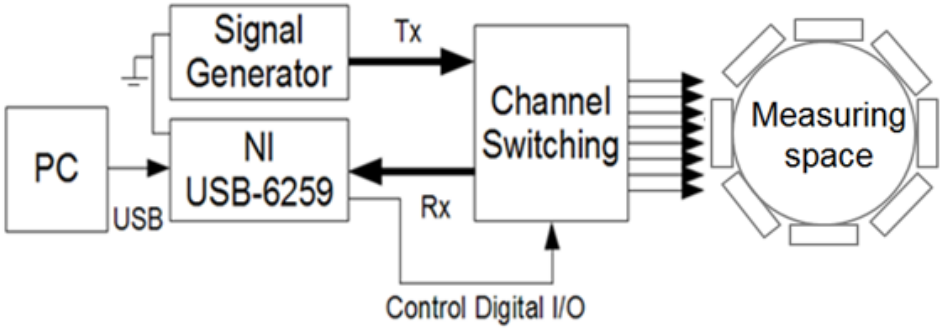

Figure 3.2: MK-I MIT system with an eight-channel coil array.

The MK-I system is used for pipeline inspection. It consists of (i) an array of eight equally spaced inductive coils arranged around the object periphery, (ii) a National Instrument (NI) based data acquisition system and (iii) a host computer, as shown in Figure 3.2. Each coil has a diameter of 42mm, a side length of 14mm and 50 turns. Eight air core coils were constructed manually to form a 100mm diameter imaging region. Figure 3.3 shows a top view of the eight-sensor coil array. Each one of the eight inductive coils in turns is supplied with an excitation signal, while the remaining coils are used as receivers. A list of specifications of this system is shown in Table 3.2. The signal to noise ratio in this MIT system is between 34dB (for measurement between two opposite coils) and 56dB (for measurement between two neighboring coils) at a frequency of 20kHz. Figure 3.4 shows the signal to noise ratio of first cycle measurements when the first coil used as excitation.

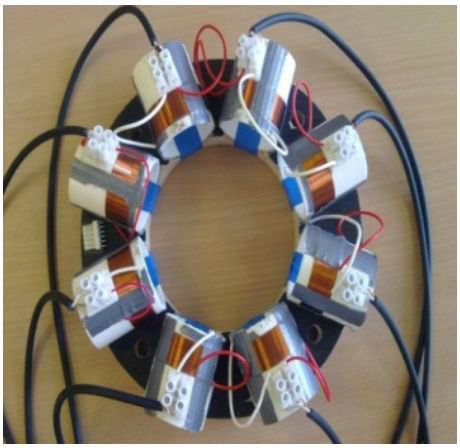

Figure 3.3: Top view of an eight-sensor coil array.

Number of sensors	8
Number of measurements	28
Inner diameter of coil array (*mm*)	100
Coil side length (*mm*)	14
Coil diameter (*mm*)	42
Number of turns for each coil	50
Operational frequency (kHz)	20
Coil type	Air-core coil

Table 3.2: Specifications of eight-channel MIT system.

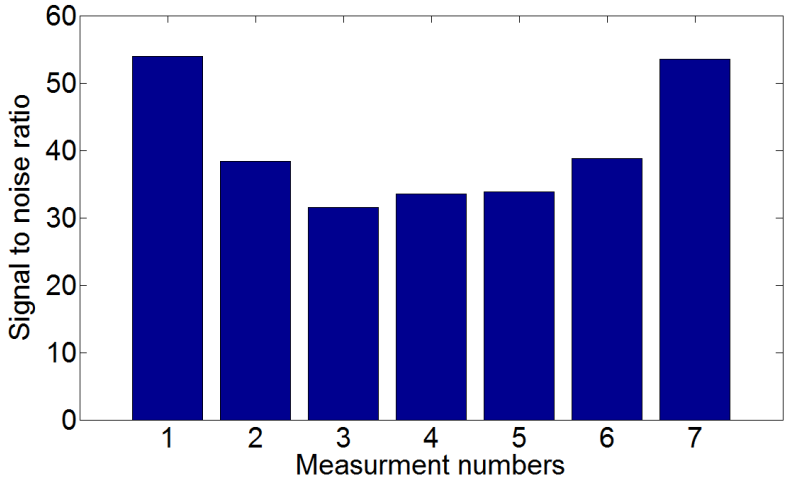

Figure 3.4: Signal to noise ratio of first cycle measurements when first coil used as excitation.

3.4 Forward Model Validation

In the simulated MIT system, eight coils are uniformly distributed around the imaging region. In order to enhance the mesh density, three solid cylinders are simulated inside the imaging region. The radius of the cylinders are 50*mm*, 30*mm*, 10*mm* respectively. The

length of the cylinders are 40mm. The centre of the cylinders locate in $(0,0,0)$ to match the centre of the coil array. The system is simulated in free space, which has 317768 tetrahedral elements. In the actual imaging region, the number of tetrahedral elements is 168072. Each one of the eight coils in turn is supplied with an sinusoidal current under 20kHz, while the induced voltages are measured in the remaining coils. The total number of independent measurements is therefore 28. The mesh model is shown in Figure 3.5.

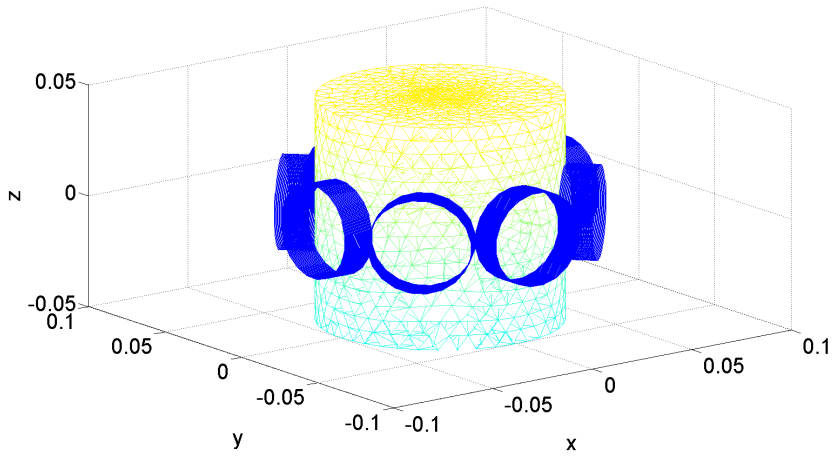

Figure 3.5: Mesh model of an eight-channel MIT system.

In order to validate the forward model, a test scenario is generated by simulating a full pipe in the centre of the region of interest (ROI). The induced voltage is compared with experimental data. In this forward model, the pipe sample with inner radius of 25.40mm and outer radius of 31.60mm is simulated in the mesh geometry, which consists of 3814 tetrahedral elements. The centre of the simulated pipe is located in the centre of the ROI. The induced voltages in the measuring coils due to this full pipe sample can be calculated from equation 2.37. Figure 3.6 shows the comparison of the induced voltage between experimental and simulation data.

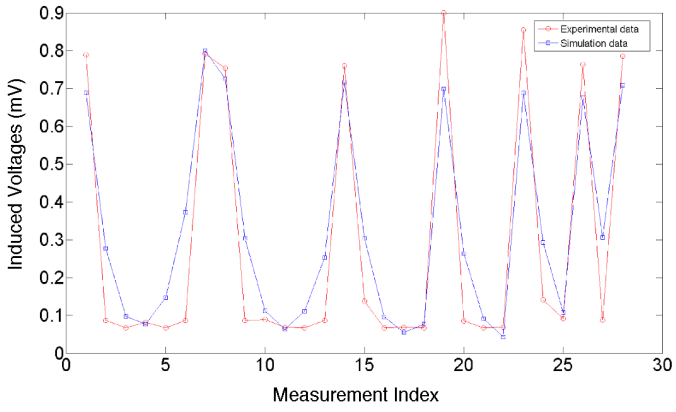

Figure 3.6: Comparison of induced voltages due to full pipe sample using simulation and experimental data.

3.5 Narrowband Pass Filtering Method

Research show that MIT is capable of imaging conductive materials. However, it is challenging to use the traditional MIT pixel based reconstruction method (PBRM) for pipeline inspection because of the limited resolution. In order to improve the MIT resolution, a novel narrowband pass filtering method (NPFM) is developed as a more suitable image reconstruction method. This proposed method can overcome the resolution limitations and produce useful information of the pipe structures. This chapter presents the comparative results of pipeline inspection using both novel NPFM and traditional PBRM. The MIT image reconstruction problem is a challenging ill-posed inverse problem. *A priori* information is key to successful reconstruction process. In pipe imaging, *a priori* knowledge of geometry will be fully explored in our NPFM.

The traditional PBRM is a searching algorithm looking for the best fit of imaging values to create an estimated measured data that matches the real measurements. In PBRM, the imaging domain is divided into small elements by uniform pixels in Cartesian coordinate system. The concept of applying NPFM can be implemented by transferring pixels from the Cartesian coordinate system (x, y) to the polar coordinate system (r, θ). As we are specifically looking at a pipe geometry using NPFM, it is important to notice that only the pixels in the ROI contribute to the final image. In this case, the ROI is limited to a narrow band region only; as shown in Figure 3.7 (a). We then filter the r component pixels that are excluded in the ROI by defining the estimated size of pipe sample in terms of inner radius r_i and outer radius r_o as shown in 3.7 (b). The filtering process takes place before the image reconstruction stage. The filtering process will improve the image quality in the pipe region by allowing the information to be extracted from a limited region.

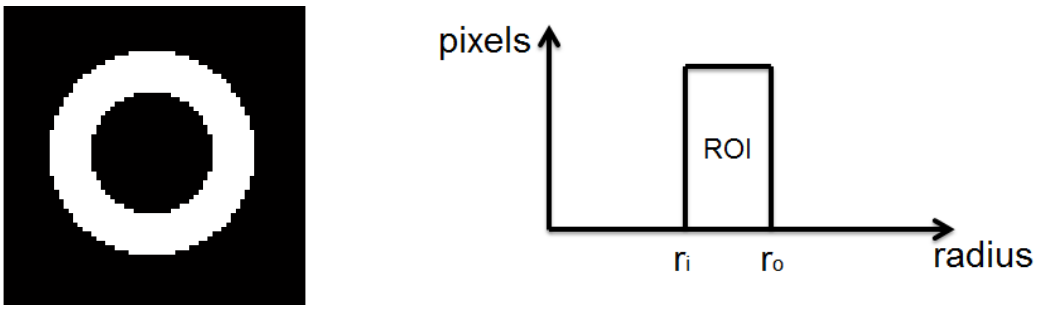

(a) (b)

Figure 3.7: (a) Narrowband region, (b) Narrowband pass filter applied to the radius.

Figure 3.8 shows the comparative results of pipe inspection using both PBRM and NPFM. It can be seen that the NPFM can produce an image reflecting the shape of the pipe taking advantage of targeted ROI for the imaging reconstruction. Note that the location of the pipe sample is crucial to the imaging process, the sample is placed in the centre of the imaging region in order to obtain equal sensitivity from all coils. The narrowband region is selected to be exactly the same size as the pipe. This choice is suitable if we know that the centre of pipe matches that of the exact centre of the coil array. In practical terms,

assuming a larger ROI will compensate any inaccuracy between the actual centre of the pipe and the centre of the coil array.

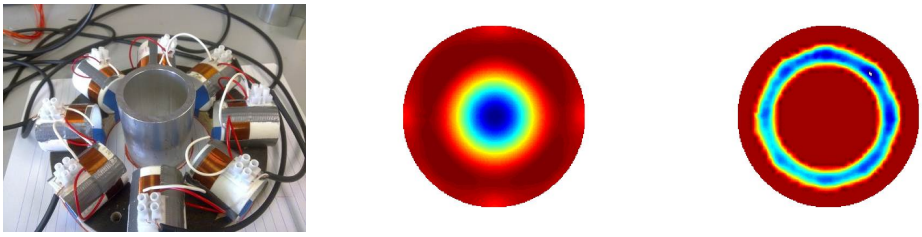

(a) True sample (b) PBRM result (c) NPFM result

Figure 3.8: Comparative results using PBRM and NPFM for a full pipe inspection.

It is also shown in Figure 3.9 that under an operational frequency of $20kHz$, a small piece of metal is placed inside the pipe sample does not affect the recorded signal as under this selected frequency the skin depth is very limited. This indicates that oil/gas (very low conductivity) would not affect the imaging process under the same experimental setup, the pipe inspection could be therefore carried out without causing disruption of the fluids flowing inside.

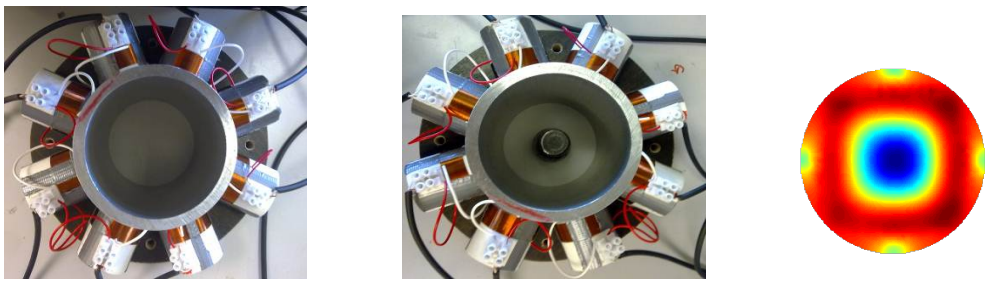

(a) (b) (c)

Figure 3.9: (a) Hollow pipe inspection, (b) Inspection of pipe with a metal inside, (c) Reconstructed images for (a) and (b).

3.6 Experimental Results

3.6.1 Inspection of External Structural Damage

Three aluminium pipe samples with the same inner radius of $25.40mm$ are used in the following experiments. The thickness of the pipe sample is $6.20mm$. A full pipe sample is shown in Figure 3.10 (a). A pipe sample with a large region with external damage is shown in Figure 3.10 (b), where the thicknesses of the removed metal is $4.34mm$. A pipe with a large region of damage and one small region of damage on the external surface of the pipe wall is shown in Figure 3.10 (c), the thicknesses of the removed metal are $4.34mm$ and $1.10mm$. respectively.

As the measured voltages remains the same for PBRM and NPFM, any resolution improvement achieved is due to the filtering process. It is known that only singular values

that are above the noise level contribute to the final images [81]. Figure 3.11 shows the singular value decomposition for both NPFM and PBRM. This provides an useful tool in terms of information content. In the 100*mm* imaging region, PBRM employs 41 by 41 uniform pixels located in the Cartesian coordinate system, each pixel represents a conductivity value. It is demonstrated in Figure 3.11 that there are 26 singular values above an assumed 1% noise level using PBRM, where the number of singular values above an assumed 1% noise level is 25 using NPFM. However, as the pipe sample does not occupy the entire imaging region, which means the number of singular values that contributes to the pipe region is less than 26. The NPFM accomplished a tradeoff between singular values and pixels. The pixels that are not in the ROI are excluded by the filtering process. The result of implementing the NPFM is that 1125 pixels are excluded from the imaging domain, leaving 556 useful pixels to reconstruct the final image, which indicates that a total of 25 singular values above the noise level are fully employed in the image reconstruction.

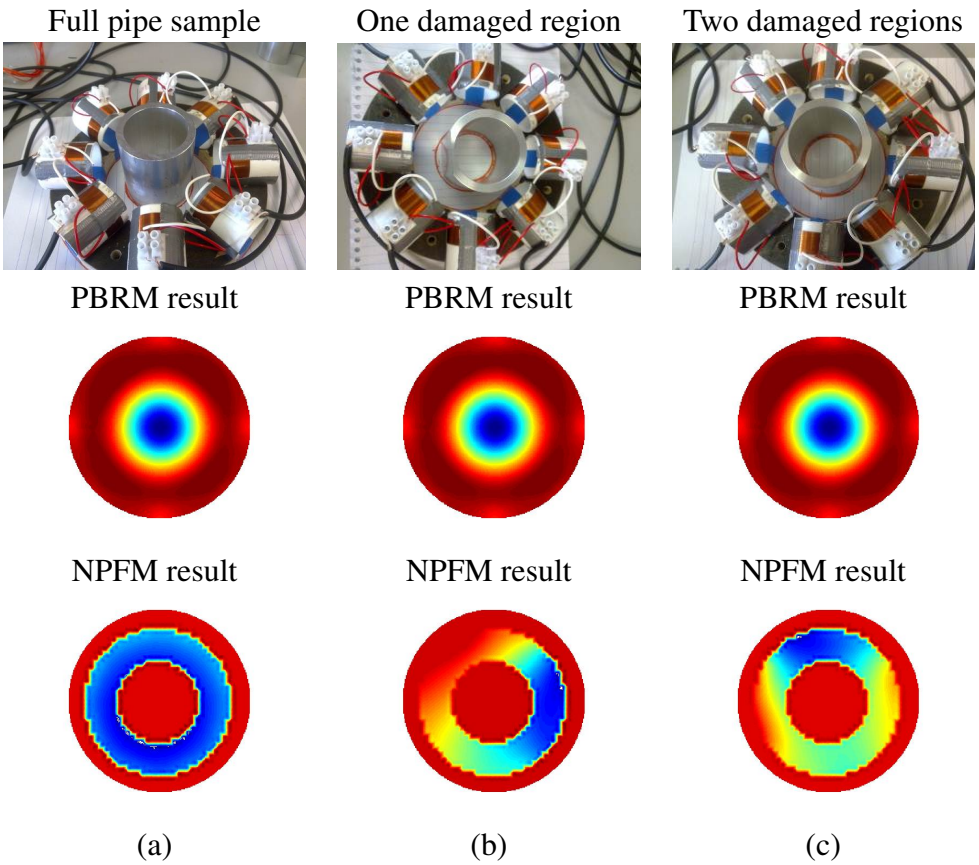

Figure 3.10: Aluminium pipe inspection results showing true samples and reconstruction of external metal losses: (a) a full pipe sample, (b) 4.34*mm* thickness of wall loss, (c) a 4.34*mm* thickness of wall loss on one side and a 1.10*mm* thickness of wall loss on the other side.

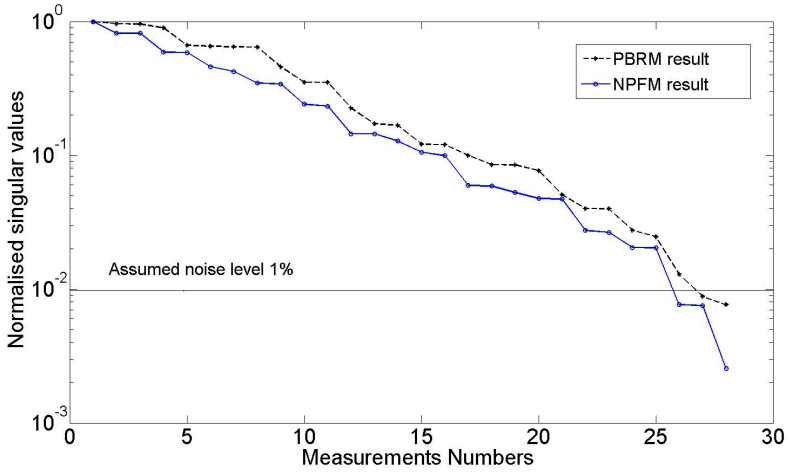

Figure 3.11: Singular value decompositions for PBRM and NPFM.

Figure 3.10 presents comparative results of pipe inspection using both PBRM and NPFM. While the PBRM fails to detect damages in outer structure of the pipe, the NPFM can successfully identify these damages. The advantage of this novel method is verified using experimental data from challenging test samples. It is well known that using a coil array with an imaging region of 100*mm*, the PBRM based MIT can retrieve information with accuracy of 10*mm* (about 10%). With the proposed NPFM, a resolution of 2*mm* (which is about 2%) is achieved using the same measured data.

3.6.2 Further Enhancement of Structural Inspection

In this section, more challenging pipe inspection results will be presented, including inspection of both pipe external and internal wall losses. The NPFM takes advantage of *a priori* knowledge of the original pipe dimensions as reference information for one step calibration. The pipe must be central to the sensors in order to acquire equal sensitivity from the coils; the position of the pipe sample is crucial to the inspection. We suggest that this inflexibility caused by the location of the pipe samples can be partly avoided by choosing a slightly larger narrowband, which can tolerant the inaccuracy of the central position of the pipe sample.

Experimental results based on internal and external structure of aluminium pipes are presented in Figure 3.12. The inner radius of the aluminium pipe is 25.40*mm*; the wall thickness is 6.20*mm*. The thicknesses of the removed metal are 4.34*mm*, 1.10*mm*, 4.30*mm* and 1.90*mm* for pipes in Figure 3.12 (a), (b), (c), and (d) respectively. The imaging results are post-processed within a confident threshold range. Of particular interest is the reconstruction of the internal losses, which are successfully detected using the proposed NPFM based MIT system.

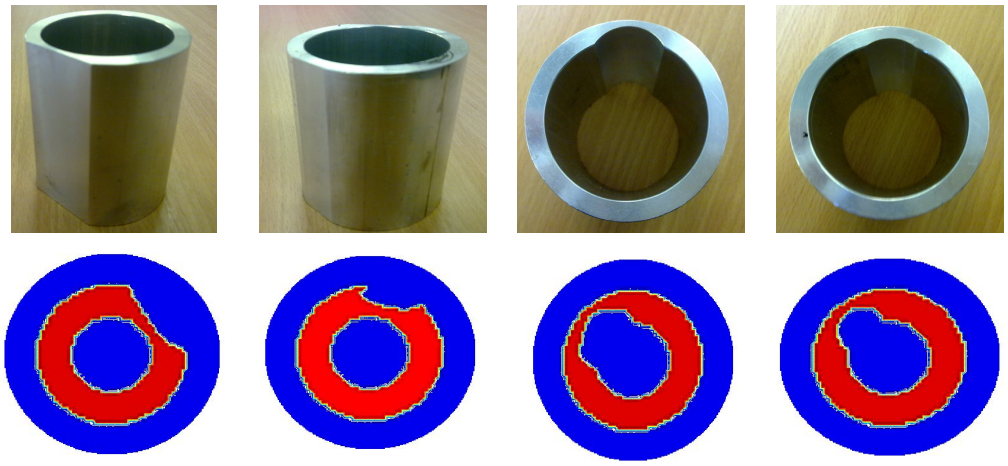

(a) (b) (c) (d)

Figure 3.12: Aluminium pipe inspection results showing true samples and reconstruction of metal losses for internal and external parts: (a) 4.34*mm* thickness of external wall loss, (b) 1.10*mm* thickness of external wall loss, (c) 4.30*mm* thickness of internal wall loss, and (d) 1.90*mm* thickness of internal wall loss.

There is strong industrial interest in steel pipe inspection. It is considered that inspection of steel pipes would be more difficult than aluminium or stainless steel pipes, but theoretically possible. In this section, a steel pipe inspection is carried out. The steel pipes are smaller and thinner compared to the aluminium pipes presented in Figure 3.12, each with an inner radius of 20.38*mm* and a thickness of 5*mm*.

Figure 3.13 shows the reconstruction of external damages from a cold steel pipe using the NPFM. As the permeability affects the skin depth, and the skin depth affects the penetration, the internal structure of the same steel pipe can not be detected reliably under the same operational frequency of 20kHz. The thickness of the external wall losses are 3.44*mm* shown in Figure 3.13 (a) and 2.13*mm* shown in Figure 3.13 (b).

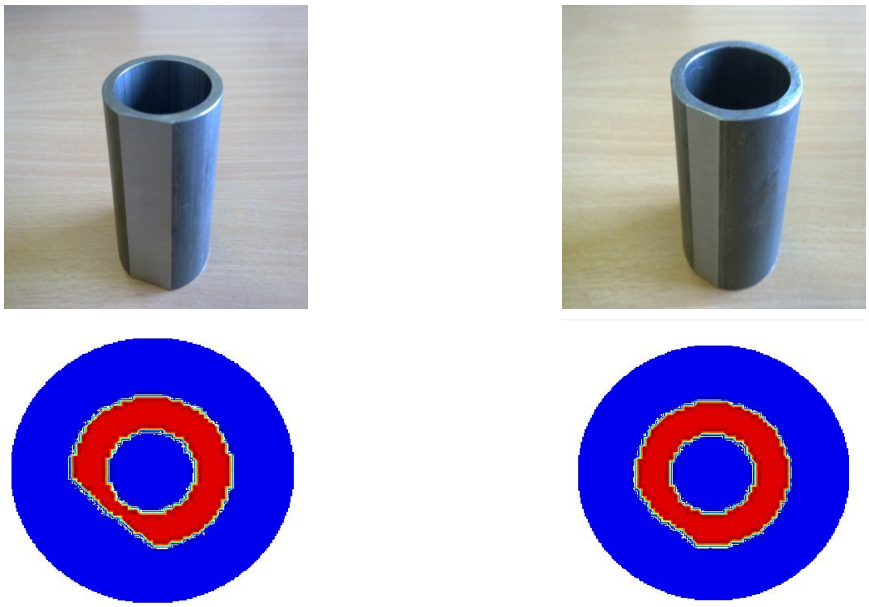

(e) (f)

Figure 3.13: Steel pipe inspection results showing true samples and reconstruction of metal losses for external parts: (e) 3.44*mm* thickness of external wall loss, and (f) 2.13*mm* thickness of external wall loss.

The induced voltages can provide indication in terms of information content. Figure 3.14 demonstrates the induced voltage for cases a to f (listed in Figure 3.12 and 3.13). It is shown that the amplitude of the induced voltage decreases as the dimension of the defect becomes smaller. It is also clear that the induced voltages from internal defects are generally lower compared to the induced voltages from external defects. This is broadly due to the skin depth effect. This issue could be addressed by implementing a multi-frequency MIT system, which will be discussed in chapter 8.

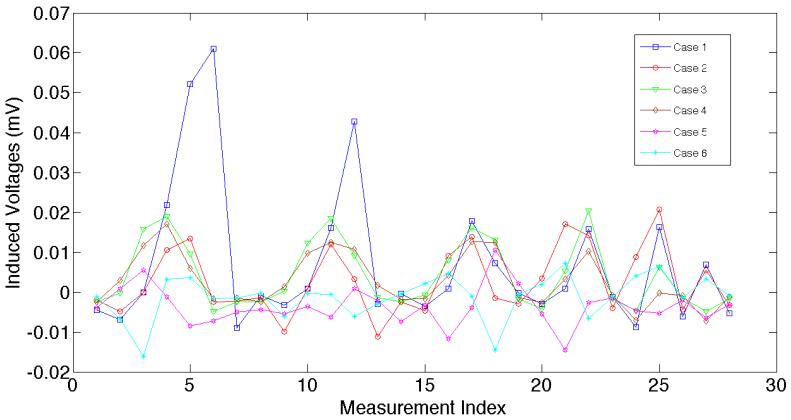

Figure 3.14: Comparison of induced voltages due to different testing profiles.

3.7 Discussion

This chapter investigates pipeline inspection using NPFM based MIT system as a case study of limited region tomography. The imaging region is limited to a pipe geometry and a novel localised algorithm NPFM is specifically developed for this geometry to improve MIT resolution. The experimental results demonstrate the capability of the proposed NPFM as a more suitable image reconstruction method compared to traditional PBRM. Experimental results demonstrate that external and internal wall losses of aluminium pipes as well as external wall losses of steel pipes can be successfully inspected. It is shown that a resolution of $10-15\%$ of the thickness of the pipes can be achieved using this proposed MIT methodology. More work is needed to remove the need for calibration against a full pipe dimensions, sensitivity to the locations of pipes and to further enhance the internal structure inspection of metallic pipelines.

The proposed NPFM can also be used to enhance the resolution of electrical capacitance tomography (ECT) for plastic pipelines. Due to the choice of the frequency and the skin depth effect, a resolution of 2% of the imaging region is the highest that can be achieved using a MIT system. However, as there is no eddy current effect in ECT, using this method could significantly improve the ECT image resolution.

There are two plastic pipe samples used in the following experiments; a small pipe sample with an external diameter of 88*mm* and an internal diameter of 76*mm*, and a larger pipe with an external diameter of 110*mm* and an internal diameter 90*mm*. The larger pipe is made from polybutylene, a thermoplastic with good mechanical properties and chemical resistance, and it is widely used for heating and plumbing applications in many properties. The smaller pipe is manufactured from polyethylene, commonly used in the corrosion-resistant piping and natural gas pipe system. The length of the small pipe and large pipe are 300*mm* and 113*mm* respectively. The schematic representations of the pipe samples can be seen in the first row in Figure 3.15. The schematic on the left contains defect of 25*mm* in length along the interior circumference and 2.5*mm* in depth, the 110*mm* diameter pipe in the middle has 2 defects, one defect spans 50*mm* on the interior circumference and the other 20*mm*, located opposite one another both with a 3*mm* depth. The 88*mm* diameter pipe on the right hand side has a defect of 1.5*mm* depth. The pictures of the samples are shown in the second row in Figure 3.15, the sensor array has a diameter of 150*mm*. The reconstructed images using both PBRM and NPFM for each case are shown in the third and fourth rows in Figure 3.15 respectively.

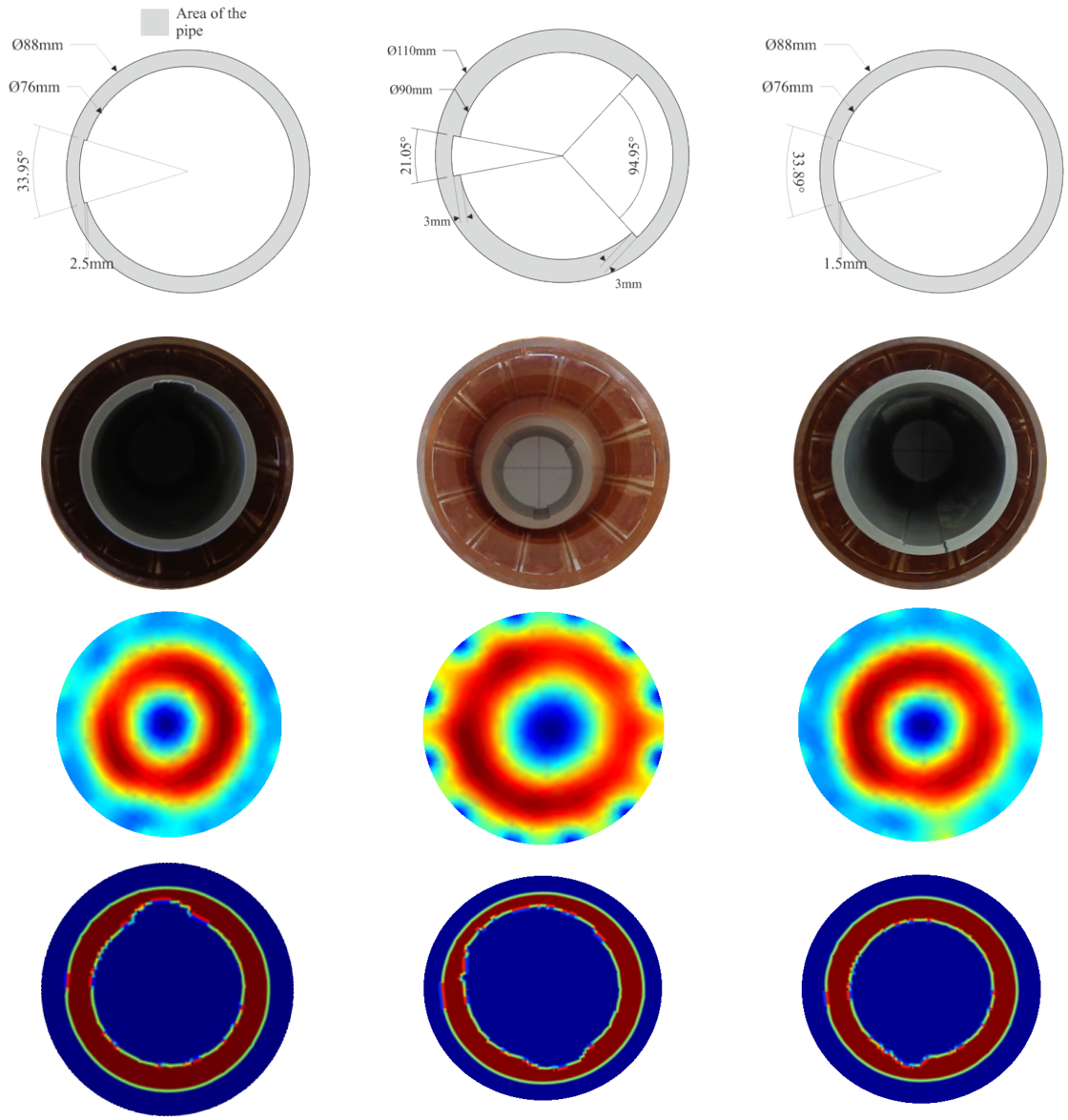

Figure 3.15: Inspection of defected plastic pipelines using NPFM based ECT system.

In terms of the size of sensor, the smallest measured defects when using a sample with two defects on is 0.29% of the cross sectional area of the imaging region. It can be seen that for the smaller pipe with 12*mm* thickness, a defect of 1.5*mm* can be reliably detected, this has a spatial area resolution of 0.195% of the imaging region. In all these cases, the PBRM could not give any useful information about the wall loss, and in all these cases the NPFM successfully locates the wall loss with the imaging defect size similar to the true wall loss. It is worth noticing that the ECT is sensitive to fluid inside of the pipe, so the same results can not be achieved if an accurate assumption can not be made about the distribution of permittivity inside of the pipe under inspection. At this stage the proposed method can only be used when the pipe system is empty. A wall loss covering only 0.195% of the ECT imaging area could be reliably detected. The resolution of 1.5*mm* depth in a tomography array of 150*mm* in diameter can be described as high definition imaging.

For the same NPFM method, the resolution achieved using ECT is approximately 10 times higher compared to the resolution achieved using MIT. This further validates the point made earlier that the proposed NPFM is an effective way of enhancing the resolution. The limitation associated with it when implementing pipeline inspection using MIT lies with the fundamental physics rather than the capability of this algorithm. However, there are several remaining issues need to be studied in this particular topic. How to obtain *a priori* information of the pipe in order to predefine the parameter in the NPFM algorithm remains a challenge. In oder to implement this pipeline inspection process, the sensitivity of the algorithm to the location of the pipe needs to be addressed. Moreover, the correct design and careful production of MIT sensors is the key in obtaining valuable measurement. Many parameters like coil size, wire gauge, number of turns, measurements frequency and source gain are important parameters to be determined. In particular there are many eddy current coil types each suited for a specific inspection task. It requires a certain level of experience to determine the right configuration.

In order to overcome the difficulties associated with the eddy current, the author propose the magneto-static permeability tomography (MPT) approach [44, 134]. MPT can reconstruct the permeability distribution of an object using magneto-static measurements. The data for image reconstruction are external magnetic field measurements on the surface of the object due to an applied magneto-static field. As there is no alternating current, there is no eddy current generated in the imaging object, the skin depth effect would not exist in this case. The permeability can be therefore reconstructed. The internal defect and corrosion in pipe with ferromagnetic materials could be potentially inspected.

In addition to our existing MK-I MIT system, we will aim to develop a 16 and a 32 sensor coil array, which can be used for inspection of large scale pipelines. Furthermore, a planar geometry based MIT study will be carried out as a limited access tomography for pipeline inspection. Both computational and experimental evaluations will be conducted for proposed sensor modalities to investigate the capability and limitation of MIT as a pipeline imaging technique.

Chapter 4

Hidden Defect Identification in Carbon Fibre Reinforced Polymer

Carbon fibre reinforced polymer (CFRP) materials pose new challenges to the non-destructive evaluation (NDE) techniques. This study addresses the issue of large defect identification in CFRP plates using electromagnetic measurements. A dual plane magnetic induction tomography (MIT) technique is proposed as a method for damage localisation in composite parts, where two arrays of planar sensors are utilised to measure the changes in induced voltages due to the changes in electrical conductivity properties. This geometry meets the requirements of damage inspection in plate structures and thus makes the imaging process feasible. The electrical voltage measurements are used as input to inversely map the spatial resolution of the samples in the region of interest. The stability and detectability of the dual plane system is examined using small metallic cubes. Both individual and multiple instances of damage embedded in CFRP samples are created as a representation of possible manufacturing defects. Experimental study shows that the presence of damage can be identified in both cases using dual plane MIT system. With advanced sensing design, rapid data collection unit and improvement in resolution, MIT could become a rapid NDE technique for the integrity inspection of the composite structures.

4.1 Introduction

A new breed of high strength material, CFRP, has found widespread application in commercial aircraft, industrial and transportation markets, where strength, stiffness, a lower weight, and outstanding fatigue characteristics are crucial requirements. Structural health monitoring of the CFRP such as missing carbon-fibre bundles, lanes, suspensions, fringes, missing sewing threads, angle errors and hidden manufacturing defects is an invaluable quality control. Many non-destructive evaluation techniques have been applied in this area to CFRP, including low frequency vibration [135], ultrasonic methods [136, 137, 138, 139], radiography [140, 141, 142], thermography [143, 144] and eddy current testing [145, 146, 147, 148, 149]. More recently, soft field tomography techniques have also

been used for damage detection in CFRP using electrical impedance tomography (EIT) [150, 151, 152]; however, the MIT-based research in this area remains very limited [153].

Although the image resolution of MIT is relatively low due to the fact that MIT image reconstruction is an ill-posed problem, this technique benefits from its contact-less, non-invasive nature and high temporal resolution. Firstly, there is no requirement for direct contact with the material being tested, such as with gels (various ultrasonic methods), specially designed probes (injected current thermography) or electrodes attached to the composite parts (EIT). Secondly, MIT, in using electromagnetic induction to map the spatial resolution, has a non-hazardous data collection process, whereas compared to X-ray computed tomography, radiation safety precautions need to be considered, which can in certain circumstances be impractical. In addition, using MIT alongside Kalman filters and 4D temporally correlated imaging permit rapid changes in electrical conductivity to be captured [96, 154], potentially enabling the functional analysis of CFRP structures, which is not currently feasible with any of the existing techniques.

As the carbon fibres in CFRP exhibit electrical conductivity, MIT could be a potential NDE technique providing a tomographic approach to traditional eddy current testing. MIT uses inductive coils to measure the induced voltages, which are associated with the passive electromagnetic properties non-linearly. The fundamental physics of MIT derive from the mutual inductance and eddy current theories. By passing an alternating current into an exciting coil, the sensing coil experiences a time-varying magnetic field. If materials with electrical properties are presented between this coil pair, the eddy currents arise in the conducting region, resulting in a perturbation in the magnetic field that can be sensed by the receiving coil. As such, the electrical properties can be revealed and the characteristics of the material presented in a reconstructed image, where the quality can be assessed visually. This technique has been applied in both biomedical and industrial processes [13, 19, 21, 155]. Overall, both MIT and eddy current testing techniques share many similarities - both arose from the same theoretical background (that of Faraday's law of induction, and subsequent eddy current theories) and as such have similar measurement principles, and both are used to image conductive or ferromagnetic materials. Nevertheless, the techniques differ in their operations and data processing. The MIT technique is a tomographic approach, utilising an array of sensors to provide a unifying tool to analyse the data, which makes the operation more robust, whereas eddy current testing targets a localised position using a pair of coils and requires a non-destructive testing specialist to carry out the testing.

In this study, a dual plane MIT is proposed for the identification of large area hidden damage in CFRP. This dual plane sensor arrays realise the imaging process in 3D, providing informtion about the geometry of the testing samples. This geometry can be potentially used in the inspection of production line at the manufacturing stage. The system resolution is evaluated through both simulation and experiments. Results of the inspection of embedded defects in CFRP are presented. With advanced excitation and sensing topology

[156], a fast data collection component and improved resolution, MIT could evolve to a rapid NDE technique for the structural health monitoring of CFRP.

4.2 Dual Plane Array

The dual plane array has been developed using two planar sensor arrays. The separation between the two arrays is $4cm$. Each array consists of 9 air-core cylindrical coils, which are arranged in a 3×3 matrix form. A non-conductive plate with a surface area of $14 \times 14cm^2$ is used to hold the sensors in place. Each coil has 100 turns, a side length of $3.4cm$, and the inner and outer diameters of the coils are $3.9cm$ and $4.1cm$ respectively (Figure 4.1a). The coil sequence of the first plane is shown in Figure 4.1b, the second planar array follows the same numbering system. It has previously been shown that slight misalignments between the receivers in the MIT system and the simulation model can cause up to 20% deviations in the conductivity perturbation [157]. Therefore, the dimensions of the coil and dual planar arrays are modeled according to the sensor design to ensure accuracy. The MIT measurement system block diagram is shown in Figure 4.2.

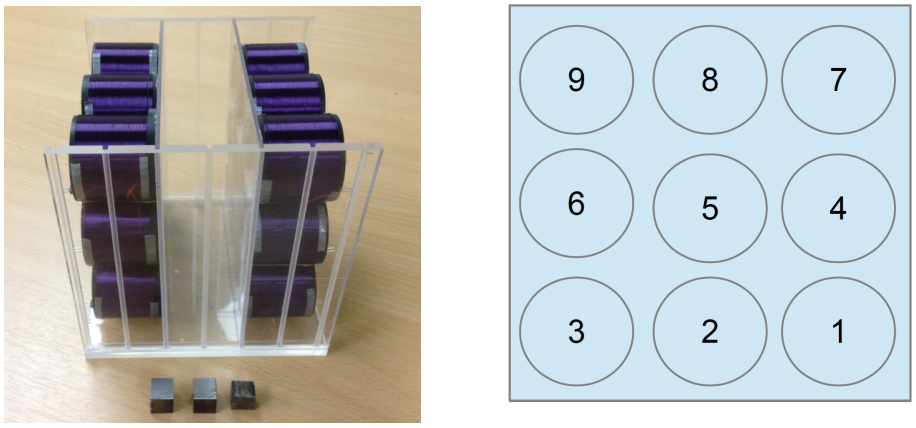

(a) (b)

Figure 4.1: (a) Dual plane sensor array, and (b) the coil sequence of the first planar array.

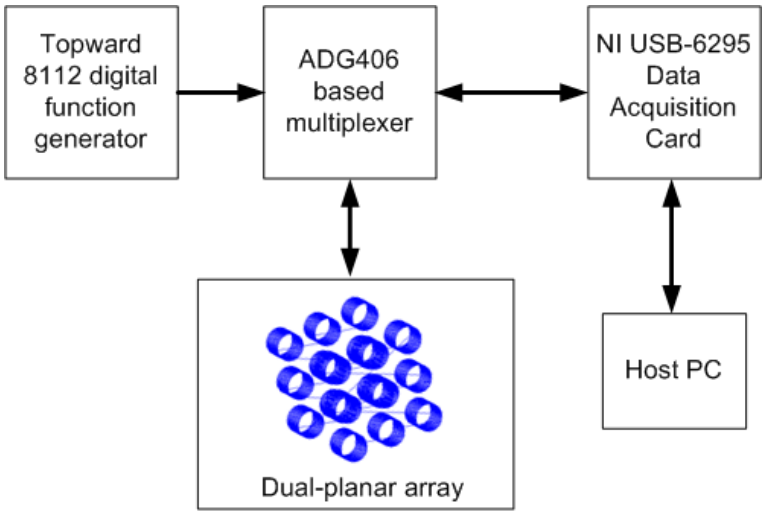

Figure 4.2: Block diagram of the dual plane MIT system.

4.3 System Analysis

This MIT system was initially developed for imaging materials with high electrical conductivity, such as metal. There are 153 unique coil pairs: 1-2, 1-3, . . . , 1-18, 2-3, 2-4, . . . , 17-18, resulting in a total of 153 independent measurements. The image reconstruction module extracts these measurements, performs the reconstruction algorithms, displays and updates the images. The signal to noise ratio (SNR) is taken to indicate the signal level of the system to the background noise level, which can be defined using an amplitude ratio as [158]:

$$SNR = 20log_{10}\frac{U_S}{U_N} \tag{4.1}$$

where U_S is the mean signal amplitude and U_N is the standard deviation of the measured signal amplitude. Due to the geometry of this system, the system SNR also depends on the separation of the two planar arrays. Figure 4.3 shows the SNR measurements with the first excitation coil when two planar arrays are separated at $2, 4, 6, 8$ and $10cm$ respectively, i.e., when coil 1 is excited with an alternating current, the voltage measurements are obtained from coil pairs $1-2$, $1-3$, ... $1-18$, and the corresponding measurements index are 1, 2, 3, ... 17.

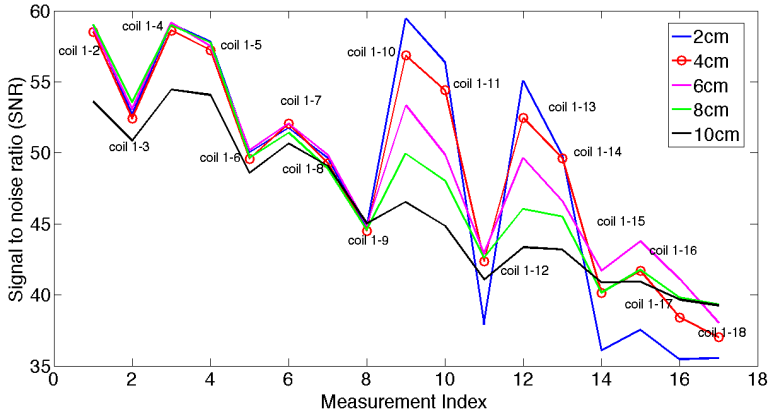

Figure 4.3: Signal to noise ratio, after the excitation of coil 1, for measurements obtained when the dual planes are separated by distances of $2, 4, 6, 8$ and $10cm$.

Several measurements are defined to analyse the system detectability, namely the neighbouring, opposite and diagonal measurement. The neighbouring measurement is used to describe the induced voltage measured from a pair of neighbouring coils that are in the same planar array (Figure 4.1b coil pair $1-2$ and coil pair $1-4$). The induced voltage measured from the coils directly facing each other is called the opposite measurement (coil pair $1-10$). The diagonal measurement refers to the induced voltage measured from any pair of coils that are located diagonally. This can be coil pairs either from the same planar array (Figure 4.1b coil pair $1-6$) or different planes (coil pair $3-16$). In this MIT study, the sensitivity maps demonstrate the relationship between the change in electrical properties and the voxel perturbation for a selected excitation/detection coil pair. It provides a visual approach to evaluate the system detectability in addition to the system SNR [61, 87, 24]. From a numerical point of view, the sensitivity map can be represented in a matrix form, which is also called the Jacobian matrix (equation 2.38).

Both front and side views of the sensitivity map for selected measurement pairs are shown in Figure 4.4, where Figure 4.4a shows the sensitivity contour for a neighbouring measurement, Figure 4.4b shows the sensitivity contour for an opposite measurement, and Figure 4.4c and 4.4d show the sensitivity contours for two diagonal measurements. In all cases, the sensitivity maps shown below are calculated for the free space scenario, i.e., there is no conductive materials presented in between. The mean sensitivity for each case is used for the isosurface contour plot. The level of sensitivity varies according to the orientation and distance of the coil pair, and the mean value gives an overall indication of the sensitivity across the region of coil coupling. The mean sensitivity value for coil pairs $1-2$, $1-10$, $1-9$, and $1-18$ are 52.76, 30.78, 8.61 and 1.38 respectively.

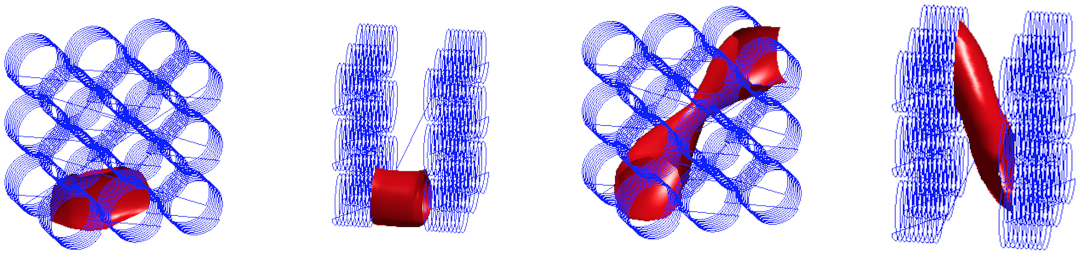

front view (a) side view (b) front view (c) side view (d)

Figure 4.4: Sensitivity maps for (a) a neighbouring measurement from coil 1 and 2, (b) an opposite measurement from coil 1 and 10, (c) a diagonal measurement from coil 1 and 9, and (d) a diagonal measurement from coil 1 and 18.

The neighbouring measurement has a higher SNR due to a closer distance between a neighbouring coil pair. The opposite measurements capture the material property change from a different plane. Compared to the neighbouring and opposite measurements, the diagonal measurements have relatively lower induced voltages and as such, result in lower SNR. However, the diagonal measurements contribute to the depth detection, which is an important parameter to characterise the properties underneath the surface. The higher SNR usually comes from the coils in the same plane (Figure 4.3), providing that the distance between neighbouring coils is smaller than the distance between opposite coils; as is the case in this study. This can be illustrated in Figure 4.5, showing the induced voltages from two planes $4cm$ apart. Taking the first cycle as an example, the strongest signal is due to the two neighbouring measurements – measurements 1 and 3, where the induced voltages of both are approximately $0.5V$ – and the highest measured voltage is induced between an opposite measurement – measurement 9, where the induced voltage is just over $0.1V$ – is almost 5 times lower than measurement 1.

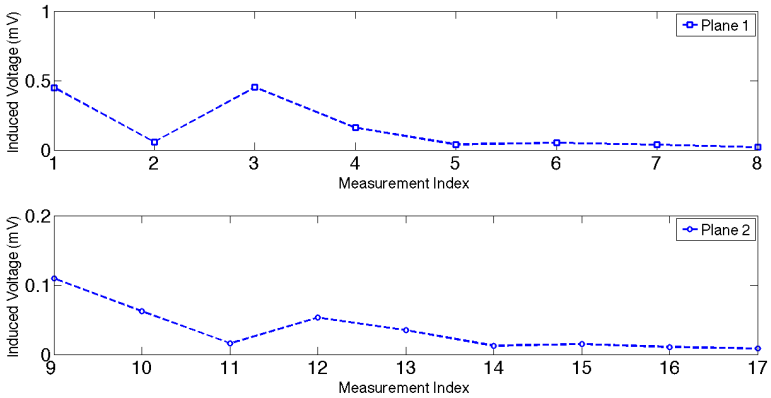

Figure 4.5: Measurements obtained from a dual plane of coils when coil 1 is excited, and the remaining coils are used as receivers.

To allow the signal to penetrate the material under testing, an appropriate operating frequency and separation between two planes of planar coils are required. It was pointed out in [159] that for a single planar MIT system with a similar experimental setup, one can

expect a maximum of $3-4cm$ of depth detection underneath the array. The driving frequency is an important factor in a MIT system. Lower frequency measurements penetrate the surface of the material and high frequency measurements thread around the surface of the material. In order to determine the suitable driving frequency, one needs to take the skin depth into consideration. In the quasi-steady electromagnetic field, the skin effect depth of general CFRP can be approximated by equation 4.2 [160]. As CFRP composites are nonmagnetic materials, the relative magnetic permeability of the CFRP is set to 1.

$$\delta = \sqrt{\frac{2}{\pi f \sigma \mu_0}} \tag{4.2}$$

where f is the driving frequency, σ is the electrical conductivity, and μ_0 is the unity permeability. With frequencies in the range of $10^4 Hz$, the skin depth of widely used CFRP is between $50-100mm$ [160], providing the electrical conductivity of the CFRP sample is within $10^3 - 10^4 S/m$. For the normal conductance of a metallic material, the electrical conductivity is higher than that of CFRP, which suggests that for the same given frequency, the skin depth of CFRP is larger than the eddy current penetration for metal. For a MIT system designed for metal detection, the driving frequency is usually around $5-100kHz$ [3]. This is a suitable operational range for the damage identification of composite material, in fact, if the system hardware allows, the driving frequency can be increased to the MHz range in an attempt to increase the system SNR. In the lower MHz frequency range, laminated CFRP composites can be assumed to be a homogeneous conductive material [161], and as such, it is feasible to use this dual plane MIT system for this application. In this study, the conductivity and the thickness of the CFRP samples are $2.1 \times 10^4 S/m$ and $10mm$ respectively (Figure 4.7), as derived from equation 4.2. The upper threshold of the operational frequency, necessary to allow the signal to fully penetrate the samples, is $241.24kHz$. Based on the nature of our in-house low frequency MIT system, design specification of the dual planar arrays, the SNR analysis, and the properties of the CFRP samples used in this study, a separation of $4cm$ between two planes and an operational frequency of $50kHz$ are determined for experimental evaluation.

Three metallic cubes are used in the following experiments to test the stability and detectability of the this system (Figure 4.1a). The top two rows in Figure 4.6 show the detection of two metallic cubes in three different locations in relation to each other. The dimensions of the cubes are $1.4 \times 1.4 \times 1.2cm^3$ and $1.2 \times 1.2 \times 1.4cm^3$ respectively. The remaining two rows in Figure 4.6 show the experimental results of a smaller individual sample under testing. The dimension of the cube is $1.2 \times 1.2 \times 1cm^3$. In all cases, the samples are placed between two planar coils. The samples have a conductivity of $1.45 \times 10^6 s/m$ and a relative permeability of 4000.

We use both slice visualisation and a 3D contour visualisation to present the reconstructed volumetric images (NOSER algorithm, equation 2.47), as shown in Figure 4.6. As the slice visualisation only provides a cross-section of the 3D image at a given location, this

does not entirely reflect the 3D shape of the reconstructed inclusion. As such, a 3D contour visualisation tool is developed to visually represent additional information about an inclusion. This visualisation takes the mean values of the raw reconstruction data and projects those values onto a mesh consistent with both the coil and the dual planar geometry. Only those values which exceed a threshold are highlighted, such that the artifacts are not represented. The threshold is variable and is informed by *a priori* knowledge of the tested material's location with respect to the sensor arrays. For the 3D contour images, the dual planar coils are simulated in addition to the reconstructed inclusion to demonstrate the positions of the inclusion in relation to the coils in free space. The same visualisation approaches are used for the remaining experimental results in this chapter.

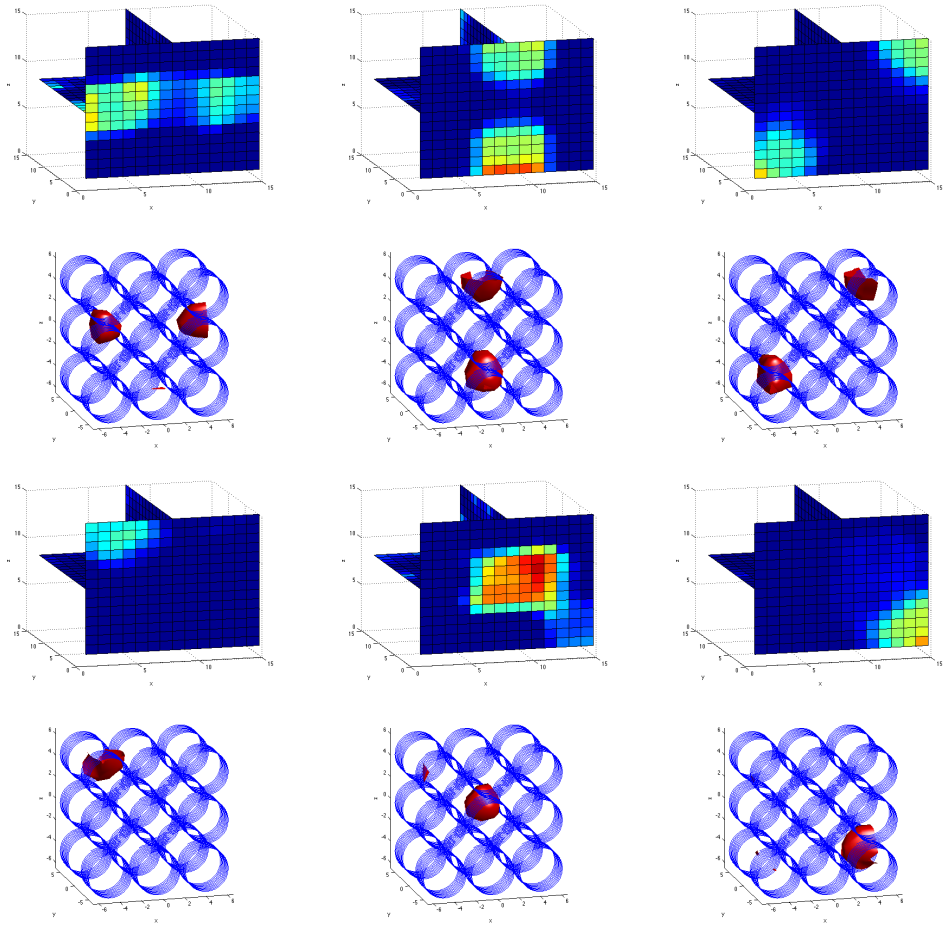

Figure 4.6: Detection of steel samples in different locations.

4.4 Inspection of Hidden Defect in CFRP

The CFRP samples used in this study are made of *HexPly* M21 epoxy matrix, which is a high performance, toughened epoxy resin system supplied in primary aerospace structures. The physical properties of the epoxy matrix are listed in Table 4.1. The hidden damages are created using polytetrafluoroethylene (PTFE) rings and embedded in the 10*mm* thickness samples. The core is comprised of 35 layers of laminates CFRP , and

is surrounded at each side by a further 10 layers of the same. An additional 10 layers are used to expand the sample to its final dimension of 10mm. Finally, a peel ply finish is applied to each side. The schematic representation of the CFRP samples are shown in Figure 4.7, where 4.7a shows a CFRP sample with one hidden defect in the centre, and 4.7b shows a CFRP sample with four hidden defects.

Fibre Mass (g/m^2)	194
Nominal Prepreg Mass (g/m^2)	294
Theoretical Calculated Cured Ply Thickness (mm)	0.184
Theoretical Calculated Fibre Volume $(\%)$	59.2
Resin Density (g/cm^3)	1.28
Fibre Density (g/cm^3)	1.78
Theoretical Calculated Laminate Density (g/cm^3)	1.58

Table 4.1: Physical properties of the *HexPly* M21 epoxy matrix.

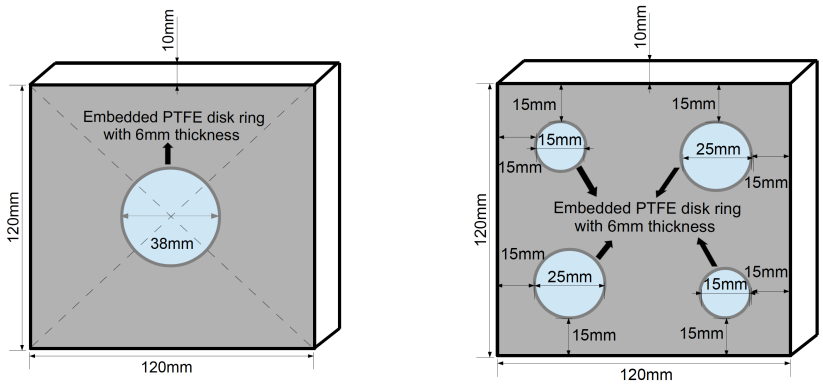

(a) (b)

Figure 4.7: CFRP samples with (a) one hidden defect, and (b) four hidden defects.

The reconstructed images for both CFRP samples are shown using sliced image and 3D contour images (Figure 4.8). The background measurement is taken from an undamaged CFRP sample with the same dimensions. This is the first step of calibrating of the input measurements in the inverse solver. The damages occur on the subsurface within the laminate architecture of the composite, which makes them invisible to inspectors. Therefore, in both Figure 4.8a and 4.8d, an approximation of the defected areas are marked in dashed line. In Figure 4.8b and 4.8e, the colour blue represent the CFRP samples with all other colours representing the damaged areas. For 3D contour images in Figure 4.8c and 4.8f, the highlighted red areas are the CFRP samples.

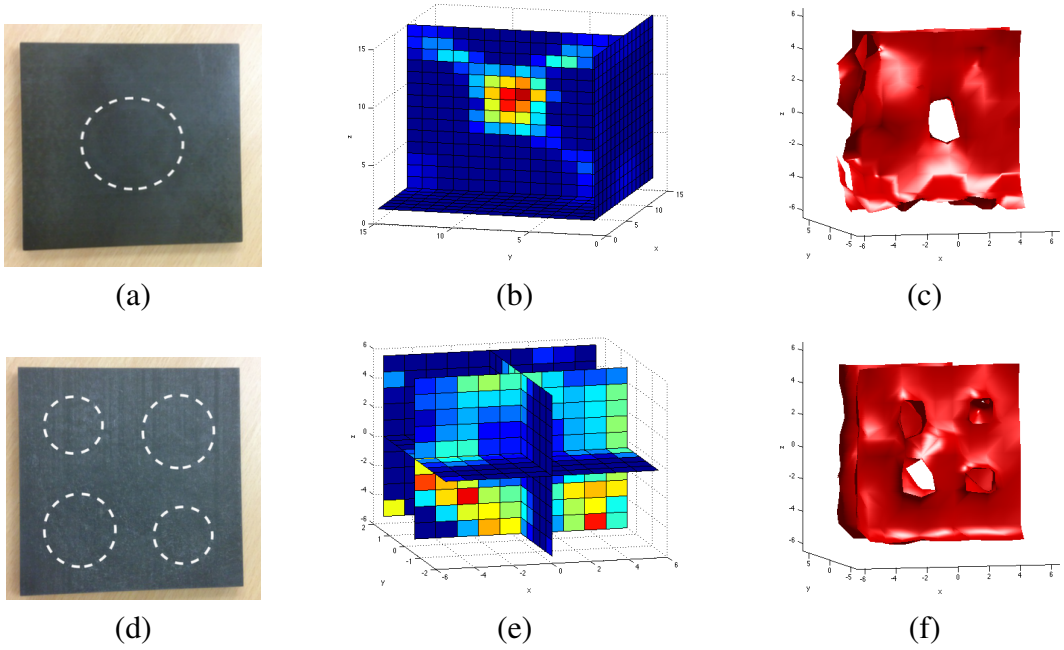

(a) (b) (c)

(d) (e) (f)

Figure 4.8: CFRP samples with one and four defects (a and d, respectively), alongside their reconstructed images using slice visualisation (b and e, respectively), and 3D contour visualisations (c and f, respectively).

4.5 Discussion

A dual plane MIT system is proposed for the identification of hidden defects in CFRP. The MIT system used in this study is initially tested using metallic samples. The fundamental physics and the mathematical solving process of MIT are studied to extend this technique in the area of CFRP inspection. The system stability and detectability is analysed through both simulation and experiments. Metallic samples as small as $1.2 \times 1.2 \times 1cm^3$ can be imaged using this dual planar MIT system in an imaging region of $14 \times 14 \times 4cm^3$, i.e., we can detect samples that constitute 0.18% of the total region of interest. The experimental results show that different sizes and locations of hidden damage in CFRP plate can be identified using the proposed MIT system with the given sensor geometry and experimental setup. A hidden defect as small as 0.74% of the total volume of the CFRP plate under inspection can be achieved, which is 0.14% of the imaging region. The CFRP samples used in this study are considered to have isotropic conductivity. The skin depth calculation shows that higher frequencies (up to a maximum of $241kHz$ in this case) can be used to improve the system SNR and consequently lead to a higher imaging resolution. However, due to the low resolution of this technique, the size differences of the defects cannot be distinguished at this stage of the research. Nevertheless two samples are not sufficiently representative to cover all possible manufacturing defects or impact damage which may occur in real industrial environment. For examples, the impact damage could result in an altered electrical conductivity, which might not be as high contrast as the conductivity changes shown in this work. This study represents the proof of principle for MIT

as a viable means to be developed as an in-service structural health monitoring technique for CFRP. Further development in this application are needed, including the study of MIT sensor array topology, the development of multifrequency excitation, the design of a rapid data handling unit and computational modeling of the forward and inverse problems for anisotropic eddy currents. These will be subjects of our follow up studies, in addition, the high temporal resolution MIT will be investigated for the functional analysis of the real time imaging of the CFRP structures.

Chapter 5

Planar 3D Near Subsurface Imaging

Eddy current methods are widely used for non-destructive evaluation (NDE) in inspection of metallic structures. Eddy current based NDE uses a single coil or a pair of coils to scan the samples. As an emerging NDE technique, MIT scans the sample with a coil array through an eddy current based tomographic approach. In this chapter, a planar array MIT system (PMIT) is proposed for 3D near subsurface imaging. This is of great importance as there are large numbers of potential applications for MIT that allow limited access to the materials under testing. The system development, practical implication, capability and limitations of PMIT are discussed. The fundamental principles are demonstrated through simulations. Experimental data are used to evaluate the capability and detectability this system as a potential 3D subsurface imaging tool.

5.1 Introduction

Magnetic Induction Tomography (MIT) is an emerging non-destructive evaluation technique that is able to map passive electromagnetic properties without causing material damage. In recent years, MIT has had applications ranging from biomedical imaging to industrial inspection. Many previous MIT systems were developed using coils that are arranged around the imaging periphery [18, 59, 61, 162]. This type of coil arrangement has a circular geometry and free access around the complete periphery, thus full access tomography can be achieved. However, there are numerous applications where access is restricted and non-invasive measurements can only be taken from one surface [87]. Consequently, the imaging process cannot be carried out by using a MIT system with a circular or near circular sensor array. Planar geometry can overcome this difficulty. As such, recent research has focused on developing planar sensors and estimating near-surface material properties using them [163, 164]. Inspecting product quality using planar sensors is also possible [165, 166]. A simulation study of planar MIT was reported in [87], where the 2D cross-sectional images of conductive bars were obtained using a simultaneous iterative reconstruction technique. Paper [167] presented a planar MIT system for the detection of conductivity inhomogeneity on the surface of a metallic plate. The sensors

were placed in a circular shape with their axes perpendicular to the plate. The 2D images were reconstructed using experimental data. It was shown that a spatial distinguish ability of $10-20\%$ of the array diameter was possible. In this chapter, a planar MIT (PMIT) is developed as a type of limited access tomography, which realises 3D reconstruction for near subsurface imaging. Recently, we have developed a 3D volumetric MIT system [83], and the techniques developed in 3D MIT enabled the development of a 3D PMIT, which offers an insight into the structures underneath the sensors by depth detection. The observations in this chapter can be extended to other types of tomography and inverse problems [168, 169, 170, 171, 172, 173, 174, 175]. The development of planar sensor model and system setup are presented, followed by simulation results and experimental evaluation. The chapter presents the first 3D PMIT study for subsurface imaging. The PMIT has two main advantages over traditional scanning based eddy current NDE methods. Firstly, PMIT employs an array of coils so that the scanning speed can be improved. Secondly, measurements from non-neighboring coils offer greater depth detection compared to single coil or double coil based eddy current scanning techniques, which will help to gain information about the materials under testing.

5.2 Planar Sensor Array

The planar sensor array consists of 16 air core cylindrical coils. 16 coils are arranged in a 4×4 matrix array and placed on a plastic square board with a surface area of $18\times18cm^2$. The thickness of the plastic board is $t=0.3cm$. The distance between each coil is $0.3cm$. The important parameters for this sensor model are listed in Table 5.1. Figure 5.1 (a) shows the coil dimensions and Figure 5.1 (b) shows the arrangement of coil sequence. A top view of the planar sensor array is shown in Figure 5.2. The block diagram of this system is shown in Figure 5.3.

Parameters	Value
Number of coils	16
Number of turns for each coil	100
Inner diameter for each coil: d_i (cm)	3.9
Outer diameter for each coil: d_o (cm)	4.1
Coil height: H (cm)	5
Coil side length: l (cm)	3.4
Self-inductance of each coil (μH)	380

Table 5.1: Sensor model parameters.

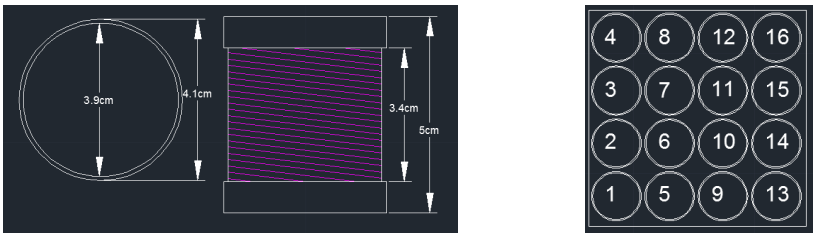

(a) (b)

Figure 5.1: (a) coil dimensions, (b) coil sequence.

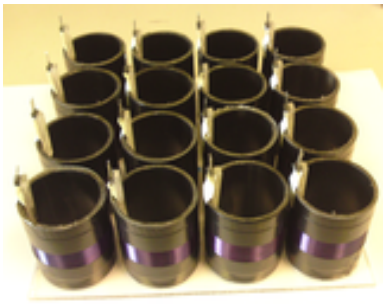

Figure 5.2: Top view of a 4×4 planar coil array.

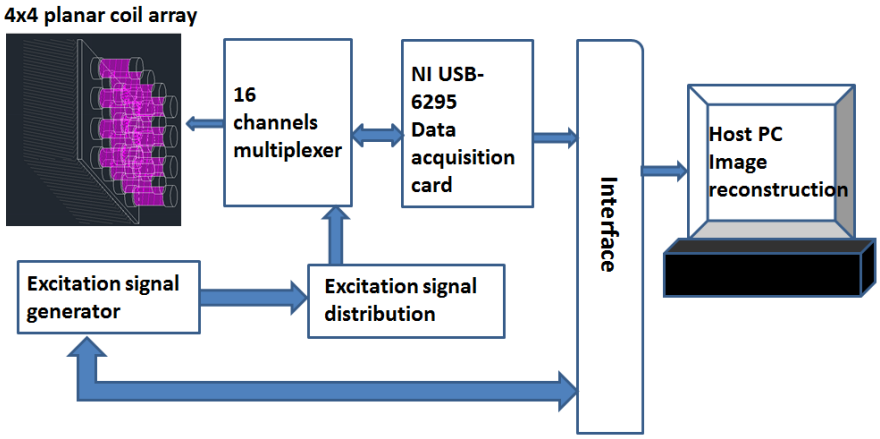

Figure 5.3: Block diagram of the proposed PMIT system.

The signal to noise ratio (SNR) is taken to indicate the signal level of this system to the background noise level, which can be defined using amplitude ratio as [158].

$$SNR = 20log_{10}\frac{U_S}{U_N} \tag{5.1}$$

Where U_S is the mean signal amplitude and U_N is the standard deviation of the measured signal amplitude. It can be seen from Figure 5.4 that for the coil arrangement showing in Figure 5.1 (b), the highest SNR of this PMIT system is $63.1dB$ (for measurement between coil 1 and coil 2) and the lowest SNR is $33.4dB$ (for measurements between coil 1 and coil 16).

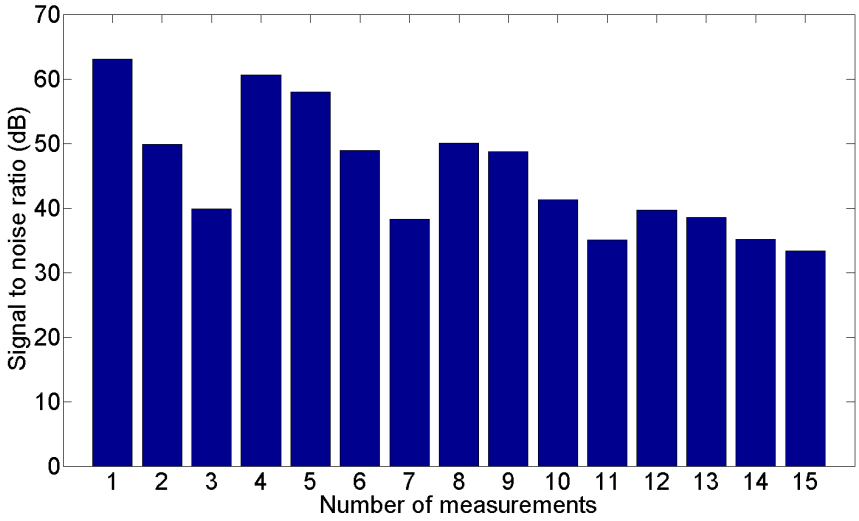

Figure 5.4: Signal to noise ratio of first cycle measurements when first coil used as excitation.

5.3 Method

In the previous section, the SNR is shown to indicate the signal level of the PMIT system. In this part, the sensitivity map will be used to evaluate how a pair of coils couple with each other. The sensitivity map of the electromagnetic imaging problem describes the system response to every voxel perturbation for a selected excitation/detection coil pair [61, 87, 24]. When the coils are close together, the system is sensitive to the surface layers, and as the coils become further apart, the sensitivity penetrates deeper underneath the object under testing [87]. This can be demonstrated by Figure 5.5, where a selection of sensitivity maps of this system are shown. When receiving coils are at an increased distance from excitation coils, a relatively larger sensitive region and a greater penetration can be observed in the system response. A decreased sensitive contour can also be observed due to the decreased strength of signals from the receiving coils. This can be seen in Figure 5.5 (c), showing a pair of coils with the greatest distance between them. The sensitive contour in Figure 5.5 (c) has the deepest penetration and the largest area, but the sensitivity in the middle is lower compared to other patterns, as shown in Figure 5.5 (a) and Figure 5.5 (b).

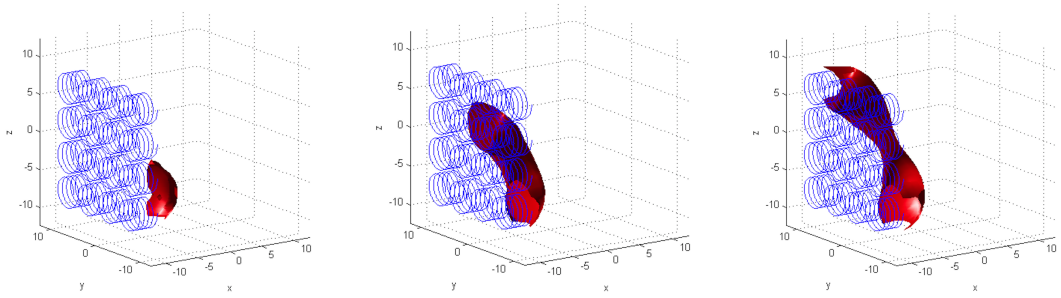

(a) (b) (c)

Figure 5.5: Sensitivity map coupling between: (a) coil 1 and coil 2, (b) coil 1 and coil 11 and (c) coil 1 and coil 16, the coil number sequence can be seen in Figure 5.1 (b).

In this study, a standard Tikhonov regularisation method (equation 2.48) is used as an inverse solver to calculate the conductivity distribution according to equation 2.48. Note that the column vector consisting of 120×1 changes of induced voltages, the conductivity column vector representing changes in $19^3 \times 1$ voxels, the sensitivity map is a 120×19^3 matrix of the sensitivity field, which can be calculated using equation 2.38.

5.4 Simulation and Experimental Evaluation

5.4.1 Detectability of PMIT System

The PMIT is a challenging 3D inverse problem, in particular, because of limited access to the object. The simulations presented in this section are used to study the underlying inverse problems in the context of a linear model. The end view of a number of simulation models are presented in Figure 5.6 to evaluate the capability and detectability of the PMIT system. The planar sensor array is simulated in (x,z) plane at $y = 0$. The first column in Figure 5.6 shows the simulated inclusions in different locations. The second column in Figure 5.6 includes the reconstructed images for each simulated case. The reconstructed 3D contour images in the third column in Figure 5.6 provide an insight as to where the inclusion is with respect to the planar sensor array.

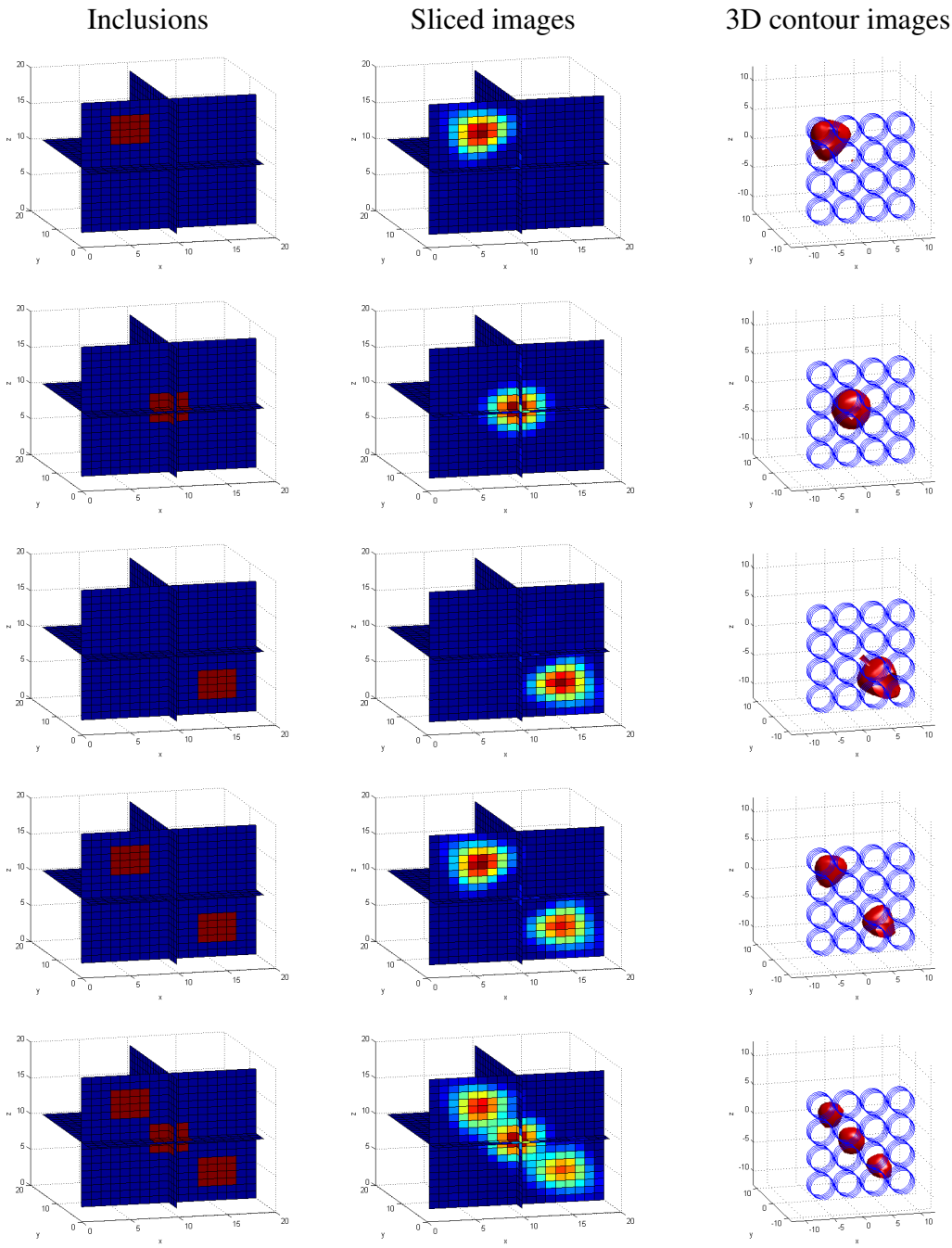

Figure 5.6: Detectability of PMIT using simulated data.

Aluminium rods of diameter 40mm are used as test samples in our experiments to validate the simulations. These rods have a high electrical conductivity of $3.5 \times 10^7 S/m$ and a relative permeability of 1. The first column in Figure 5.7 shows the positions of true aluminium rods in relation to the planar sensor array. The second column in Figure 5.7 shows the reconstructed images for each selected position. The reconstructed 3D contour images are included in the third column in Figure 5.7, where the end view of the rod positions with respect to the planar sensor model are shown. In these experiments, the aluminium rods are located against the planar sensor array with a fixed distance to the sensors. This fixed distance can be written as: $D_f = (H-l)/2+t = 1.1cm$, where H and l are the height and the side length of each coil sensor, and t is the thickness of the board

(Table 5.1).

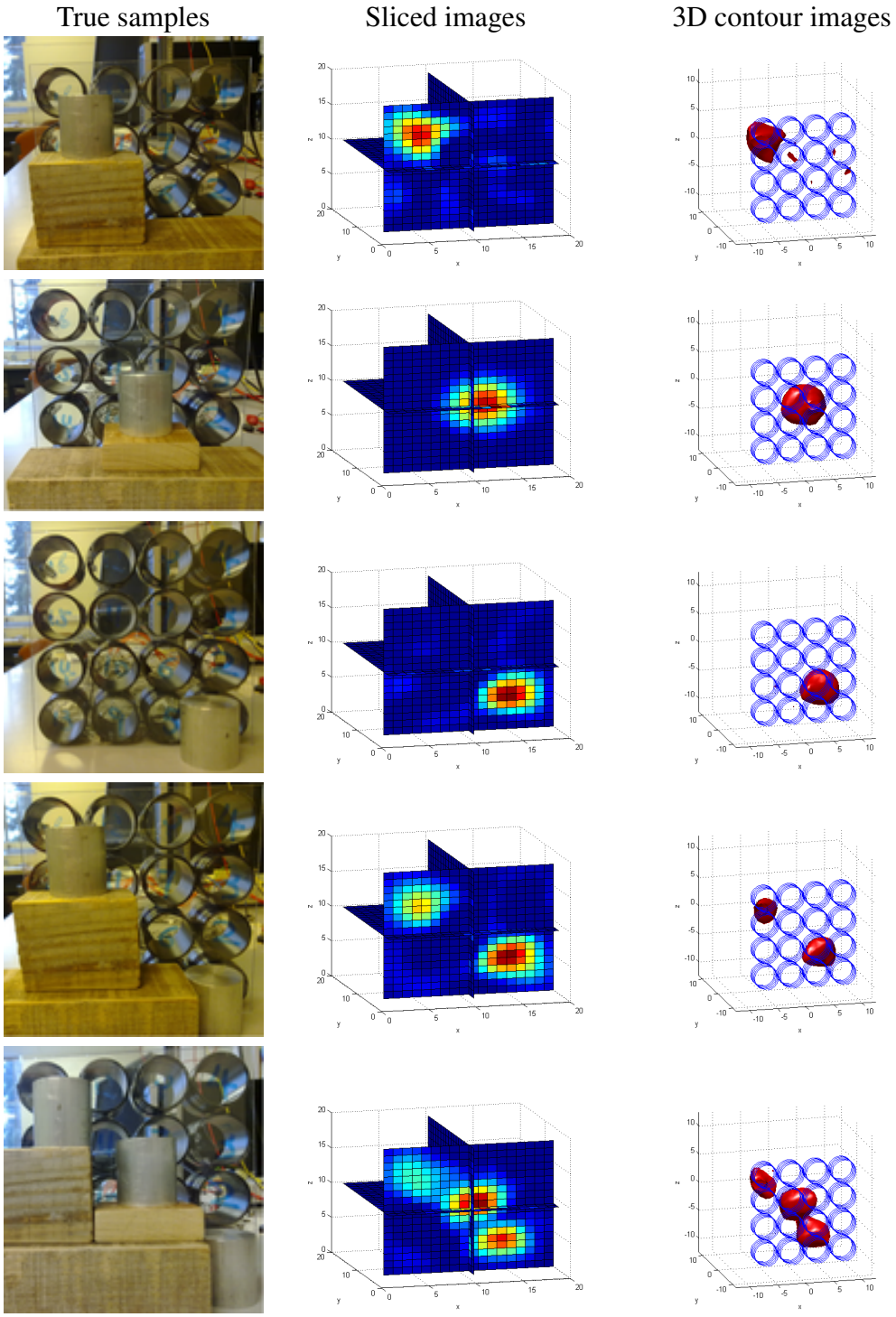

Figure 5.7: Detectability of PMIT using experimental data.

5.4.2 Depth Detection of PMIT System

In the previous section, we investigated the detectability of the PMIT system in terms of different positions using simulations and experiments. It was shown that this PMIT system is capable of detecting objects that are close to the sensors. For subsurface imaging, the imaging depth is a key parameter to assess the capability and detectability of

this PMIT system. Therefore, a series of simulations and subsequent experiments are completed for this purpose.

In Figure 5.8, the top view of the simulation models are shown to demonstrate the principle of near subsurface imaging using PMIT system. The planar sensor model is simulated in (x,z) plane at $y = 0$. The first row in Figure 5.8 shows one simulated inclusion with highlighted lines indicating the distance between the sensors and the inclusion at four selected depths: $y = 3$, $y = 5$, $y = 8$, and $y = 10$. The second row in Figure 5.8 presents the reconstruction of one inclusion at each selected depth. The same simulation procedures are adopted for simulating two inclusions, as shown in the third row in Figure 5.8. The reconstructed images are demonstrated in the bottom row in Figure 5.8. It can be seen from Figure 5.8 that the image quality degrades as the depth increases.

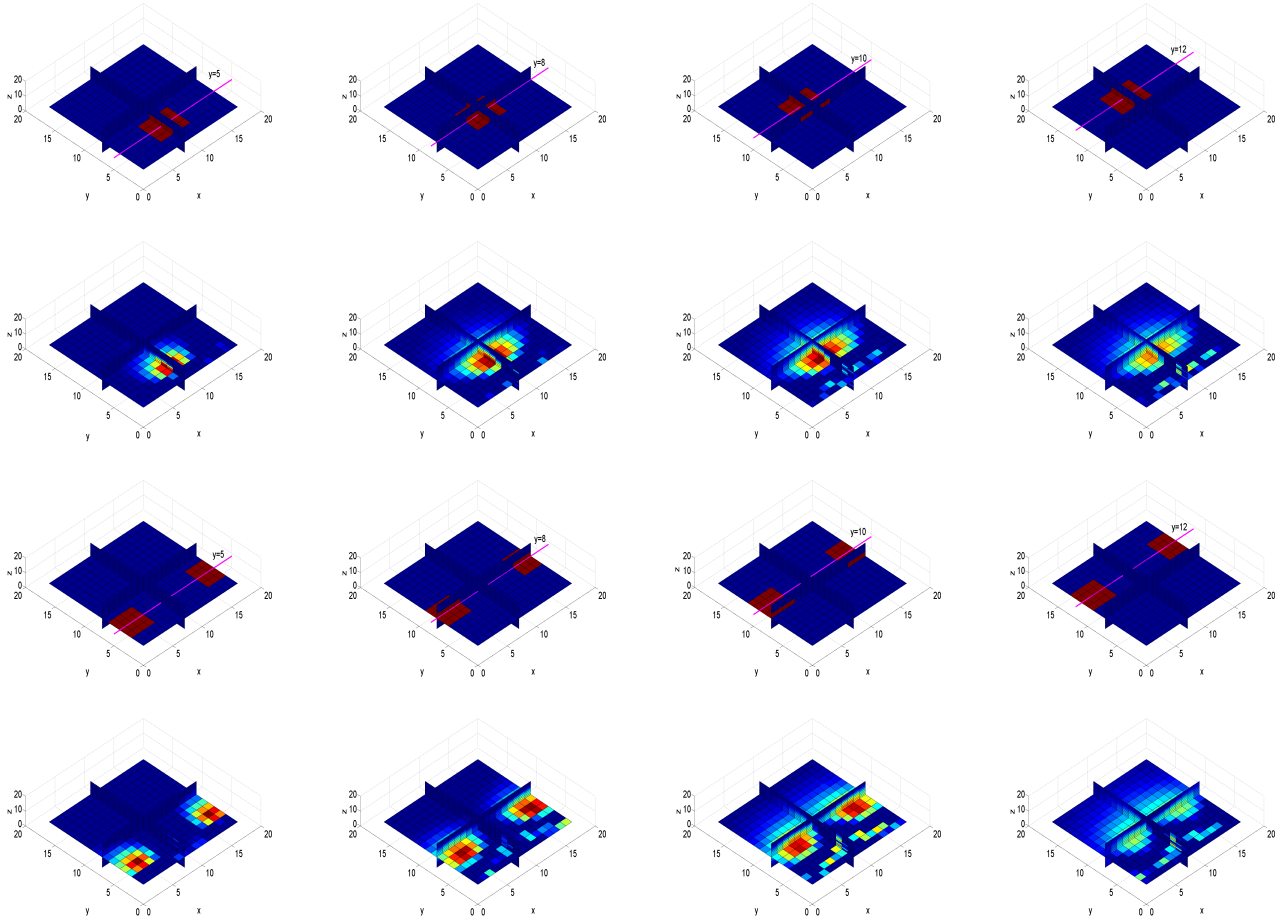

Figure 5.8: Depth detection using simulated data.

We have solved the inverse problem and detect a maximum imaging depth of $8-10mm$ using simulations. In order to verify the simulation models and evaluate the detectable depth of the PMIT system using measured data, two sets of experiments are completed. Same aluminium rods are used as test samples.

Figure 5.9 presents the experimental setup and the reconstructed images using one rod for subsurface imaging. The first row in Figure 5.9 shows the top view of the true samples with respect to the planar sensors.

As mentioned in section 5.4.1, there is a fixed distance of $D_f = 1.1cm$ between the sensor array and the samples due to the construction of the sensor model and the thickness of the board. Although short, it is crucial to take this distance into consideration when evaluating the depth of this system, as it poses an additional barrier for eddy current in MIT, particularly as the skin depth is limited under a driving frequency of $50kHz$. Therefore, it cannot be neglected. The structure and layout of the sensor model need to be considered carefully if a highly accurate system is required. The moving distances from the planar sensors D_m are: $0cm$, $1cm$, $2cm$, $3cm$ and $4cm$ respectively. Therefore, the total distance between the true sample and the front of the sensor array is $D = D_f + D_m$. The sliced images and 3D contour images for each depth are presented in the second and third row in Figure 5.9.

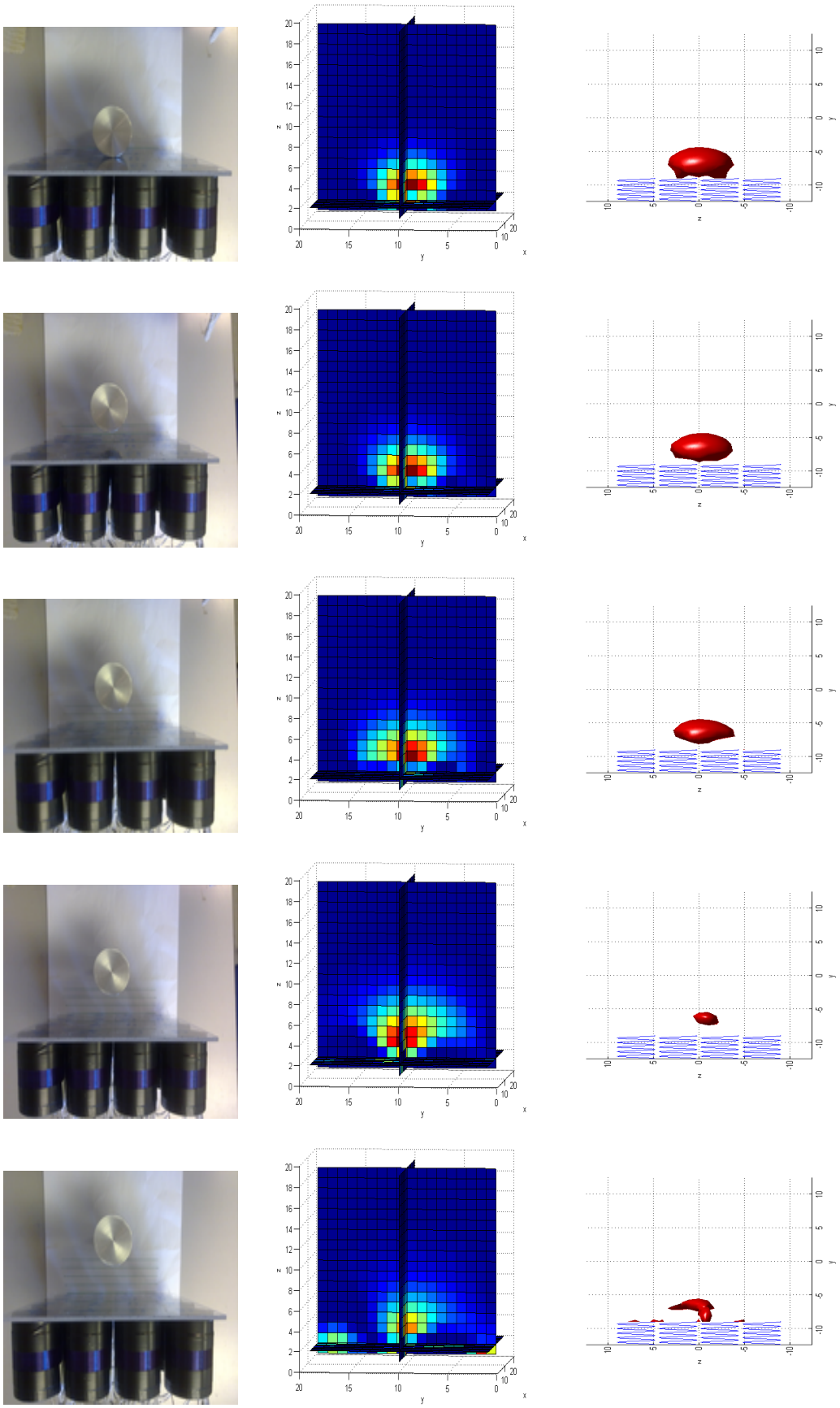

Figure 5.9: Depth detection using one object.

The same experimental procedures are repeated using two rods, as shown in Figure 5.10. The distance between two aluminium rods is 4cm. The true samples, sliced images and 3D

contour images are shown in the first, second and third rows of Figure 5.10 respectively.

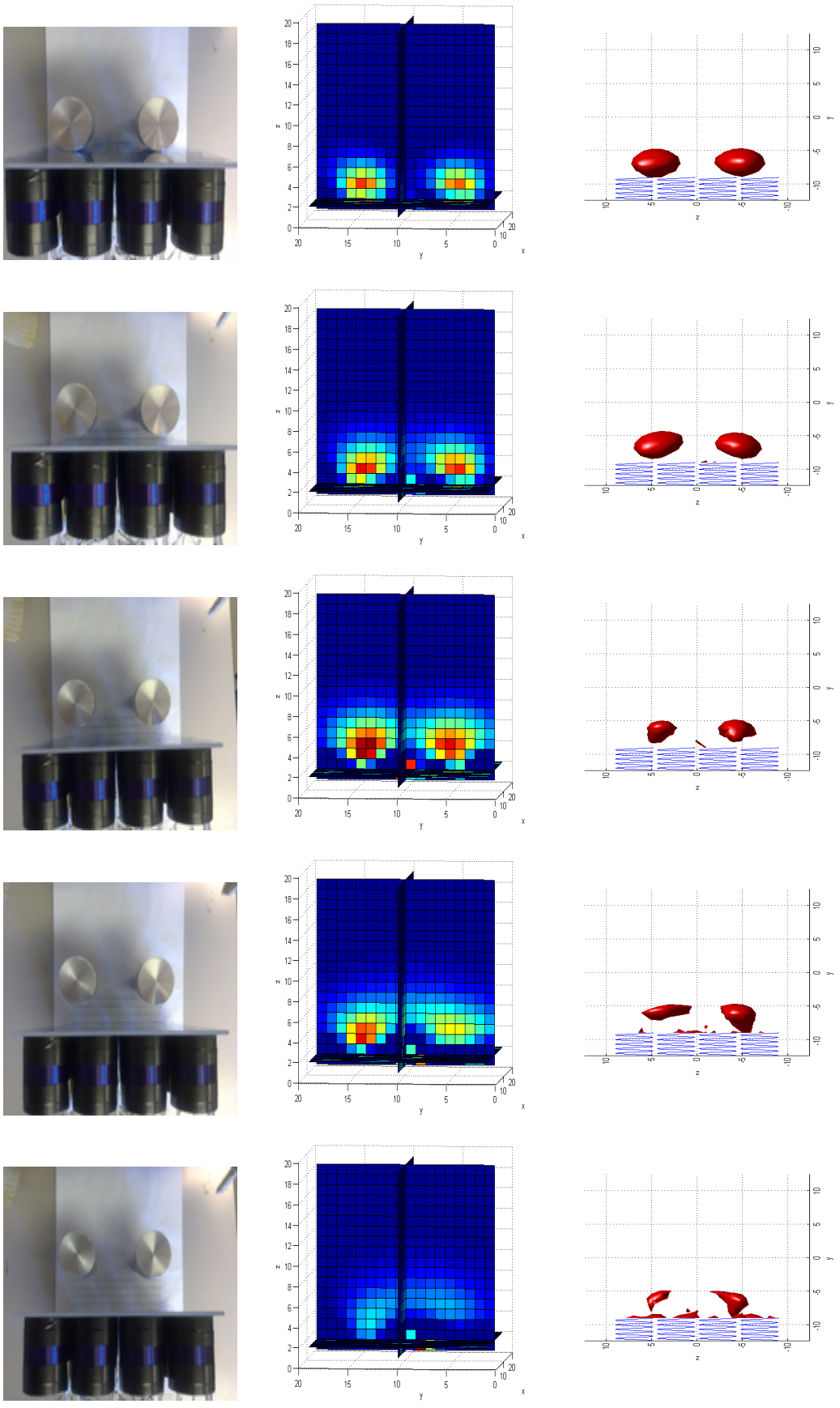

Figure 5.10: Depth detection using two objects.

5.4.3 Quantitative Evaluation of Depth Detection

Both simulations and experiments produce satisfactory reconstructions for object(s) close to the sensor array. In this section, we introduce an image quality parameter: volume deformation ratio (VDR) to examine the image quality degradation using experimental data for object(s) distanced from the sensor array.

It can be seen from Figure 5.9 and Figure 5.10 that image reconstruction algorithms usually reconstruct a circular image to match the true object, and display it in a position that matches the true position of the target. As the object is distanced from the planar sensors, the system becomes less sensitive, and the measurements become less accurate. In this case, image algorithms will create a larger spherical image to represent the true target, resulting in artifacts around the boundary of the reconstructed image [176]. Therefore, the volume changes in reconstructed images due to the distance between sensors and objects under testing can be used to assess the image quality.

In order to calculate the VDR, a reference volume and a threshold are required. Both simulations and experiments have shown that this PMIT system can detect object(s) close to the sensors, and can reconstruct satisfactory images. Therefore, we take the reconstructed image at this state (i.e., $D_m = 0cm$) as a reference image, and calculate the total volume of the inclusion(s) in the reconstructed image as a reference volume. The volume change $\triangle v$ in the reconstructed image is proportional to the distance change $\triangle d$ between the test sample(s) and the planar sensors within certain range. Finally, the slope $\frac{\triangle v}{\triangle d}$ can be used to represent the deformation rate. Let the threshold of VDR be 50%. If VDR is greater than 50%, we consider the reconstructed image to be too distorted to be of use.

The definition of VDR can be written in the following manner:

$$VDR = \mid \frac{v_i - v_{ref}}{v_{ref}} \mid \tag{5.2}$$

where v_i is the volume of the inclusion(s) in the reconstructed image with the object(s) placed at i cm away from the planar array. The v_{ref} is the reference volume, which is taken from the volume of the reconstructed inclusion(s) with the object(s) placed are very close to the sensors (i.e., $D_m = 0cm$).

The volume of the inclusion(s) in reconstructed image can be calculated using the following equation [176]:

$$v = \frac{\sum[\triangle\sigma_k \geq \frac{1}{4}max(\triangle\sigma)]}{\sum_1^i \triangle\sigma_i} \tag{5.3}$$

where $\triangle\sigma_k$ represents a voxel which has an amplitude greater than one-fourth of the maximum amplitude in the reconstructed image. Note that in the numerator, a threshold of one-fourth is chosen, which is the total number of voxels that contribute to most of the significant visual effects in the reconstructed image [176]. The denominator is the total number of voxels in reconstructed image. As each voxel has the same volume, the total

volume of voxels can be calculated using the total number of the voxels.

It can be seen that from equation 5.2 that if a reconstructed image is severely ill-posed, the VDR can be inaccurate as the total volume of the voxels might be extremely large ($v_i = +\infty$) or small ($v_i = -\infty$), or just happen to be the same as the reference volume ($v_i = v_{ref}$). In these cases, the VDR is not representative any more and cannot be taken into consideration for image quality assessment.

A threshold of 50% is chosen as the purpose of the experiments is to find the object(s) under testing rather than to examine the accuracy of the depth detection of our PMIT system. The threshold can be set lower if a higher sensitivity and accuracy are required.

Moving distance	$1cm$	$2cm$	$3cm$	$4cm$
VDR one object	1.54%	15.74%	41.48%	53.60%
VDR two objects	12.01%	42.55%	51.45%	56.13%

Table 5.2: Volume deformation ratio.

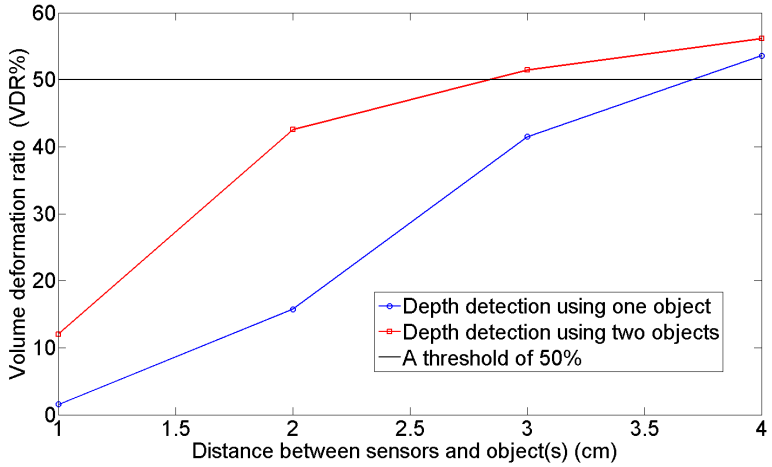

Figure 5.11: Graph of volume deformation.

5.5 Discussion

It can be seen from Figure 5.6 and Figure 5.7 that the PMIT system is capable of detecting both single and multiple conductive objects, which are placed with an approximate fixed distance of $1cm$ away from the sensors. However, the reconstructed images using experimental data showing in Figure 5.7 are generally compromised compared to the results presented in Figure 5.6.

A number of simulation models in Figure 5.8 demonstrate the principles of near subsurface imaging using a PMIT system. It can be seen from Figure 5.8 that a depth of $8-10mm$ can be achieved through simulations. This further validates our system sensitivity analysis, as presented in Figure 5.5, where the sensitive contour does not penetrate

more than 10cm into the imaging region. The experimental results presented in Figure 5.9 and Figure 5.10 reveal that the PMIT system can detect a depth of approximately $3-4mm$ beneath the planar array.

It is clear from the 3D contour images shown in Figure 5.9 that the true sample can only be detected partially as the distance from the sensors increases. Moreover, comparing the reconstructed images from two sets of experiments for evaluating depth detection, a rapid degradation in image quality can be observed in Figure 5.10 compared to the results in Figure 5.9. This image degradation is also quantitatively evaluated through an image quality measure VDR, as shown in Table 5.2 and Figure 5.11. The VDR of the reconstructed image at incrementally increased distance of 1cm for one object is 1.54%, while the VDR for two objects at the same distance away from planar sensors is 12.01%, significantly higher. As the distance is increased to $3cm$, the VDR for two objects exceeds the threshold of VDR, which means the reconstructed image is severely degraded. However, this degradation in image quality is not associated with the number of objects under testing. The system detectability depends on the distribution of the sensitive region and the locations of the object(s) under testing.

In general, uniform detectability can be observed in the region that is close to the sensors. As the imaging depth increases, the sensitivity degrades from uniform detectability. The detectable area can be considered similar to a spherical region due to the decreased signals between coil pairs that are further away. It is shown in Figure 5.5 (c) that the measurement from the furthest coil pair contribute to most of the significant depth. However, the furthest coil pairs also have the lowest SNR, as shown in Figure 5.4, which means the sensitivity of such a coil pair is reduced compared to the sensitivity of neighbouring coil pairs. As the object moves further away from the planar sensors, the overall sensitivity decreases. The areas that are close to the edge of the planar array is comparatively less covered by the sensor array. Hence, the sensitive region tends to have a trapezoidal or spherical shape, as shown in Figure 5.12.

The level of detectability between simulated and measured data differs for two reasons: noise in measured data, and the skin depth effect. In this study, at a driving frequency of $50kHz$, aluminium has a skin depth of approximately $366\mu m$ [18], which is far less than the diameter of the aluminium rod. This results in the eddy current threading on the surface of the object. As such, very little information can be obtained from the back of the test sample. The simulated models do not have issues associated with depth penetration as a linear model is assumed.

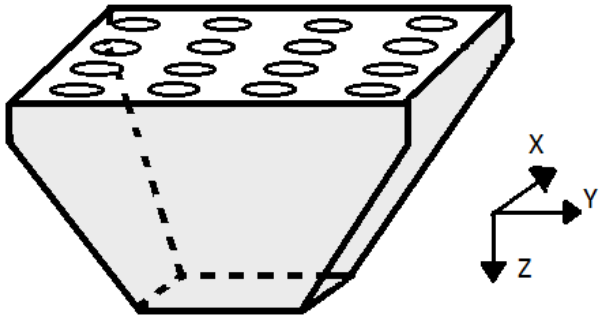

Figure 5.12: The distribution of sensitive region against the imaging depth.

This chapter investigates the capability and detectability of a novel PMIT system. This geometry makes it possible to study the near subsurface imaging using an eddy current method. It is a very challenging imaging setup as access to the targeted object is limited to one surface only. The fundamental principles are verified through simulation studies. Experimental results detect a limited depth in this PMIT system. Nevertheless, it demonstrates the potential this system has as a non-invasive subsurface imaging tool. In our future work, we will aim to improve the depth detection by developing a multi-frequency PMIT system. Non-linear image reconstruction in 3D PMIT will also be a subject of our future study.

Chapter 6

Evaluation of the Missing Data Effect

6.1 Introduction

Pipeline inspection using traditional MIT system with a circular coil array is studied in chapter 3. The circular coil array provides a circular geometry and free access around the complete periphery, where full access tomography can be achieved in laboratory conditions. However, in real life situations, there are situations where access is highly restricted, consequently the imaging process can hardly be implemented by using a traditional MIT system with circular or near circular sensor array.

In this chapter, a new 32-sensor coil model is developed to study the effect of the missing data on the quality of reconstructed images in MIT [177]. Missing data can be caused by undersampling measurements in order to achieve fast speed tomography process or because of limited angle/access to the targeted object(s) being imaged. The MK-I MIT system with 32 sensors provides a data set consisting of 496 measurements, where some of the data might be missing due to the nature of the imaging objectives. To examine a range of missing data sets, two experimental scenarios are completed: undersampling measurements and limited angle imaging. The former is carried out by evenly activating 4, 8, and 16 sensors from 32 sensors and the latter is investigated by using limited angles of 45°, 90°, 180°, and 270°, compared to 360° full angle imaging. An edge finite element method is used to calculate the forward problem and a linear algorithm is implemented as an inverse solver to reconstruct images. An image quality measure is adopted to quantify the effect of missing data on MIT image quality through experimental evaluation. The results are evaluated qualitatively and quantitatively.

This chapter gives an insight to what to expect from limited angle imaging and highlights the challenges related to this. For pipeline inspection, we propose a combination of limited angle and limited region tomography, which could improve the MIT reconstructions.

6.2 MIT System with 32 Sensors

The MK-I system with a 32-channel coil array is shown in Figure 6.1. Each coil has a diameter of 20*mm*, a side length of 34*mm* and 205 turns. 32 air-cored and double layered coils are constructed to form a region of interest (ROI) of 210*mm* diameter. Figure 6.2 shows a top view of the 32-sensor coil array. The SNR in this MIT system is between 40*dB* (for measurement between two opposite coils) and 56*dB* (for measurement between two neighbouring coils) at an operation frequency of 50kHz. Figure 6.3 shows the SNR of first cycle measurements.

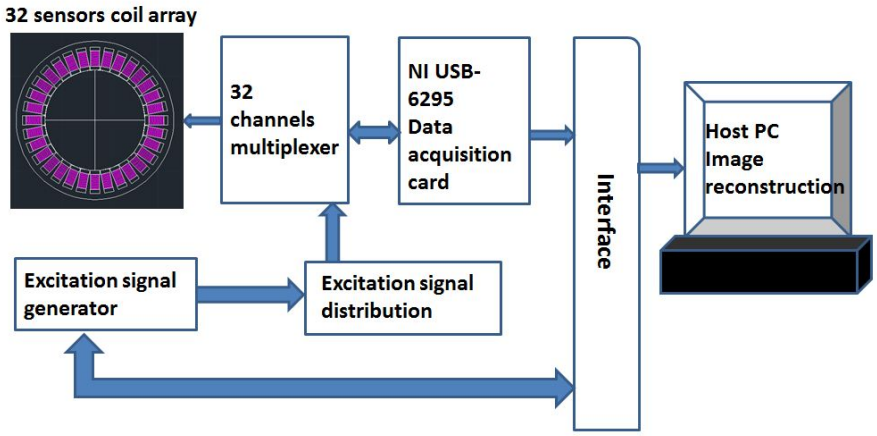

Figure 6.1: MK-I MIT system with a 32-sensor coil array.

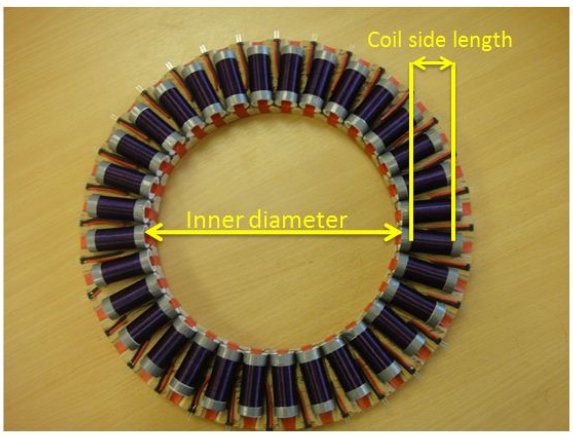

Figure 6.2: Top view of the 32-sensor coil array.

Number of sensors	32
Number of measurements	496
Inner diameter of coil array (*mm*)	210
Coil side length (*mm*)	34
Coil diameter (*mm*)	20
Number of turns for each coil	205
Operational frequency (*kHz*)	50
Coil design	Air core and double-layer coil

Table 6.1: Specifications of 32-channel MIT system.

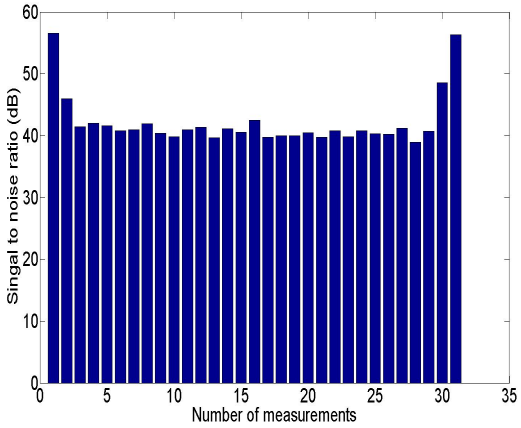

Figure 6.3: Signal to noise ratio of first cycle measurements when first coil used as excitation.

6.3 Experimental Results

6.3.1 Experiment Setup

It is known that for an array of N transceivers (coil modules functioning as either exciter or sensor) fixed in position, $N(N-1)$ measurements will be possible. As these consist of reciprocal pairs, the number of independent measurements will be $M = N(N-1)/2$. If only S number of sensors are selected, the total number of missing data points will be $M^{'} = M - S(S-1)/2$.

In scenario one, the missing data profile is generated by undersampling measurements from a full data set of 496 measurements. Evenly spaced 4, 8 and 16 sensors are undersampled individually from a 32-sensor coil array. This way, the dimension of the ROI remains unchanged, the only changing parameter is the number of sensors, which links the image quality directly to the missing data profile. Table 6.2 shows the relationship between the number of sensors and the missing data profile, as well as the sensor layout for each undersampled case.

Number of sensors (N)	4	8	16	32
Measurements (M)	6	28	120	496
Missing data ($M^{'}$)	490	468	376	0
ROI in diameter (mm)	210	210	210	210
Coil layout	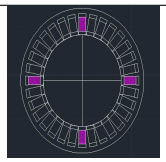	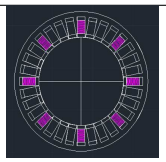	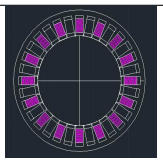	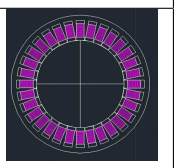

Table 6.2: Scenario one: Undersampling measurements.

In scenario two, we consider missing data through limited angle imaging, which could happen due to limited access to imaging samples. In this study, several limited angles are systematically considered to evaluate the effect of missing data has on the imaging process and image quality. Physical angles of 45°, 90°, 180° and 270° angles are evaluated respectively and compared to the 360° full access imaging. In this scenario, 4, 8, 16, 24 and 32 sensors are implemented to realise the imaging process. It is worth noticing that the sensors are activated in sequence to form an arc of selected angle. This is the fundamental difference between undersampling scenario and limited angle scenario. Table 6.3 shows the relationship between limited angle and the missing data profile, as well as the coil layout for each selected angle.

Number of sensors (N)	4	8	16	24	32
Measurements (M)	6	28	120	276	496
Missing data ($M^{'}$)	490	468	376	220	0
Angle (degree)	45°	90°	180°	270°	360°
Coil layout	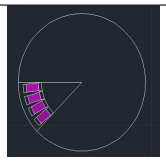	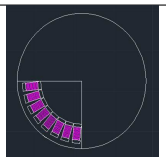	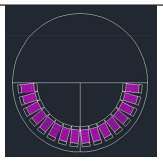	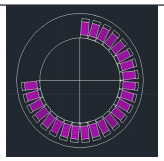	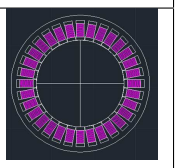

Table 6.3: Scenario two: Limited angle imaging.

In scenario one, the distance between neighbouring coils increases as the number of undersampled sensors decreases; which means the measured voltages between neighbouring coils become lower compared to full data case. The measured voltages between opposite coils however remain the same for all undersampled cases due to unchanged dimension of ROI. The undersampling process results in the sensitive area being shifted towards the central area and consequently the boundary area becomes less detectable.

For scenario two, limited angle imaging, the ROI varies according to the selected angle, which provides an unequal sensitivity compared to full angle imaging. However, with the boundary areas being closer to the sensing coils, these areas become more sensitive and detectable compared to the central location.

6.3.2 Undersampled Data Imaging

A large aluminium rod of 88*mm* diameter is used in the central location for single object imaging, while smaller aluminium rods of diameter 64*mm* are used in other locations in multiple objects imaging. The aluminium rods have high electrical conductivity of $3.5 \times 10^7 S/m$ and relative permeability of 1. For single object detection, a large rod is placed in the centre of the ROI in order to obtain equal sensitivity from undersampled sensors. For multiple objects detection, smaller rods are uniformly distributed in the ROI for the same reason. The reconstructed images presented in Figure 6.4 show high conductivity contrast between air and metal. In this chapter, the inverse problem is solved using a linear Newton one step error reconstruction (NOSER algorithm, equation 2.47). The chosen regularisation parameters are included in Figure 6.4 for all cases.

It can be seen from column 4 in Figure 6.4 that the MIT system with 32 sensors is capable of detecting a single object and separating multiple objects. This is under the circumstance of zero missing data; all 496 measurements are used to reconstruct images. Column 3 in Figure 6.4 shows the reconstructed images from the MIT system with undersampled 16 sensors, where only 120 measurements are undersampled to reconstruct images. The undersampling process makes the channel switching and data collection operation faster compared to the full data case. Moreover, comparing the reconstructed images of one and two rods using undersampled 16 sensors and 32 sensors (shown in the second and fourth row in Figure 6.4), the image quality degradation due to undersampling data process can hardly be observed. However, as the number of imaging objects increases, the image quality starts to degrade. For the reconstruction of three and four rods using undersampled 16 sensors, the images are blurred. As the number of measurements from the missing data profile increases to 468 in the case of undersampling 8 sensors, the system can not map the conductivity distribution accurately. Although the time consumption for image reconstruction is reduced, the final images are not favorable as shown in the second column in Figure 6.4. The first column of Figure 6.4 shows the reconstructed images, where only 4 sensors are undersampled, the number of missing data is increased to 490. There is no useful information but noise gained.

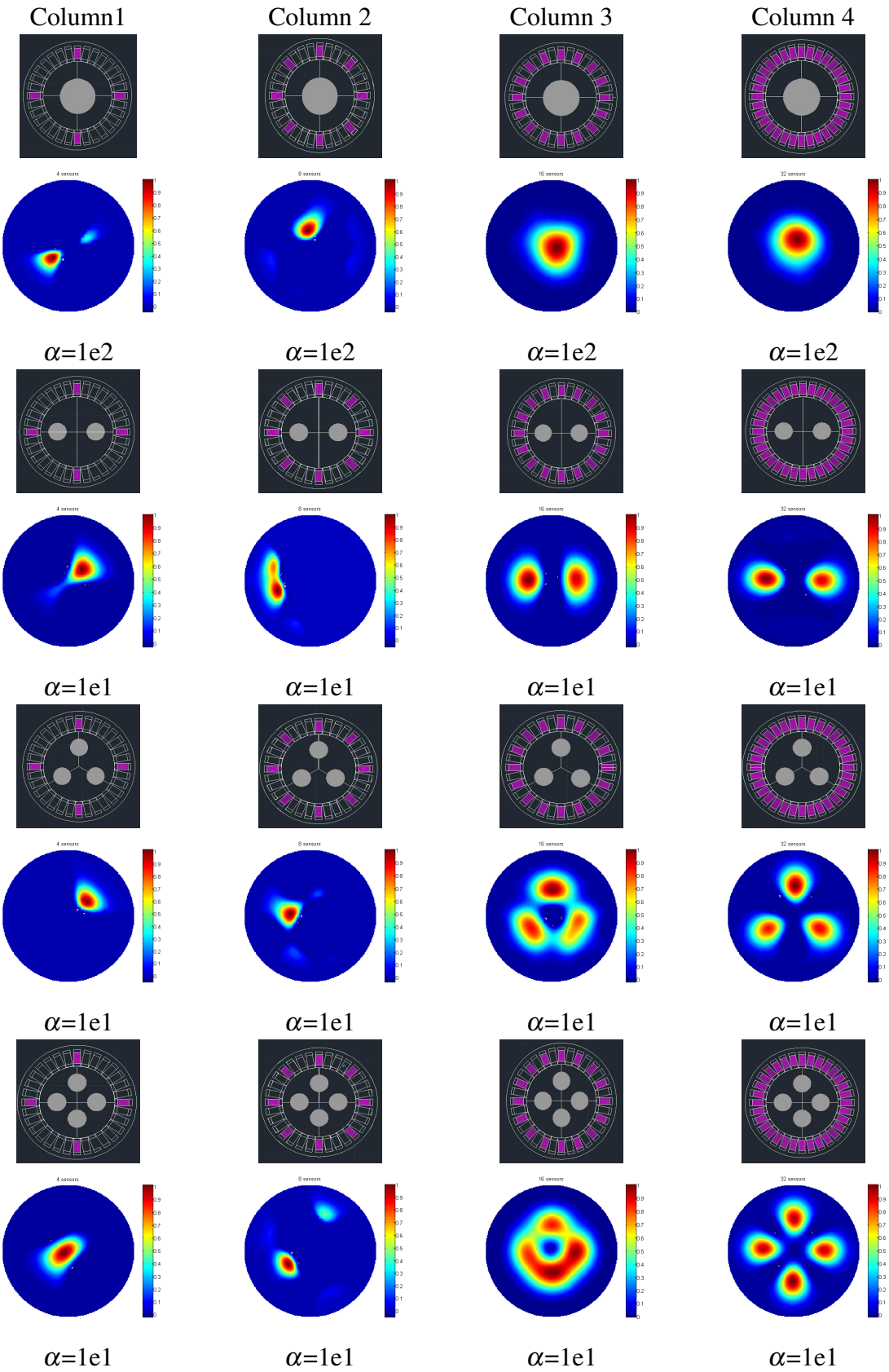

Figure 6.4: Single and multiple objects detection using undersampling data.

It is known that only singular values that are above the noise level contribute to the final images [81]. In order to compare the number of singular values above the noise level, the most noisy scenario is considered, which is the measurement with lowest SNR for

all cases. The singular value decay combined with the noise level provides a useful tool in terms of information content. Figure 6.5 indicates the level of information loss due to undersampling of the measured data. The number of singular values above the noise level for cases of 32, 16, 8 and 4 sensors are 101, 48, 21 and 6 respectively. It is proved that as the amount of missing data increases, the number of singular values contributing to the final image reduces and hence the degradation in image quality that can be seen qualitatively in Table 6.4.

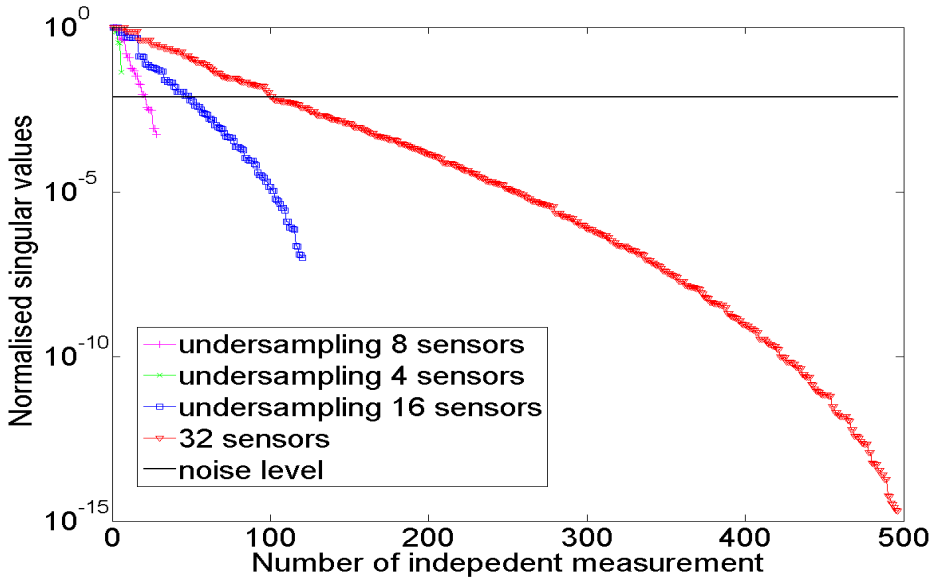

Figure 6.5: Singular value decay for undersampled measurements.

In this study we have filled the available surrounding area with 32 coils so that we can study the effect of missing data and the undersampled cases are chosen from the same coil array. This should not be confused with how a MIT system with 8 or 16 sensors could have performed in different scenarios with different dimensions of sensor and ROI [86, 178].

To further quantify the resolution loss due to missing data, an image quality parameter resolution (RES) is adopted to assess the image quality numerically. The RES measures the ratio of the image pixel amplitudes that contribute to the most visually significant effects to the total image pixel amplitudes in reconstructed image [176]. It can be defined as:

$$RES = \sqrt{\frac{a_q}{a_0}} \tag{6.1}$$

where $a_q = \sum_k [x_k \geq \frac{1}{4} max(x_k)]$, x_k represents each pixel in the reconstructed image, and a_0 is the total image pixel amplitudes in reconstructed image. A square-root is taken so that RES gives length ratios rather than area ratios, RES should be close to 1 in order for the technique to more accurately represent the true area of the conductivity distribution [83]. This is a useful measure when the image quality improvement or degradation can not be observed directly from the reconstructed images. For example, the reconstruction

of one and two objects using undersampled 16 sensor and full 32 sensors shown in Figure 6.4. Note that the RES value is valid and can be used to analyse the image quality numerically under the condition of an acceptable image being reconstructed from a MIT system. It is shown in the first and second column in Figure 6.4 that the MIT system with undersampled 4 and 8 sensors cannot accurately map the conductivity distribution of the test materials, there is only noise obtained. The RES values under these cases are not valid and therefore not shown in Table 6.4. The RES values are compared between the case of undersampled 16 sensors and 32 sensors case. Table 6.4 shows that the values of RES decreases as the quantity of missing data increases from 0 to 376 for both single and multiple objects detection. This gives an indication of resolution loss due to undersampling process.

N	$M^{'}$	RES one objects	RES two objects	RES three objects	RES four objects
32	0	0.9412	0.9484	0.9233	0.8991
16	376	0.9389	0.9374	0.8855	0.8537
8	468	-	-	-	-
4	490	-	-	-	-

Table 6.4: Image quality parameter with respect to undersampled measurements.

In addition to seeing the effect of missing data on image quality, 1D graphs of conductivity distribution are plotted, taking two objects detection as an example. The conductivity intensity values are normalized against the maximum value for each case. Figure 6.6 shows the 1D graphs using undersampled 16 sensors, 32 sensors, compared to the true case. Similar 1D plots for undersampled 4 and 8 sensors are not shown here because of the highly inaccurate images that result. As we are using a linear one step reconstruction algorithm, the 1D graph is used to show the separation of two inclusions in the reconstructed images. It can be seen from the graph that both the MIT system with undersampled 16 sensors and the full set of 32 sensors are capable of separating two inclusions side by side. This indicates that for this particular case, undersampling 16 sensors can achieve a reasonable image quality. Although undersampling 16 sensors has an advantage of reducing the data collection time, the conductivity distribution of the reconstructed image using 32 sensors is more closer to the true case. This shows the compromise between image quality and hardware complexity as well data collection time.

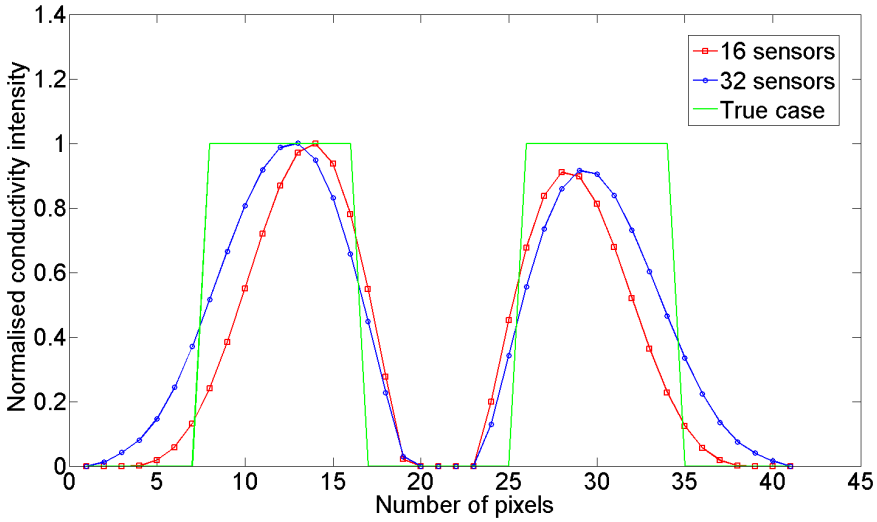

Figure 6.6: Graph of 1D conductivity distribution for undersampled 16 sensors and full 32 sensors; referring to two objects detection in Figure 6.4.

6.3.3 Limited Angle Imaging

This section studies the missing data effect due to limited angle imaging. 32 sensors form a circular imaging region with 360° coverage, where all the measurements are implemented to reconstruct images. For limited angle imaging, 4, 8, 16 and 24 sensors are arranged in arcs to form 45°, 90°, 180° and 270° respectively. Comparing to undersampling data scenario, where the ROI remains unchanged for all cases; the ROI in a limited angle scenario is confined to a limited angle coverage and it varies according to the selected angle. Aluminium rods of 64 mm diameter are used in the following experiments. Figure 6.7 includes reconstructed images using different angles and the chosen regularisation parameters for each case. The fifth column in Figure 6.7 shows that both single and multiple objects can be successfully detected through 360° imaging. As the number of missing data is increased to 220, imaging of four objects can not be reconstructed with an angle of 270°, however, limited angle of 270° has demonstrated its capability of imaging up to three objects, shown in the fourth column in Figure 6.7. The results presented in the third column in Figure 6.7 show that imaging of one or two objects is possible through 180° imaging. With the number of missing data further increases to 468 and 490, it can be seen from the second and first column in Figure 6.7 that limited angle of 90° and 45° can only image one object.

This experiment validates a hypothesis that the object is detectable under the condition that the object is placed in the ROI, which is the area within a limited angle. Of particular interest is the rod detection using 45° imaging, where one object placed in the ROI is successfully detected, which would be otherwise impossible for traditional MIT system with equally spaced 4 sensors coil array. Furthermore, comparing the image results included in the second column in Figure 6.4 and the second column in Figure 6.7, where limited angle of 90° is shown capable of detecting one object within its coverage, while

undersampling 8 sensors does not provide useful information. Noticing that the number of sensors and the number of measurements are the same for both cases. Limited angle tomography is required when there is limited access to the object to be imaged, however, this comparison indicates that if *a priori* knowledge about the position of the object was known, limited angle imaging could be useful as it allows more sensors to be populated around the ROI.

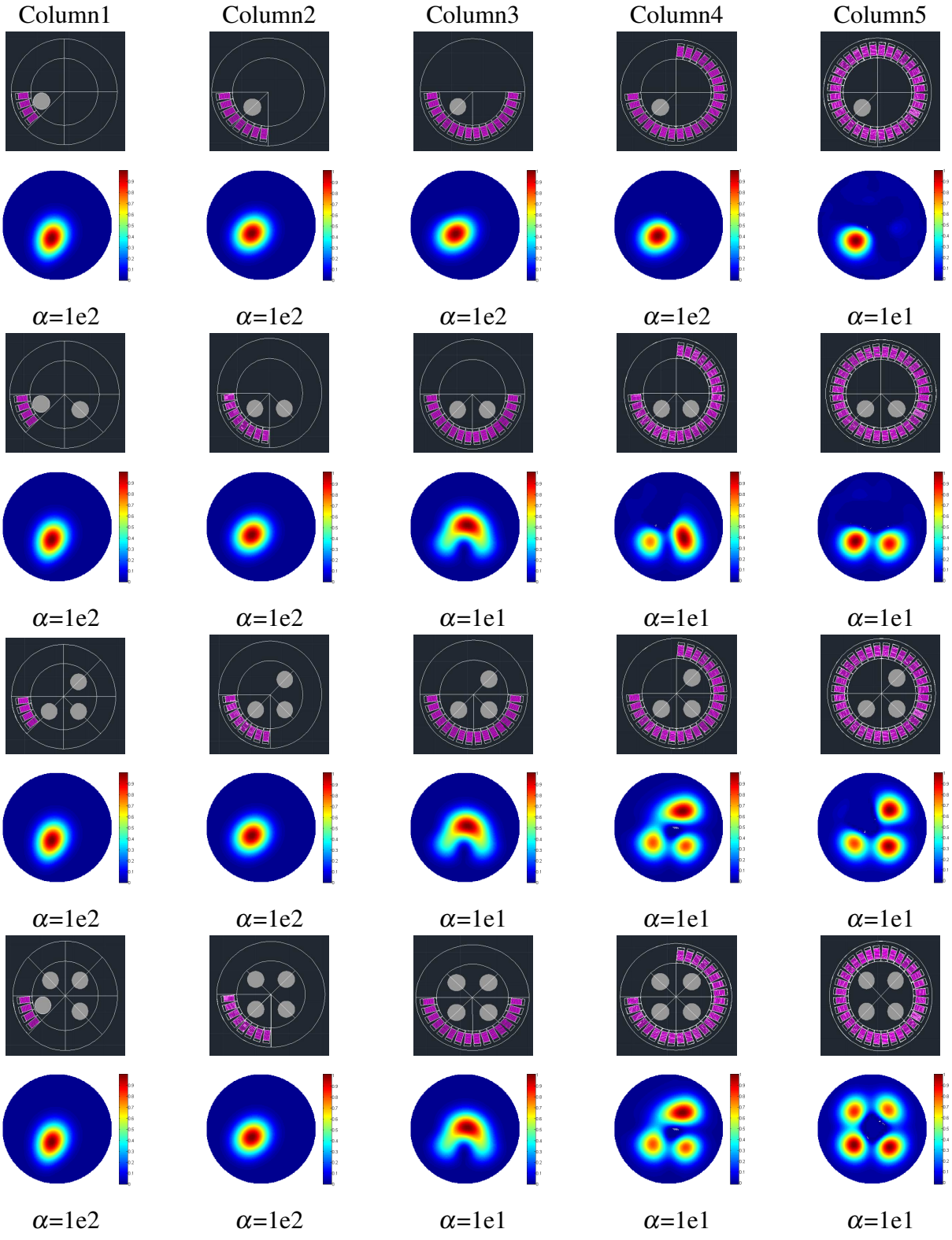

Figure 6.7: Single and multiple objects detection using limited angle imaging.

The singular value decay for limited angle imaging is shown in Figure 6.8. The system responses differently to each limited angle imaging, which means the system noise level varies accordingly. In here, the worst SNR scenario is considered to compare the number of singular values above the noise level. The number of singular values above the noise level decreases from 141 to 98, 60, 24 and 6 as the angle decreases from 360° to 270°, 180°, 90° and 45°, which causes the information loss.

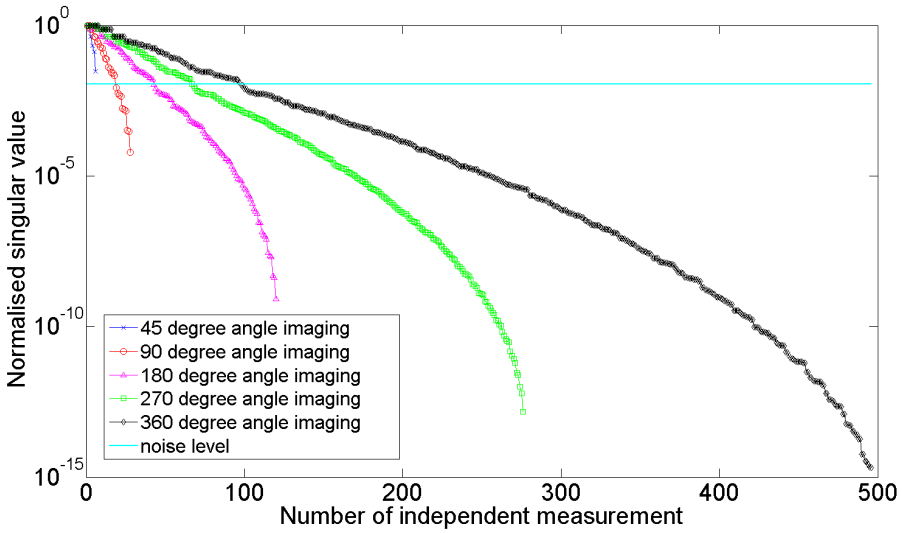

Figure 6.8: Singular value decay for limited angle imaging.

It is difficult to assess the image quality visually for the case of single object detection using different angles, as shown in the second row in Figure 6.7. Using image quality measure RES, we can assess the resolution loss due to missing data numerically. It can be seen from Table 6.5 that the RES value gradually decreases as the number of missing data increases. For limited angle imaging of 45° and 90°, only one object placed in the ROI is successfully detected. When there is more than one object under inspection, there is still only one object is shown in the reconstruction. Therefore, the RES values for multiple objects detection remain the same as the RES values for one object detection. This principle also applies to imaging three and four objects using limited angle of 180°, as well as imaging four objects using 270°. In these cases, the calculated RES values do not reflect the pixel amplitudes ratios anymore. Therefore, they are not shown in Table 6.5 to avoid confusion.

Angle	M'	RES one objects	RES two objects	RES three objects	RES four objects
360°	0	0.9677	0.9355	0.9077	0.8791
270°	220	0.9596	0.9332	0.8932	-
180°	376	0.9547	0.9278	-	-
90°	468	0.9543	-	-	-
45°	490	0.9543	-	-	-

Table 6.5: Image quality parameter with respect to different angles.

Figure 6.9 shows 1D graphs of conductivity distribution of the reconstruction of two rods from limited angle imaging. The values of conductivity intensity are normalised against the maximum value for each angle. It is shown in Figure 6.9 that 360°, 270° and 180° are capable of separating two objects placed in a row, while limited angle of 90° and 45° fail to do so. Comparing to the true case, 360° imaging provides the most accurate conductivity distribution of two inclusions. A good reconstruction is also produced using 270° imaging compared to 180° imaging. It is clear from the graph that limited angle of 90° and 45° can only map the conductivity distribution of one inclusion. This is consistent with the results presented in Figure 6.7.

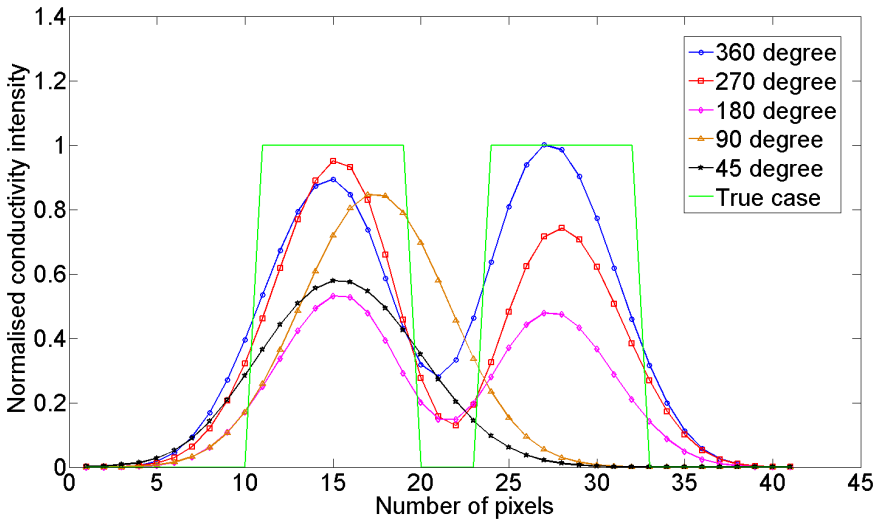

Figure 6.9: Graph of 1D conductivity distribution using limited angle imaging of 45°, 90°, 180°, 240° and full angle of 360°; referring to two objects detection in Figure 6.7.

6.4 A 3D Case Study

This section presents a 3D case study for the purpose of evaluating the missing data effect on the quality of MIT image reconstruction. A cube coil model is designed for this study, with each plane consisting of 5 coils. There are 30 coils in total. We systematically remove one plane of coils at a time to investigate the effect of missing data in limited access tomography. A variety of geometries can be established during the removal process. All geometries are assessed using experimental data. The effect of missing data is evaluated using singular value decomposition (SVD) and a matrix resolution analysis.

6.4.1 3D MIT Sensor

A cube MIT sensor model is developed for this case study (Figure 6.10). The sensor model consists of 6×5 sensors in total. The dimension of the cube model is $14 \times 14 \times 14$ cm^3. Each inductive coil has a radius of $2cm$, a side length of $3cm$, and 100 turns.

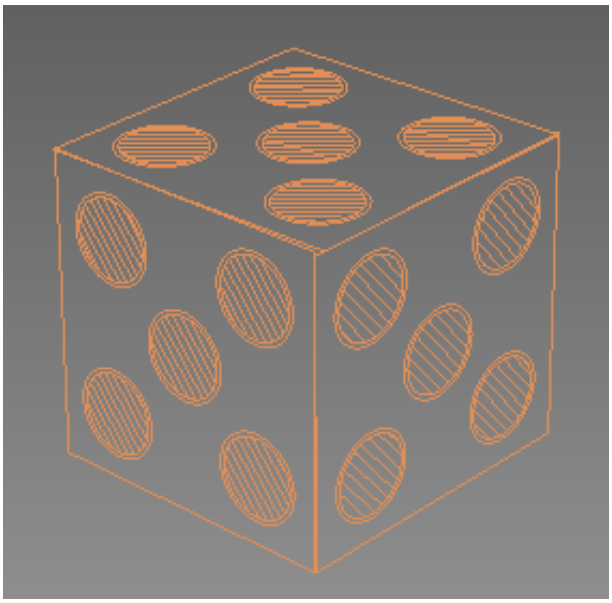

Figure 6.10: Schematic representation of a 3D cube sensor model.

6.4.2 Experimental Results

A steel cube sample is used for the following experiments. This cube has dimensions of $3.8 \times 3.8 \times 3.8\ cm^3$ and a conductivity of $3.5 \times 10^7 S/m$. The experimental procedure is carried out by removing a plane of coils to create a missing data effect which can be compared to the full data scenario. The removal process will result in different sensor geometries in different cases. In order to compare the reconstructed images in all cases, a cube sample is placed in the centre of the imaging region.

Five cases are established representing situations whereby there are zero, one, two, three, or four planes of coils removed from the cube model (cases 1 to 5, respectively). Figure 6.11 shows, by column, the geometry of the sensing array, a cross-sectional slice of a 3D reconstructed image of the metallic cube sample, and a reconstructed image in Mayavi visualisation.

The first row in Figure 6.11 shows the reconstructed images using a complete cube sensor geometry. In this case, an image of the metal cube is successfully reconstructed, shown as both a sliced image and a Mayavi visualisation. The second row shows the reconstructed image of a cube sample after one plane of coils is removed, leaving five planes of coils for imaging. Although compared to the full data case, removing one plane of coils results in 135 missing measurements, the reconstructed image quality does not seem to be compromised. Removing two planes of coils could lead to a variety of coil geometries, however, in this study, we only investigate the case whereby two parallel planes of coils are removed, as other geometries are neither common nor widely used. In this case, the location of the metal cube can still be accurately detected in the centre (third row in Figure 6.11). Nevertheless, there is a noticeable shifting of the reconstructed inclusion, i.e., the inclusion seems to be stretched towards the locations where two planes of coils are absent. A similar observation was also found in a 3D electrical capacitance tomography

study in a limited data scenario, described as a sphericity effect on a reconstructed image [179]. The fourth row in Figure 6.11 shows the reconstructed images using three planes of coils. The quality of the reconstructed images are noticeably degraded. In addition, there is also a strong sphericity effect of the inclusion in the reconstructed images. After removing four planes from the cube model, there are only two planes of coils for measurement acquisition, which again, can form a variety of sensor geometries. In this study, we only study the case whereby two planes of coils are facing opposite each other, i.e., as two parallel planes. The distance between two parallel planes is $14cm$ due to the dimension of the cube model. In an ideal case, an optimum distance can be chosen based on the SNR level of the system and the practical application one wishes to pursue [180]. The application of this parallel planar geometry is studied in chapter 4. The sphericity effect is further enhanced in this case, although the location of the inclusion can still be reliably imaged in the centre. The removal of five planes of coils from a cube model results in a planar array for testing. The study and application of this particular geometry is presented in chapter 5.

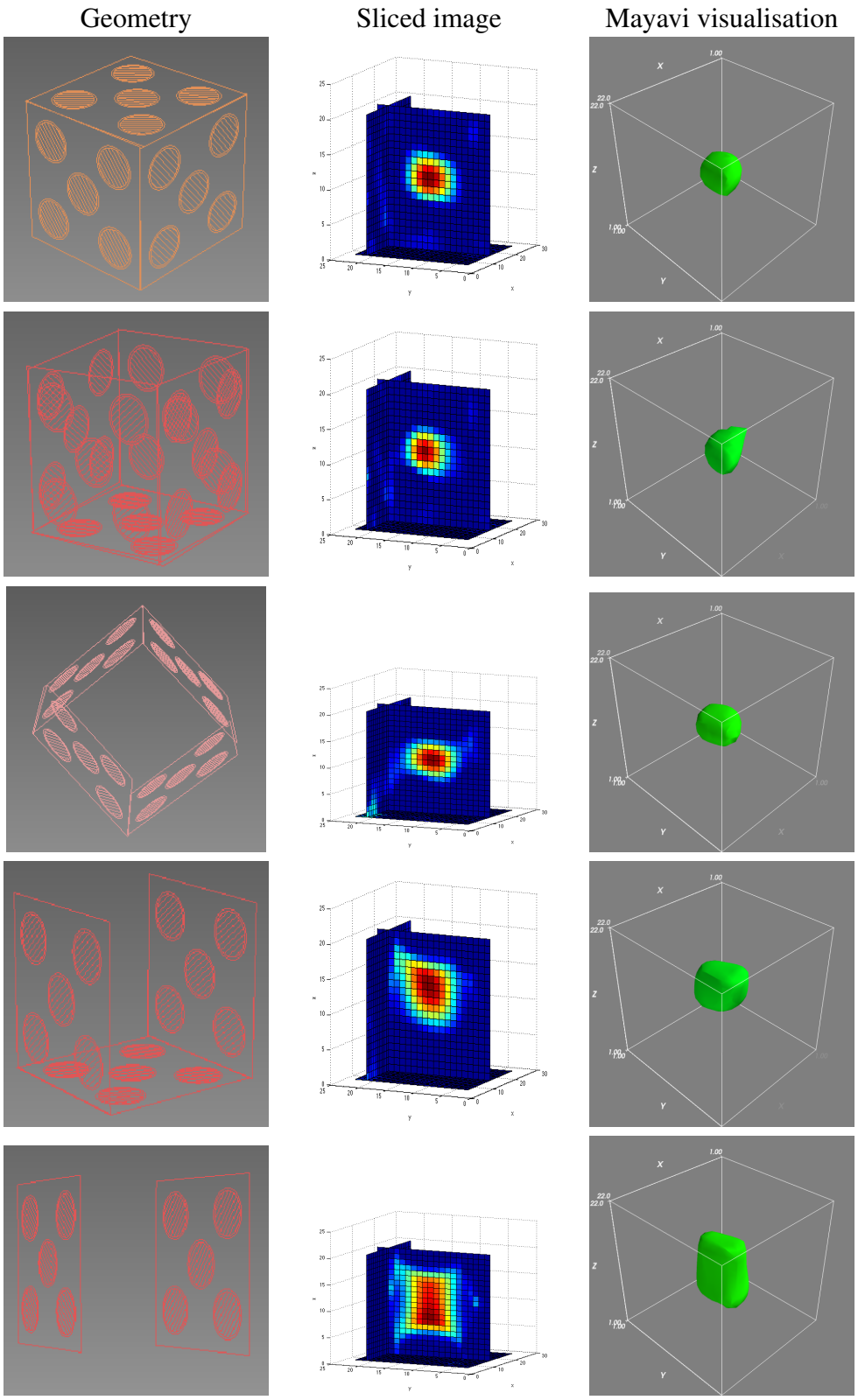

Figure 6.11: Reconstructed images of a metal cube under different missing plane scenarios. The number of missing planes, by row, is 0, 1, 2, 3, 4 respectively.

6.4.3 Evaluation of the Missing Planes

Figure 6.12 shows the sensitivity contours between pairs of coils in Mayavi visualisation. From left to right: the sensitivity contour for a central coil in the bottom plane and a

central coil in the plane perpendicular to the bottom plane, two central coils opposite to each other, and a diagonal pair of coils located in the same plane.

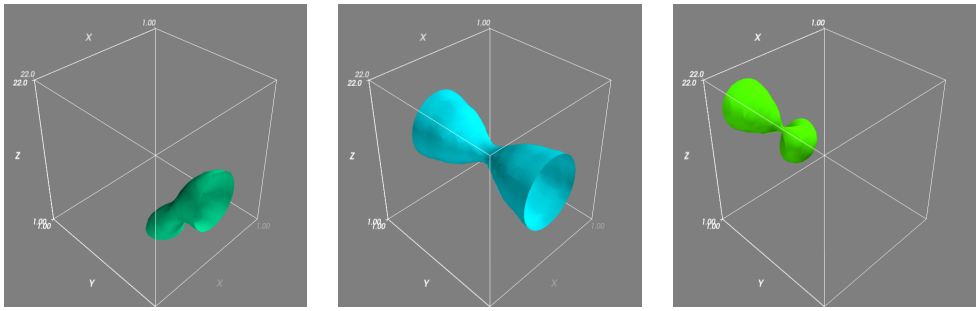

Figure 6.12: Sensitivity maps.

The singular value decomposition (SVD) is also adopted for analysis. The concept of SVD has been introduced in the previous section. Figure 6.13 shows the decay of SVD for Jacobian matrices under different missing plane cases (listed in Figure 6.11).

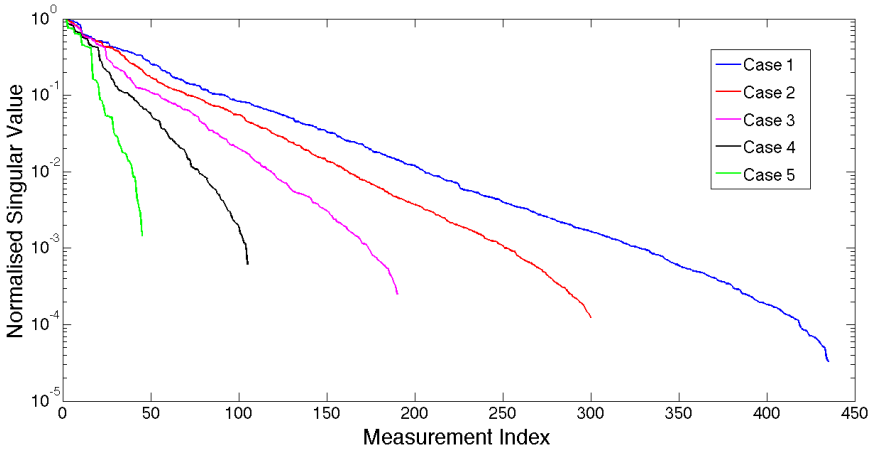

Figure 6.13: Decay of the normalised singular value of sensitivity matrices for five cases: case 1-full data scenario, case 2-five planes, case 3-four planes, case 4-three planes, case 5-two parallel planes.

The aim of the inverse problem is to solve the distribution of passive electromagnetic properties of the imaging subject. Recall the Tikhonov regularisation formulation 2.48:

$$x = (J^T J + \alpha I)^{-1} J^T b \tag{6.2}$$

The true distribution of b can be written as:

$$b_{true} = J x_{true} \tag{6.3}$$

A model distribution of the conductivity is therefore:

$$x_{model} = (J^T J + \alpha I)^{-1} J^T J x_{true} \tag{6.4}$$

A resolution matrix is defined by:

$$R_m = (J^T J + \alpha I)^{-1} J^T J \tag{6.5}$$

This suggests that the closer the resolution matrix is to the identity matrix, the more stable and reliable the inverse model is [181]. The resolution matrix is a column vector, and the sum of the diagonal component of the resolution matrix reflects how close the value is to that of an identity matrix. Figure 6.14 show the sum of the diagonal components of the resolution matrix for five cases. The value decreases as the number of missing planes increases. This is expected, and also consistent with the observations found in the previously discussed 2D MIT study.

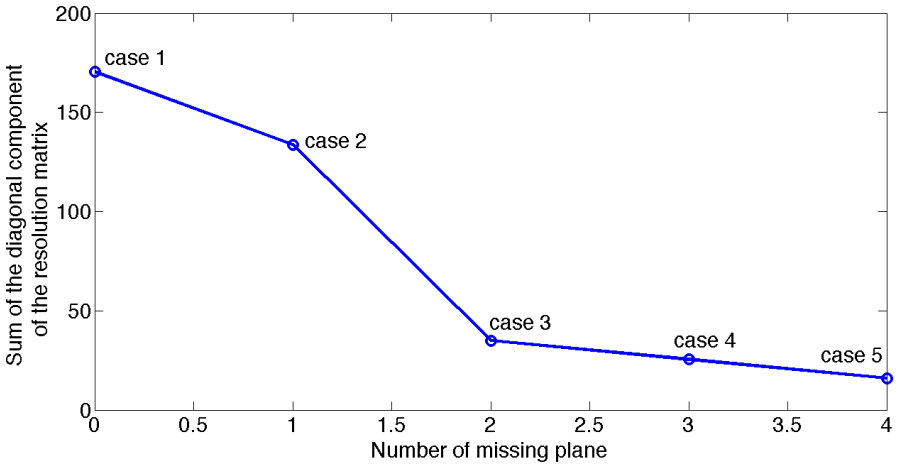

Figure 6.14: Sum of the diagonal components of the resolution matrix at five missing plane cases.

6.5 Discussion

This chapter evaluates the effect of missing data through undersampling measurements and limited angle imaging using experimental data. This is carried out in a systematic manner and the images are assessed using an image quality measure RES and graphs of 1D plots. It is important to distinguish this study from the optimisation of the number of sensors in MIT. Here we choose a 32-channel MIT system, which produces acceptable quality images, and systematically remove coil sensors to study the effect of missing data through undersampling and limited angle tomography. The quality of reconstructed images are assessed to indicate the resolution loss caused by missing data in MIT. It is worth noticing that the proposed MIT system uses a sequential data collection strategy. In this context, the data acquisition in undersampled cases becomes faster but results in lower image quality. The limited angle could happen when there is only limited access to the imaging subject. The results of this study illustrate what to expect from limited angle situations and highlight the challenges related to this. The future direction of this study

is to develop a compressed sampling technique to undersample MIT data, in particular with a very large number of coils (for example, 256 coils [182]). A large number of coils can result in a large number of measurements, which could pose great difficulty to system hardware by slowing the data acquisition and image reconstruction processes significantly. Unlike the systematic removal of coils in the 32-channel system presented here, we aim to find an optimal trade-off between the image quality and data acquisition time. This study provides a fundamental background for such work.

The 3D case study further investigates the effect of missing data on the quality of reconstructed images in a volumetric scenario. It is expected that removing planes of coils results in image quality degradation. This is validated by analysing the singular value decomposition and resolution matrix, and is consistent with our findings in a 2D case. Furthermore, among the missing plane cases, the parallel plane and single plane geometries have direct appeal in practical applications, as shown in chapters 4 and 5.

Chapter 7

Experimental Evaluation of Two-phase Flow Imaging

Multi-phase flow imaging is a challenging topic in industrial process tomography. In this chapter, we present a non-invasive imaging technique for the electrically conductive phase of a multi-phase flow problem. Magnetic induction tomography (MIT) is sensitive to the conductivity of the target, and as such has the potential to be used as an imaging technique to visualise the conductive components in a multi-phase flow application. The MK-II MIT system is used for this study, among which eight excitation coils are supplied with a $15V$ peak, $13MHz$ sinusoidal signal in sequence from a signal generator, while the remaining eight coils are floated as receivers. The imaging region of this MIT system has an inner and outer diameter of $190mm$ and $200mm$ respectively. Static fluid distribution patterns are produced using several fluids with different conductivities and placed inside the imaging region to form conductivity phase contrasts. Experimental results show that the smallest conductivity contrast that can be imaged is $0.06S/m$ for an inclusion that occupies 8.69% of the imaging region. An in-depth experimental evaluation of the system response towards various fluid measurements is shown for the first time, as are results for quasi-static fluid experiments showing that a non-homogenous flow of gas bubbles can be imaged in various conductive backgrounds. In sum, the analyses presented investigate the feasibility and capability of MIT for this application, while also reporting some of the first flow rig tests in this field.

7.1 Introduction

Magnetic Induction Tomography (MIT) is also known as electromagnetic induction tomography or eddy current tomography. It is a relatively low cost technique, although due to its soft-field nature, the resolution of MIT has not yet met the standards for widespread commericalisation. The underlying principles of MIT is that a magnetic field is excited and registered by inductive coils arranged around the imaging region; the spatial distribution of magnetic field and the mutual coupling between the coils is then altered by material

presented in the imaging region. Materials can be either ferromagnetic or conductive. In a typical 2D phantom study case, the cross-sectional images of the properties of the object can be reconstructed using the voltage or phase measurements collected from the inductive coils. Because of the non-hazardous, non-invasive and contactless natures of MIT, its use has been proposed for numerous applications, including geological exploration [3], foreign material monitoring [183], non-destructive evaluations [153, 167, 177], and biomedical imaging [13, 90, 178, 184, 185, 186, 187, 188, 189, 190].

It is also considered more advantageous to use MIT in flow imaging compared to electrical resistance tomography techniques [191, 192, 193]. Due to the low resolution of this technique, the realisation of MIT as a smart imaging device for industrial process tomography remains a challenging topic. There have been reported cases where MIT is used for metal visualisation and solidification [18, 19, 194]; however, the experimental validation in two-phase or multi-phase flow imaging using MIT is still limited. It is considered that MIT could be complementary to existing techniques for multi-phase flow imaging as MIT is sensitive to the conductive component of the flow mixtures [195, 196]. A feasibility study of electromagnetic imaging in distinguishing two type of conductivities: fat and water-bearing fat free tissues was presented in 1993. This study was primarily focused on the imaging of biomedical tissue, however, the concept of MIT be used in flow process was introduced and validated for the first time [60]. Albrechtsen et al [197] proposed a single channel MIT system to measure the water content in multi-phase flow using experimental phantom recordings. Based on the observations, the authors concluded the correlation between the position of the coil and the water/oil interface could be overcome by a full tomographic system. Similar conclusions have also been drawn by Hammer et al [198]. Liu et al [199] proposed a parallel excitation structure for MIT in an attempt to image conductive or ferromagnetic properties in two phase flow. However, this work was limited in scope, focussing a simulation of the sensing field, and as such experimental results were not included in the publication. It was not until 2008 that a full MIT system had demonstrable feasibility for two phase flow imaging. Watson et al [200] studied a phantom simulated multi-phase flow in an oil pipeline, with the imaging conductivity of the system found to be below $10S/m$. More recently, Wei et al [201] demonstrated an experimental based two phase flow imaging using a 16 channel MIT system. Nevertheless the experimental results were promising, showing that a conductivity contrast as small as $1.58S/m$ can be imaged, the authors did not pursue further analysis of the results.

This chapter presents a critical evaluation of MIT for two phase flow imaging. Both static and quasi-static experiments are presented to evaluate the MIT in variety of conditions. The practical difficulties, fundamental limitation, and potential improvement of this technique are discussed.

7.2 Static Fluid Test Results

7.2.1 Experimental Setup

The MK-II MIT system is used for this study, which consists of 16 coils arranged around the imaging periphery. The inner diameter, outer diameter and the length of the imaging region are 190mm, 200mm and 90mm respectively. The driving frequency is 13MHz, with a 15V peak driving voltage and a driving current of 0.39A. The coil resonance frequency is 45MHz, and the sampling rate of the system is 100MS/s [83].

A series of systematic experiments are conducted to demonstrate the likely conditions of an industrial process environment using static fluid distribution patterns. Several terms are used throughout this study, hence it is worth giving the description for each term.

- Imaging region: the region of interest where the static fluid distribution pattern is measured using 16 inductive coils on the periphery.
- Background conductivity: the conductivity of the contents of the imaging region, excluding any inclusions.
- Inclusion: an area of differential conductivity within the imaging region, as compared to the background conductivity. As this study utilises fluids, the background material and the inclusion(s) of interest can both be fluid distribution patterns. In this case, the inclusion is kept distinct from the background by being bottled in a non-conductive object.
- Conductivity contrast: the difference between the conductivity of the background and the inclusion.
- Area ratio: ratio of the cross-sectional area of the inclusion to the area of the total imaging region.
- Norm value of phase difference: the norm value of the phase shift measurement between the background and the inclusion (millidegrees), and it is calculated directly from the raw measurements with no calibration. As a difference imaging is used in this study, the norm value presents the phase shifts in a single value.

Two scenarios are considered to demonstrate the conductivity contrasts in the imaging region, i.e., conductive inclusion(s) in a non-conductive background and non-conductive inclusion(s) in a conductive background. A static fluid distribution pattern is introduced to the background by bottling the fluid in a non-conductive cylindrical container. In each scenario, the inclusion is measured in three dimensions (28.70mm, 56.00mm and 72.52mm, hereafter small, medium and large respectively). As the fluid is bottled in a closed area in the imaging region, it is feasible to calculate the ratio of the cross-sectional area of the

inclusion to the total imaging region (i.e., area ratio). The area ratios of a single inclusion in the imaging region for small, medium and large dimensions are 2.28%, 8.69% and 14.57% respectively. For each experiment, both single and multiple inclusions of the same size are tested. In the case of a single inclusion, the experiment is conducted in three different positions to assess the spatial homogeneity of the system response (marked as pos1, pos2 and pos3 in Figure 7.1). Similarly, when two inclusions are tested in the imaging region, pos1 and pos2 are selected as a representative example; when three inclusions are tested, all three positions are used (Figure 7.1). In total, over 600 sets of experiments are conducted to evaluate the MIT system for imaging two phase distributions of static fluid in the imaging region. The aim of the static fluid distribution tests is to identify the smallest conductivity contrast that can be reconstructed and the area ratio for that contrast.

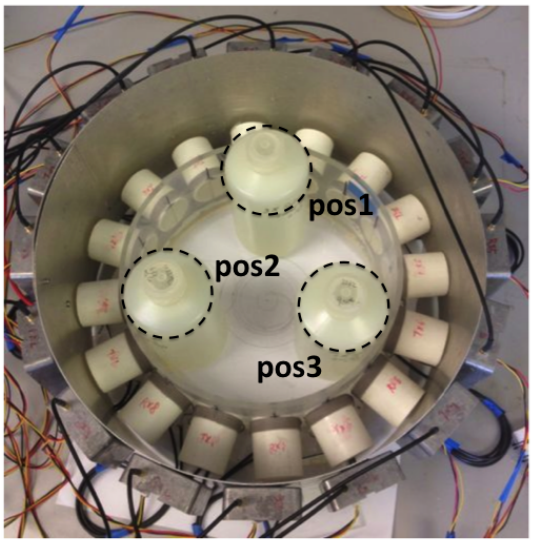

Figure 7.1: The experimental setup, in this case showing three inclusions within the imaging region.

7.2.2 Fluid Distribution Patterns in a Free Space Background

Three saline solutions with different conductivity values are used, of $1.52S/m$, $4.06S/m$ and $5.94S/m$ (low, medium and high) respectively. Each solution is bottled in the aforementioned non-conductive containers (small, medium and large). These containers are placed within the imaging region in each experiment as the only inclusion.

Figure 7.2 shows the standard deviation of the norm values of the phase difference resulting from the position change (i.e., whether the single inclusion is at pos1, pos2 or pos3) versus the area ratio for fluids of three conductivity levels (red, blue and magenta for, respectively, low, medium and high conductivity). For each conductivity level, standard deviations are calculated from data independently obtained at all three positions (pos1, pos2 and pos3). Three standard deviations are calculated in total, one per area ratio (small, medium and large).

We can draw two conclusions from this figure. Firstly, the standard deviations reflect

both the stability and repeatability of the data obtained for a given conductivity level, with lower standard deviations associated with more stable and more highly repeatable data. Secondly, the standard deviations of the three conductivity levels are highly variable depending on area ratio. Standard deviations for all three conductivity levels are similar for small and medium area ratios, and highly divergent for large area ratios, suggesting that in the latter case different conductivity levels are more readily distinguished.

Furthermore, the difference in standard deviations between the three area ratios reflects their distinguishability from each other - for instance, small inclusions (i.e., with small area ratio) have not only comparatively high standard deviations but their standard deviations at each conductivity level are relatively similar. As such, small inclusions have the most unstable measurements and accordingly are more difficult to distinguish by conductivity. For medium inclusions, the standard deviation for all three conductivity levels is far lower than that of either small or large inclusions, reflecting that they have both the highest stability of all the measurement data but also that they are the most difficult to distinguish by conductivity. In addition, the standard deviation of the norm value for a large inclusion of the highest conductivity is the greatest among all other cases, suggesting that although this represents a poorly-repeatable measurement, it unambiguously distinguishes high conductivity from medium or low. Thus, there is a trade-off between the stability of the system and its ability to distinguish inclusions by their conductivity.

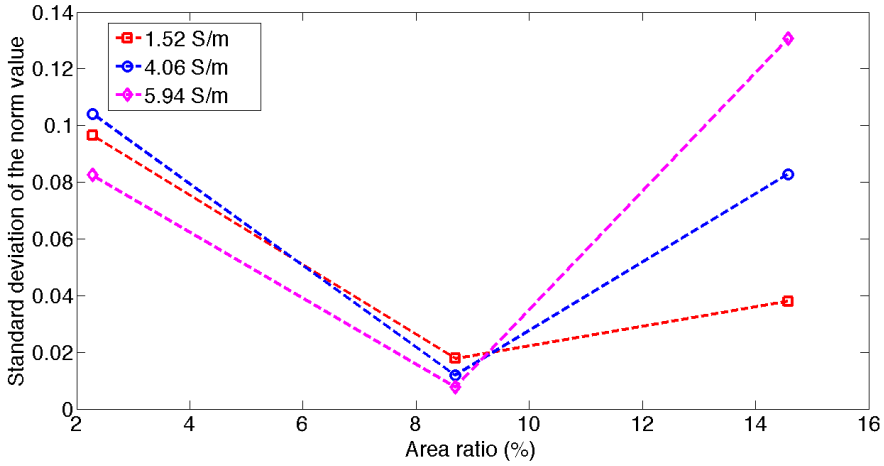

Figure 7.2: Standard deviation of the norm value of the phase difference resulting from the position change of a single inclusion versus the area ratio of that inclusion (2.28%, 8.69% and 14.57% respectively). Data is shown for fluids with three conductivities (red, blue and magenta for, respectively, conductivity values of $1.52 S/m$, $4.06 S/m$ and $5.94 S/m$).

Figure 7.3 shows the reconstructed images for, by row, one, two and three inclusions of, by column, small, medium and large area ratios. In all cases, the conductivity of the inclusion(s) is $1.52 S/m$. It can be seen that for small inclusions, conductivity contrasts cannot be reliably reconstructed regardless of the position of the inclusion or the number of inclusions in the imaging region (first row in Figure 7.3). For both medium and large inclusion, images of one, two or three inclusions can be reliably reconstructed. This

suggests that in this scenario, for a given conductivity contrast, if the inclusion cannot be imaged, increasing the number of inclusions does not contribute to any significant gain in information. However, by increasing the dimension of the inclusion, this could result in an improved resolution in the reconstructed image. This suggests that in this case, the dimension of the inclusion is more informative with regard to image reconstruction than the number of inclusions being imaged. This phenomenon can be explained by reference to the sensitivity distribution of the MIT system: areas nearer sensors are comparatively more sensitive than regions farther away [40]. Furthermore, although the area ratio covered by a small inclusion is, by definition, less than that of a medium or large inclusion, and increasing the number of inclusions further introduces a field perturbation into the imaging region, small inclusions still cover a less sensitive area compared to medium of large counterparts, resulting in unsuccessful image reconstruction.

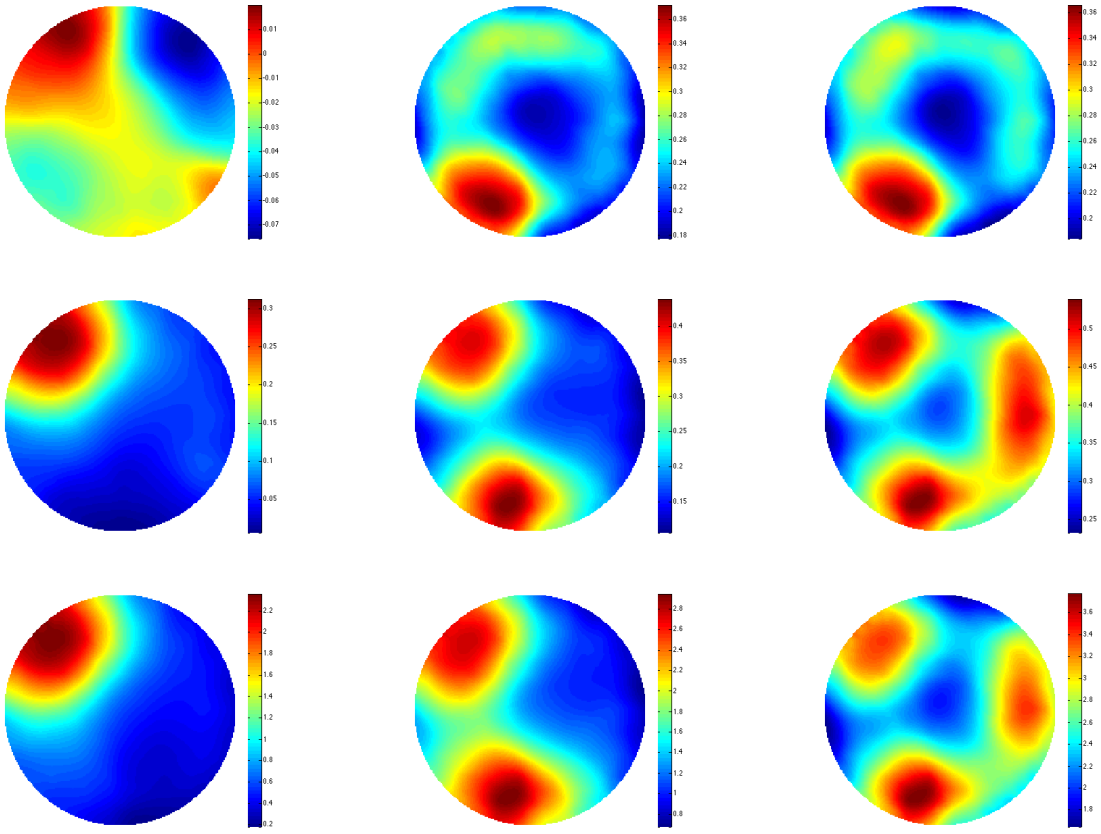

Figure 7.3: Reconstructed images of one, two and three inclusions in a free space background are shown in the first, second and third column; the first, second and third row shows the reconstructed images of small, medium and large dimensions of inclusions in a free space background respectively. The conductivity of the inclusion is $1.52S/m$ in all cases.

In this section, the aim of the experiments is to investigate whether for the same number of inclusions, of the same dimension and at the same testing positions, the conductivity of the inclusion affects its detectability. The first row in Figure 7.4 shows the reconstructed images for a single inclusion in the same testing position for conductivities of $1.52S/m$, $4.06S/m$ and $5.94S/m$ (low, medium and high) respectively. Each column refers to a dif-

ferent inclusion size (small, medium or large). It can be seen that for a single, individual inclusion, an image cannot be reconstructed for at low or medium conductivities and that at high conductivity, the reconstructed image contains multiple, notable artifacts. For two or three inclusions, at all three levels of conductivity, the image reconstructions are successful. By comparing the reconstructed images of multiple medium and multiple large inclusions, we observe more uniform colouration (i.e., similar values) amongst medium-sized compared to large inclusions. This is consistent with the observations shown in Figure 7.2 which suggest that for all three levels of conductivity, medium-sized inclusions are optimal in terms of the stability of their measurements.

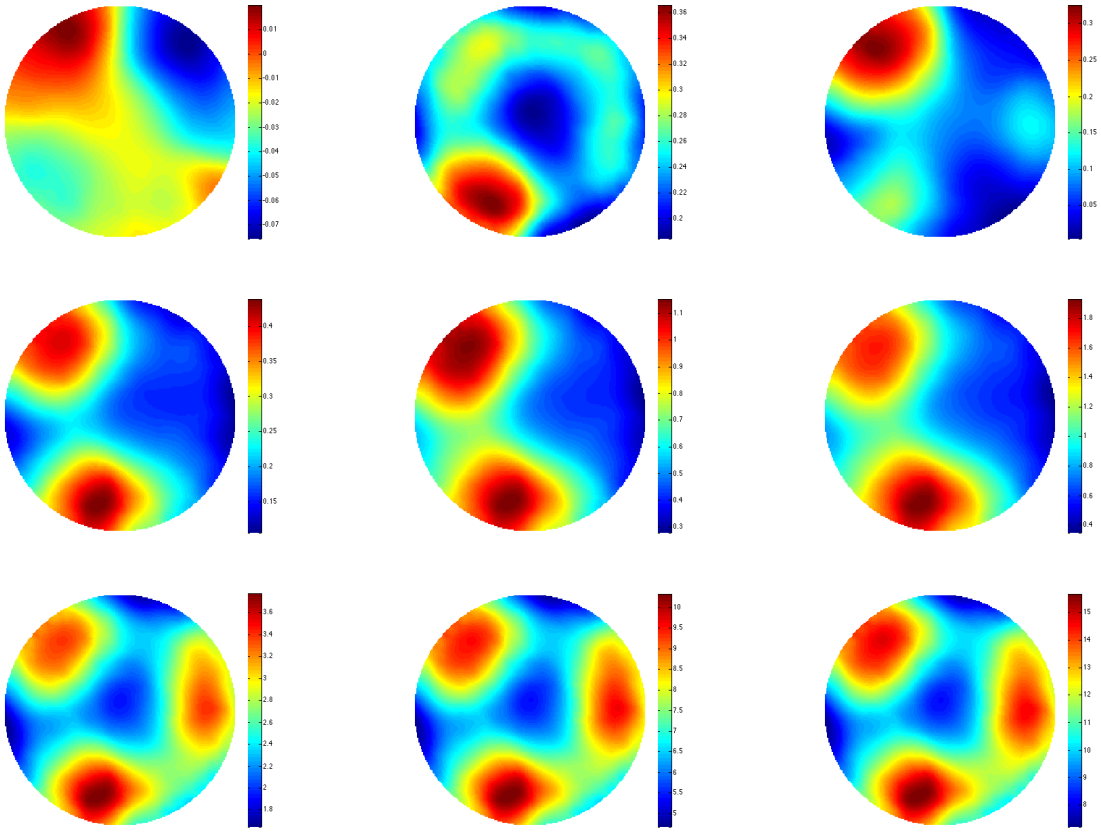

Figure 7.4: Reconstructed images of small, medium and large dimensions of inclusions in a free space background are shown in the first, second and third column; the first, second and third row shows the reconstructed images of one, two and three inclusions in a free space background respectively. The conductivities of the inclusions in the first, second and third columns are $1.52S/m$, $4.06S/m$ and $5.94S/m$ respectively.

Figure 7.5 contains two sets of plots, showing the norm value of the phase difference against either the change in area ratio (left, in black) or the change in conductivity level (right, in brown). Both sets of plots are produced using one, two or three inclusions (top to bottom, respectively). The norm value of the phase difference against the change in area ratio behaves similarly in all cases: there is a low variance for the size change from small to medium, increasing substantially when the dimensions change from medium to large. This is consistent with the results shown in Figures 7.2 and 7.3. By contrast, for

medium and large inclusions, there is a linear correlation between conductivity level and the norm value of the phase difference. For small dimension, the plots for one, two and three inclusion(s) are inconsistent with each other due to the low stability of the data, as also shown in Figure 7.2. This also explains the unsuccessful image reconstruction shown in the top row of Figure 7.3.

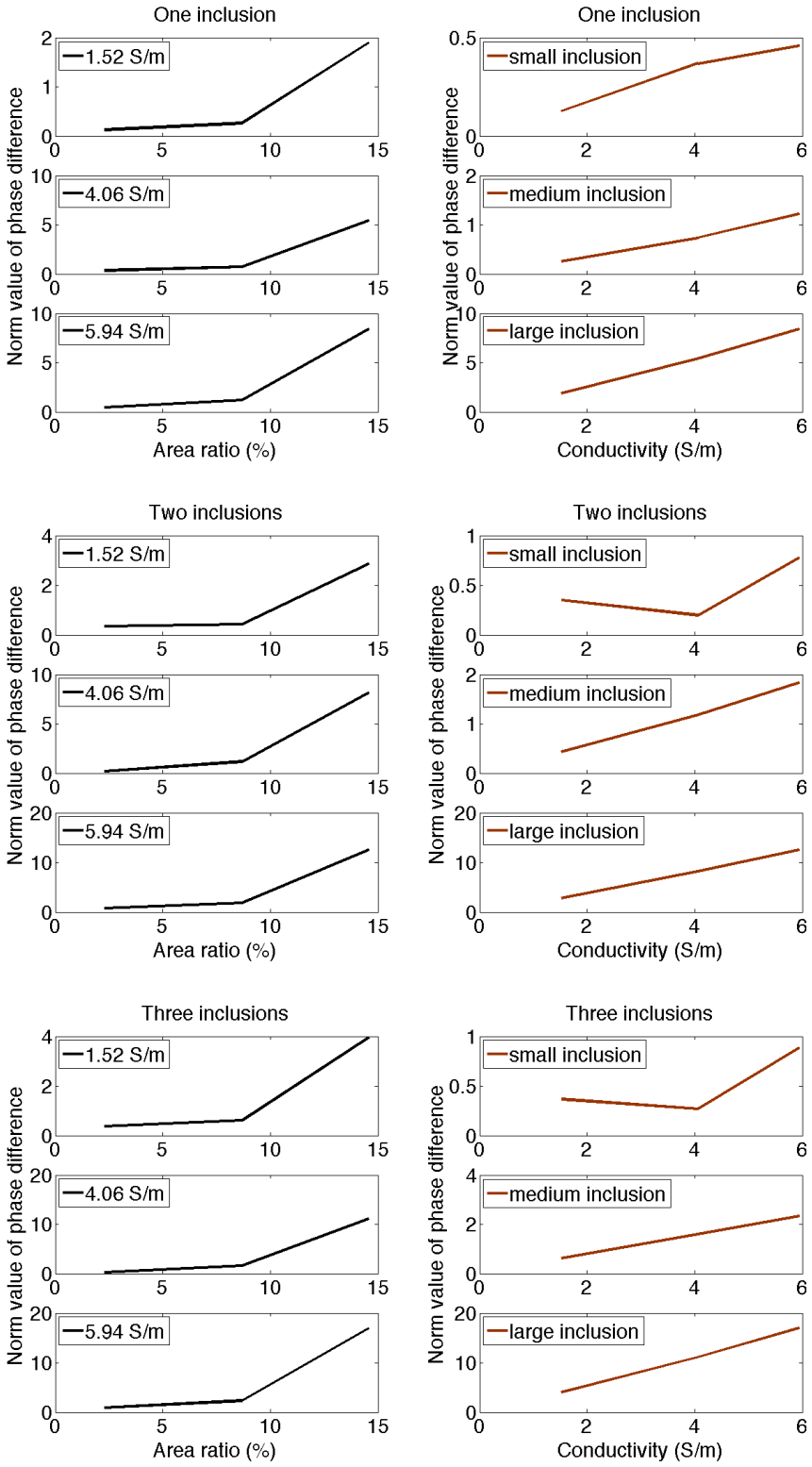

Figure 7.5: The norm value of the phase difference against the change in area ratio (left, in black) and the change in conductivity level (right, in brown). Both sets of plots are produced using one, two or three inclusions (top to bottom, respectively).

7.2.3 Fluid Distribution Patterns in a Silicone Oil Background

The silicone oil used in this study has an electrical insulation property, and as such can be used as a non-conductive background. Figure 7.6 shows the reconstructed images of one to three inclusions of a $1.52S/m$ saline solution in a silicone oil background (columns left to right, respectively), of either small, medium or large dimensions (first, second and third rows, respectively). We show that the image quality increases as the dimension of the inclusion increases, and that furthermore the ability to distinguish the location of multiple inclusions become more pronounced as their dimensions increase.

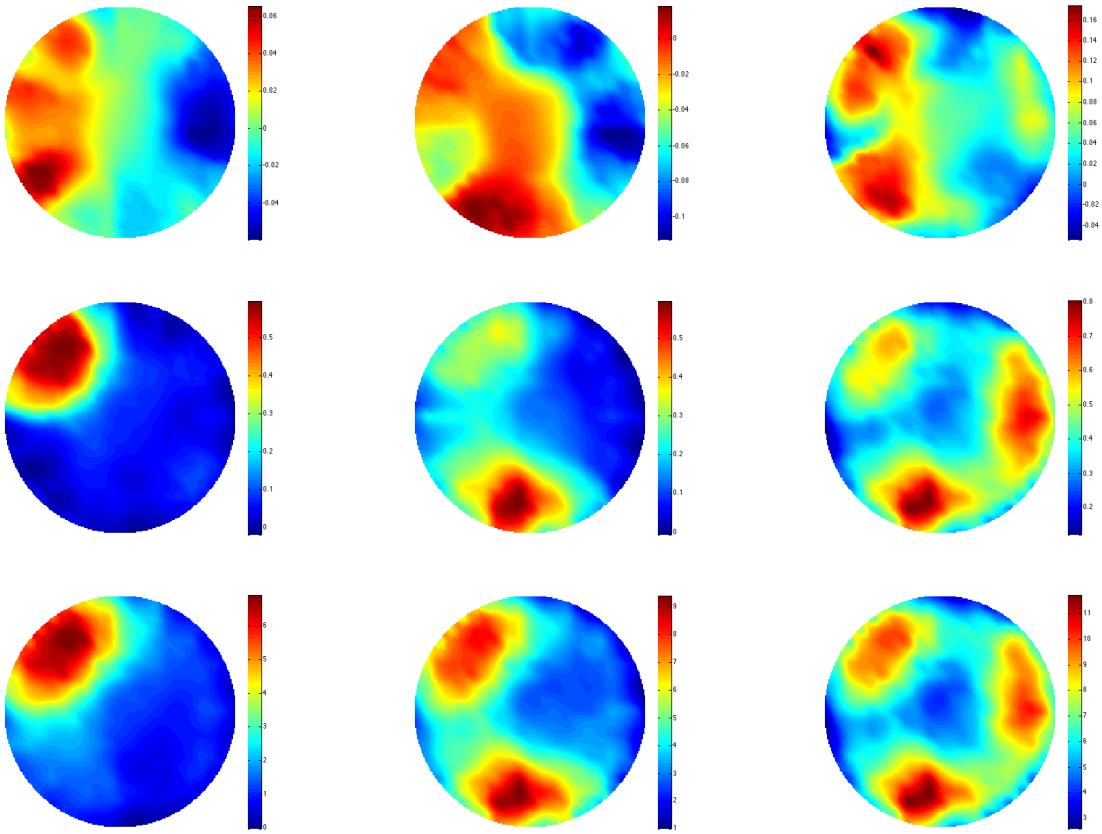

Figure 7.6: Reconstructed images of one, two and three inclusions of saline solution in a free space background are shown in the first, second and third column; the first, second and third row shows the reconstructed images of small, medium and large dimensions of saline solution in a free space background respectively. The conductivity of the saline solution is $1.52S/m$ in all cases.

7.2.4 Fluid Distribution Patterns in a Saline Solution Background

In this section, two phase liquid imaging is investigated using silicone oil to represent a non-conductive inclusion and saline solution (conductivity $1.52S/m$) as a conductive background. Figure 7.7 shows the reconstructed images of three sizes of inclusions - small, medium and large, as shown in the first, second and third rows, respectively. Although the conductivity contrast is the same as presented in Figure 7.6, the reconstructed images notably differ. For instance, it appears that the dimension of the inclusion carries

comparatively little informative weight with regard to the quality of the image - this is in contrast to Figure 7.6, whereby increases in inclusion size from small to medium can noticeably isolate the area of interest.

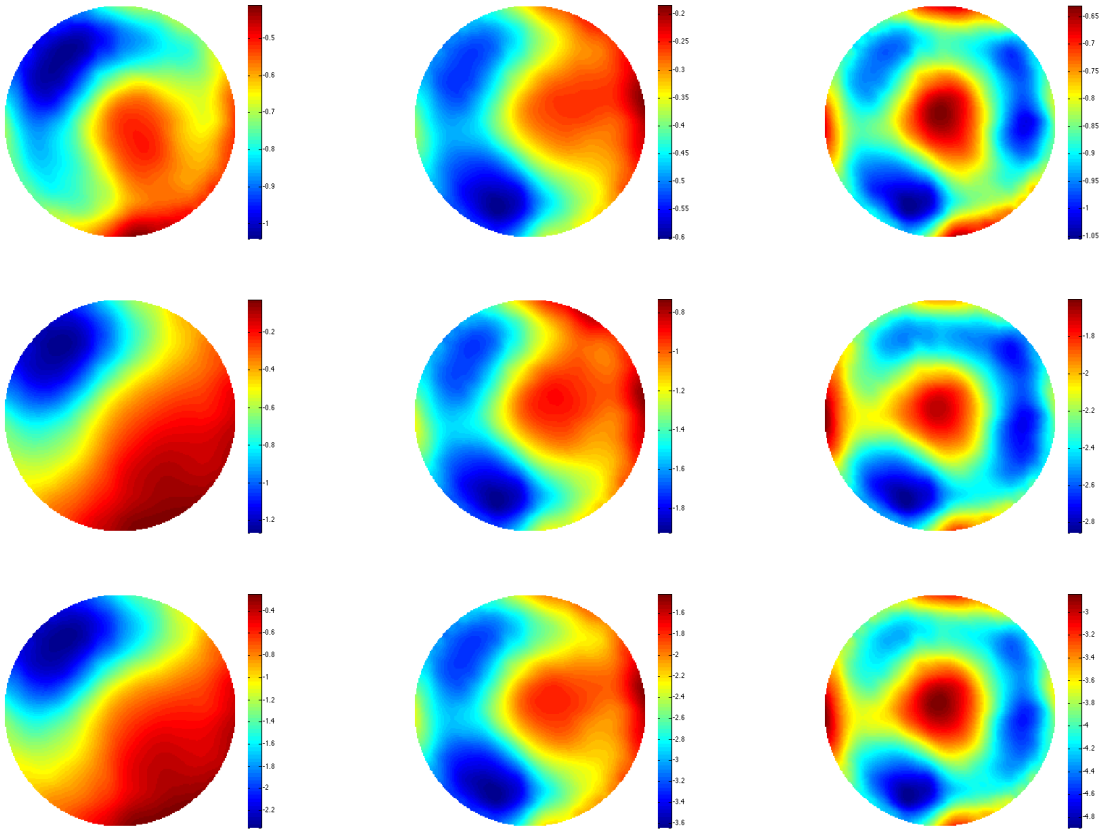

Figure 7.7: Reconstructed images of one, two and three inclusions of silicone oil in a saline solution background are shown in the first, second and third column; the first, second and third row shows the reconstructed images of small, medium and large dimensions of silicone oil in a saline solution background respectively. The conductivity of the saline solution background is $1.52S/m$.

Figure 7.8 shows the standard deviation of the norm value of the phase difference resulting from position change for conductive inclusions in a non-conductive background (saline solution with $1.52S/m$ conductivity in a silicone oil background; dashed blue line) and non-conductive inclusions in a conductive background (silicone oil in saline; dashed red line). Unlike Figure 7.2, the effect of inclusion size differs in both cases. This suggests that the MIT imaging system shows a different response to different backgrounds. It can be seen that the standard deviation of the norm value increases more sharply for larger area ratios in the case of conductive inclusions in a non-conductive background, compared to a more steady increase for non-conductive inclusions in a conductive background. This supports the previous suggestion that inclusion dimension carries greater informative weight for the image reconstruction of conductive inclusions against a non-conductive background. This would also explain the substantial improvement in image quality as the inclusion dimension increases in Figure 7.6, compared to Figure 7.7, where

the improvement in resolution is less discernible.

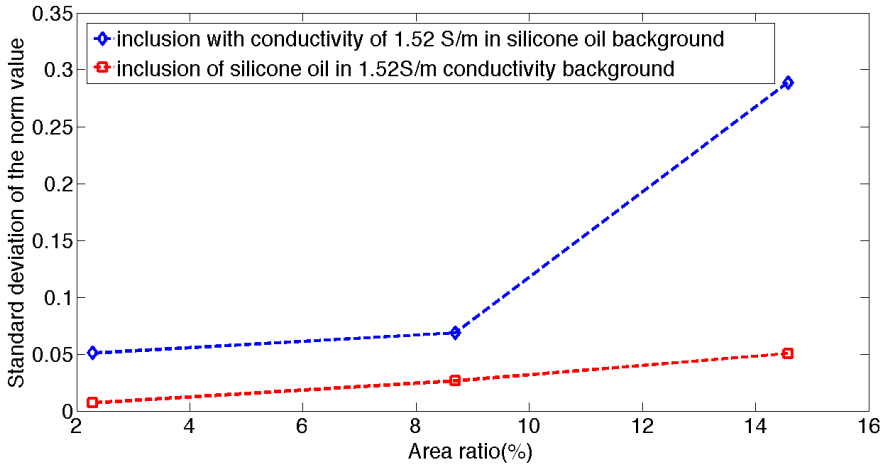

Figure 7.8: Standard deviation of the norm value of the phase difference resulting from the position change of a single inclusion versus the area ratio of this inclusion (2.28%, 8.69% and 14.57% respectively) for two cases: silicone oil in a saline background (dashed red line), and saline solution (conductivity $1.52 S/m$) in a silicone oil background (dashed blue line).

7.2.5 Fluid Distribution Patterns in a Tap Water Background

Compared to the other conductive fluids previously discussed, tap water is not only more common but has comparatively low conductivity. As such, we repeated the above experiment using tap water as a background and silicone oil as an inclusion, in order to determine the smallest conductivity contrast at which image reconstruction is still feasible. Figure 7.9 shows the reconstructed images of one, two and three inclusion(s) of silicone oil in a tap water background. Although image quality is poor in comparison to previous results, this is nevertheless an encouraging finding, as it suggests the smallest conductivity contrast at which image reconstruction is possible is $0.06 S/m$, for an inclusion that occupies 8.69% of the total imaging region.

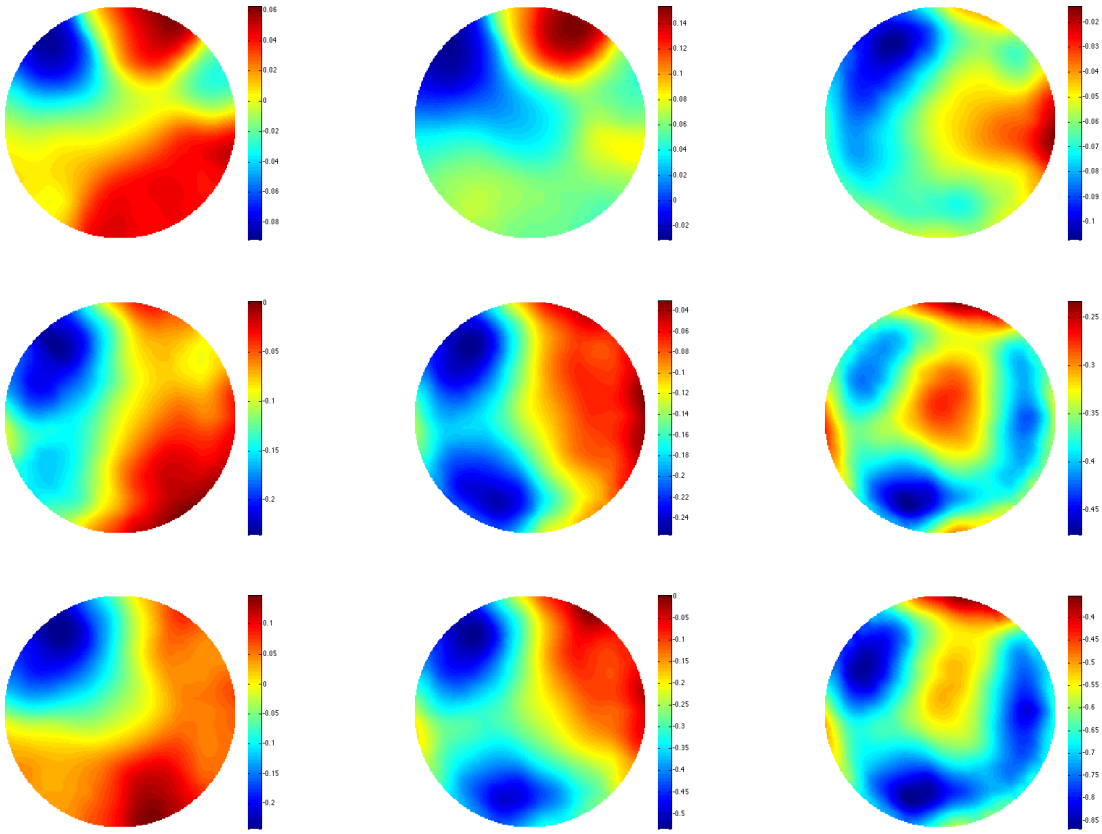

Figure 7.9: Reconstructed images of one, two and three inclusions of silicone oil in a tap water background are shown in the first, second and third column; the first, second and third row shows the reconstructed images of small, medium and large dimensions of silicone oil in a tap water background respectively. The conductivity of the tap water background is $0.06S/m$.

7.2.6 Non-homogenous Conductive Fluid Imaging in a Free Space Background

A stratified flow regime is one of the classic flow regimes in industrial process tomography. A core aspect of this regime is the differentiation of multiple liquid flows, of variable conductivity, into strata. Our experimental setup does not allow the direct testing of flow, although it is nevertheless of interest to determine whether strata can be distinguished for non-homogenous, albeit in this case static, liquids. The aim of this experiment is to image different volumes of conductive fluid within the imaging region to determine whether they can be distinguished by strata. In this experiment, a conductive fluid is used with a conductivity of $6.20S/m$. This fluid is bottled in plastic containers with outer diameter of $37mm$ and a height of $79mm$. Each container is fully filled with $50ml$ fluid. Strata are created within the imaging region by aligning multiple containers as shown in Figure 7.10 (marked by dashed lines). As the conductivity and volume of fluid in each bottle is constant, varying the number of bottles allowed us to vary the total volume of conductive fluid in each stratum. As the bottles are surrounded by free space, each strata is a non-

homogenous mix of both conductive and non-conductive material. Three strata are tested, varying by total volume of conductive fluid (4, 8, and 13 containers, i.e., 200*ml*, 400*ml* and 650*ml*, respectively). Reconstructed images shown from the left to the right in the bottom row of Figure 7.10.

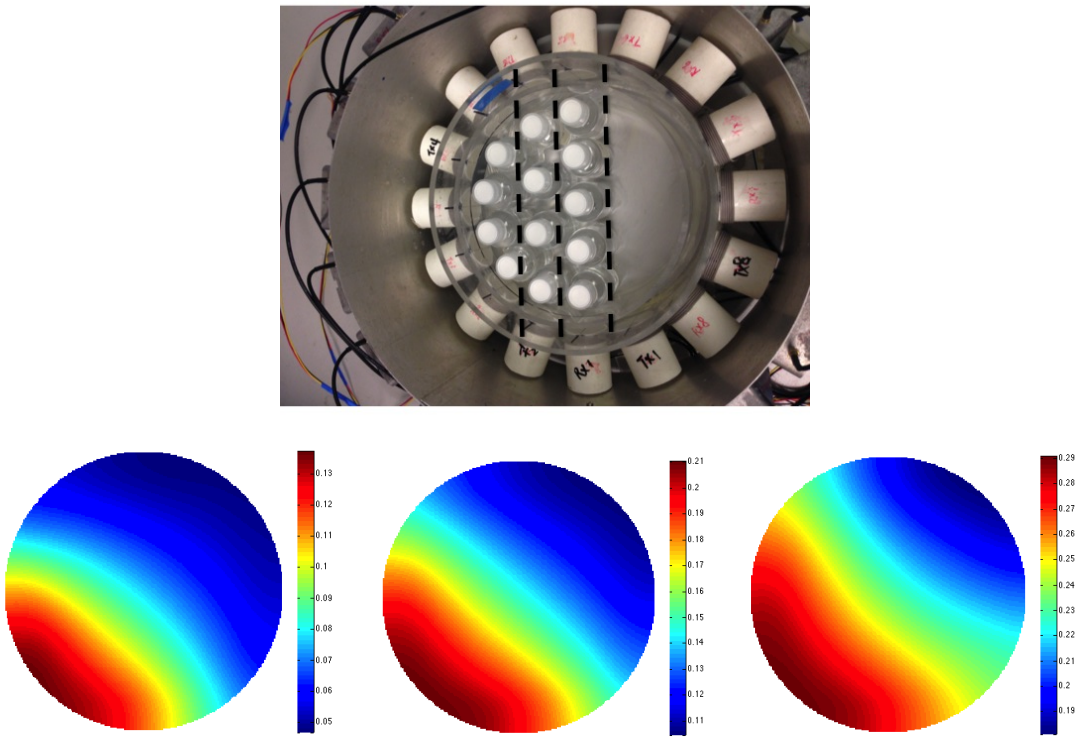

Figure 7.10: Experimental setup (top) and reconstructed images (bottom) of three strata, each of non-homogeous conductive fluids in a free space background. By volume, strata are 200*ml*, 400*ml* and 650*ml*, from the left to the right respectively.

7.3 Quasi-static Fluid Measurements

This section investigates the feasibility of gas bubble imaging in a flow rig. The inner diameter, outer diameter and the length of the flow rig are 190*mm*, 200*mm* and 800*mm* respectively. The flow rig is positioned centrally in the imaging region with a 16 channel coil array on the periphery (Figure 7.11).

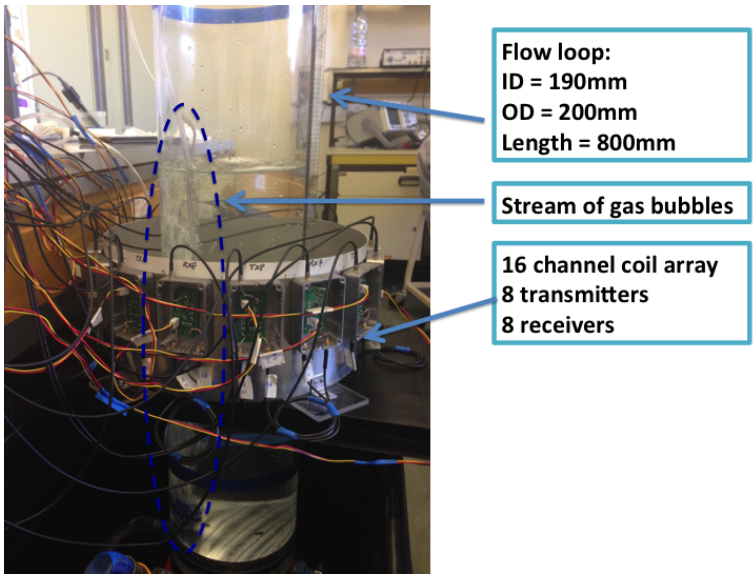

Figure 7.11: Bubble testing setup.

Five different conductive fluids are used in this experiment, with conductivities of $0.06S/m$, $1.81S/m$, $3.20S/m$, $5.13S/m$ and $12.64S/m$ respectively. The background data are taken from the empty flow rig, and the fluid measurements are taken when the flow rig is filled with different volumes of fluids, from 4, 6, 7, 8, 9, 10, 11, 12, 13 to 15 litres. Repeated measurements are also taken as the rig is drained. The aim of these tests is to assess both the sensitivity of the system, and the optimal range of conductivity range that can be accurately measured. In total, 95 sets of data are collected for evaluation. As the phase shift caused by the fluid is determined by both the conductivity value and the volume of the fluid, the phase shift varies accordingly. Figure 7.12 shows the norm value of the phase difference against the volume of fluid, when the total volume of the fluid increases from 4 to 15 litres at five different conductivity values. There is an increase in the norm value when the fluid begins to reach the bottom of the coil array, and as the volume of the fluid increases, the norm value decreases. Further increases in the volume result in consistent increases in the norm value of the phase difference, with eventual saturation of the phase perturbation after 12 litres of fluid.

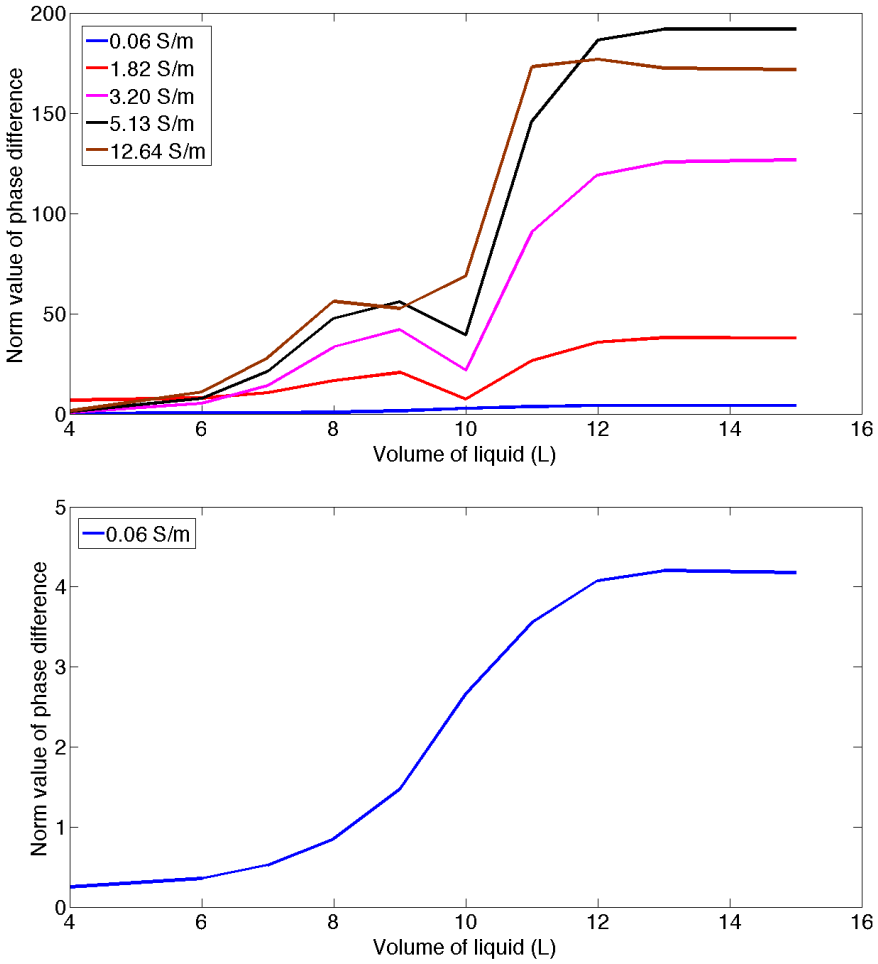

Figure 7.12: The norm value of the phase difference against the volume of the fluid for backgrounds with five different conductivities (top). Shown in blue, red, magenta, black, and brown are conductivities of $0.06S/m$, $1.81S/m$, $3.20S/m$, $5.13S/m$ and $12.64S/m$ respectively. The norm value of the phase difference against the volume of the fluid for a tap water background is shown in the bottom half of the figure.

The fluid reaches the centre of the imaging region when the flow rig is filled with 9 litres of fluid. Figure 7.13 shows the norm value of the phase difference for five different conductivity backgrounds when the flow rig is filled with 9 litres of fluid. There is a consistent increase in the norm value as the conductivity increases, which reaches its peak value at a conductivity of $5.13S/m$.

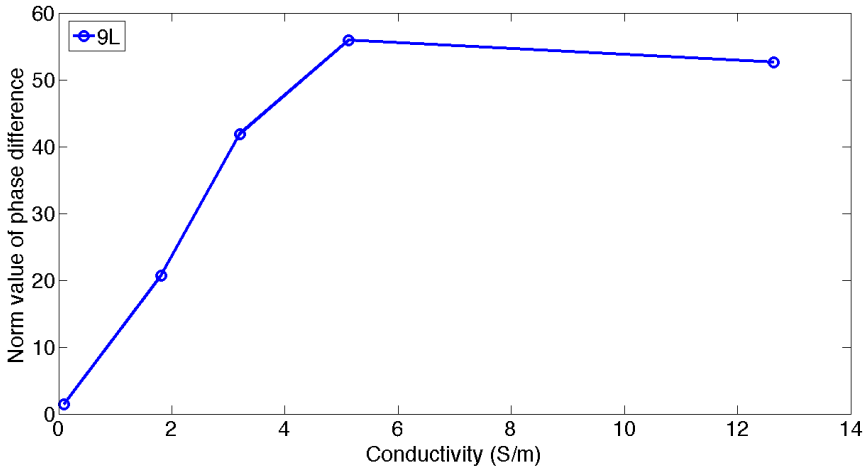

Figure 7.13: The norm value of the phase difference for five difference conductivity backgrounds ($0.06S/m$, $1.81S/m$, $3.20S/m$, $5.13S/m$ and $12.64S/m$ respectively) when the flow rig is filled with 9 litres of fluid, measurements were made between the coil pair Tx2 and Tx6.

Once the flow rig is filled with 15 litres of fluid, a stream of bubble gas is injected on the periphery at 2 points opposite each other (labelled position 1 and position 2 in Figure 7.14) to introduce the perturbation to the electromagnetic field. The aim of the experiment is to test whether the system can reconstruct an image of the bubbles. A snap shot of the bubble testing is reconstructed to show the average bubbles along the axial direction. The imaging results are shown in Figure 7.14; note the value of the scale decreases as the conductivity of the background decreases. Although the gas bubbles are themselves non-conductive, they are injected into a conductive background; as such, the areas that are injected with gas bubbles in fact have a non-homogenous non-conductive feature. This experiment can be considered the opposite of the experiment shown in Figure 7.10, where the results show the reconstructed images of a non-homogenous conductive medium in a non-conductive background.

Bubble position 1

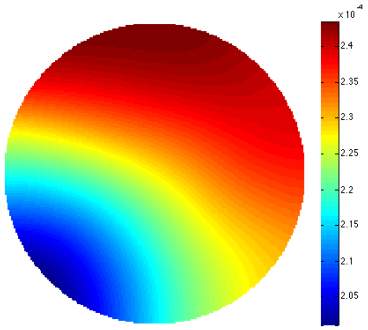

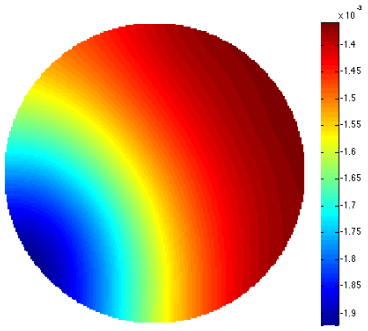

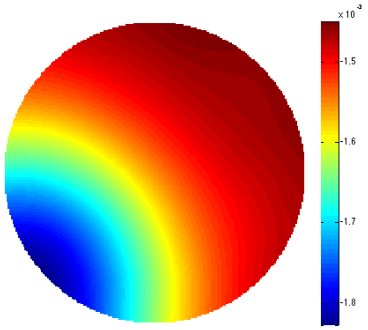

Bubble position 2

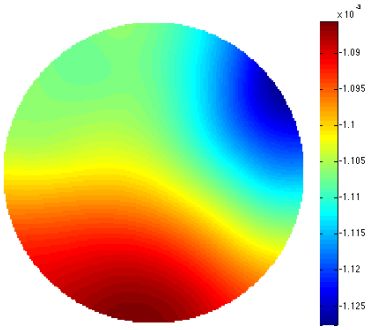

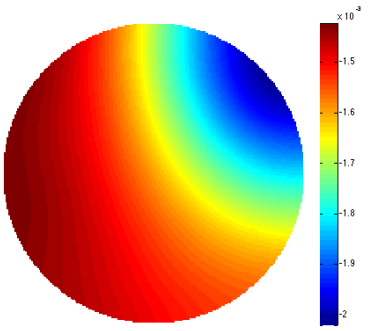

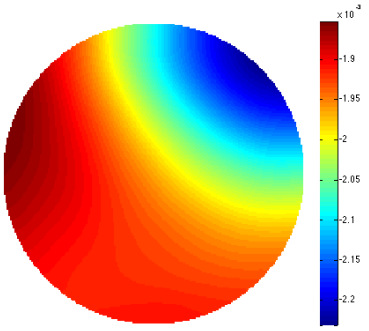

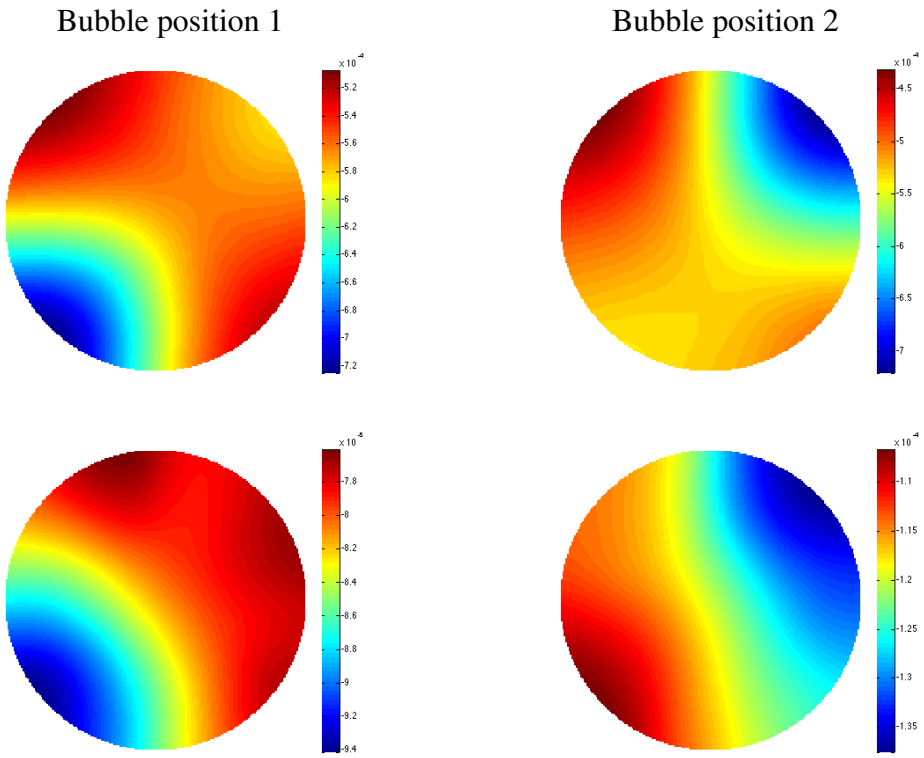

Figure 7.14: Reconstructed images of bubble flow in various backgrounds. Background conductivities are, by row, $12.64S/m$, $5.13S/m$, $3.20S/m$, $1.81S/m$ and $0.06S/m$ respectively.

Figure 7.15 shows the experimental setup and the reconstructed images of silicone oil within a saline solution. The silicone oil is bottled in a non-conductive container of height 180mm and outer diameter 130mm. The basal position of the container is initially placed at the bottom of the flow rig and raised by $5cm$ until it surpasses the fluid level. The experiment is performed twice, with a background conductivity of $1.81S/m$ and $12.64S/m$ respectively.

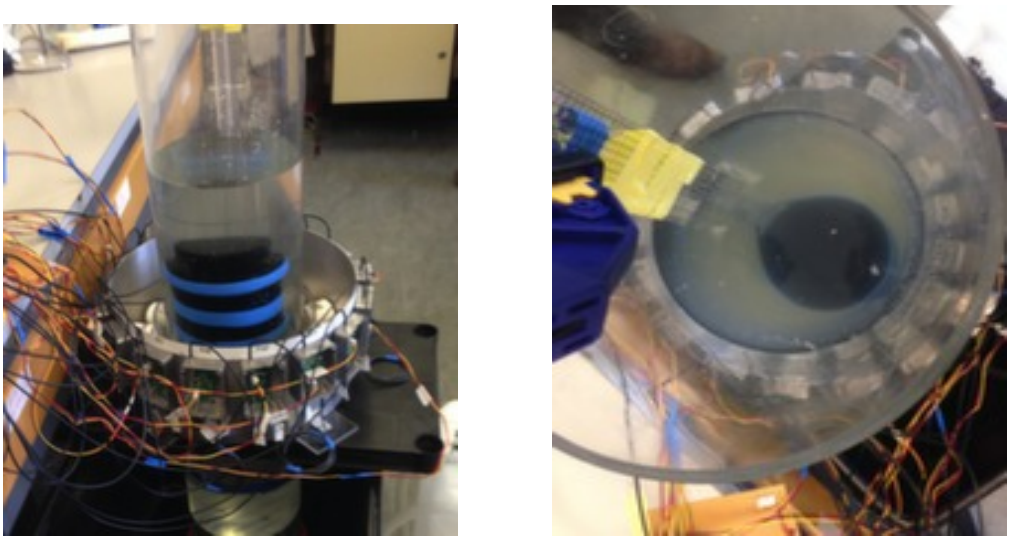

side-view top-view

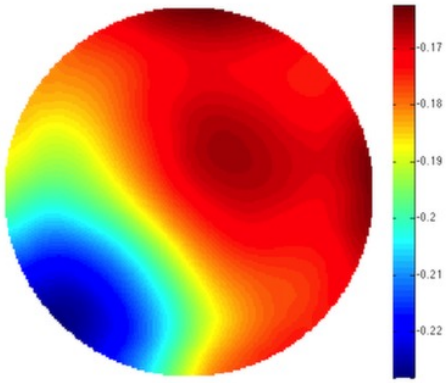

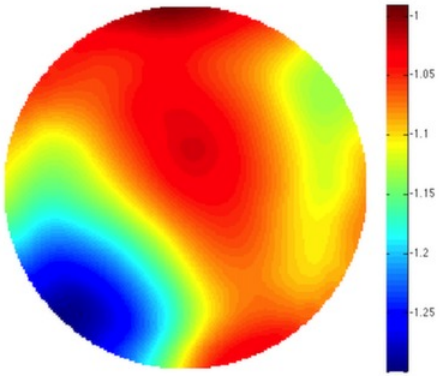

(a) (b)

Figure 7.15: Experimental setup of a silicone oil inclusion in two conductive backgrounds, with associated images. (a) silicone oil inclusion within a $1.81 S/m$ background, (b) silicone oil inclusion within a $12.64 S/m$ background.

Figure 7.16 shows the norm value for the phase difference resulting from the movement of the silicone oil along the axial direction within the conductive background. The distance whereby the silicone oil container is placed within the imaging region is set to be the reference distance, i.e., $0cm$ along the axial direction. For a background with $1.81 S/m$ conductivity, the norm value of the phase difference initially decreases; from $-15cm$ and greater, however, the value starts to increase. This is also called the fringe effect of the sensing region as the sensing area in the axial direction depends on the conductivity contrast between the background and the inclusion [202], consistent with the observations in Figure 7.12. The norm value of the phase difference reaches its peak when the silicone oil container arrives in the imaging region. Further increasing the distance, the value starts to decrease again. As the distance surpasses $15cm$, the silicone oil does not seem to cause any distinct perturbation in the phase difference. For the background with conductivity $12.64 S/m$, the overall norm value of the phase difference does not change as sharply as that for $1.81 S/m$. At $-20cm$, the norm value of the phase difference caused by background conductivities of $1.81 S/m$ and $12.64 S/m$ are 10.94 and 12.83 respectively. As

the norm value of the phase difference caused by a higher conductive background already exceeds its counterpart, at this point, the fringe effect is not observed between -20 to $-10cm$.

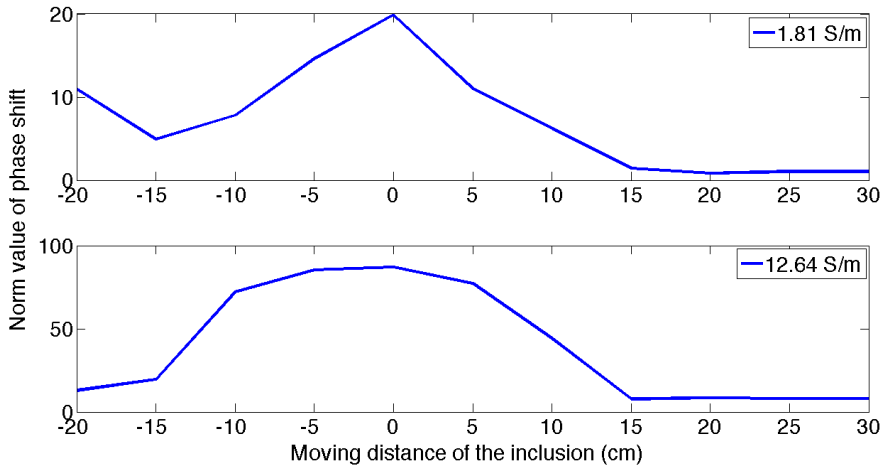

Figure 7.16: The norm value of the phase difference resulting from the movement of the silicone oil along the axial direction within two conductive backgrounds, $1.81S/m$ and $12.64S/m$ respectively.

7.4 Discussion

The visualisation of conductive phase flow is a challenging problem in industrial process tomography, with a need to develop a cost-effective, non-invasive yet robust imaging technique in this area. This study investigates the feasibility of MIT for this application and also highlights the difficulties associated with it. Four background measurements are collected by contrasting both non-conductive (free space and silicone oil) and conductive fluids (saline solution and tap water, with conductivities of $1.52S/m$ and $0.06S/m$, respectively) to represent a range of scenarios of potential interest in industrial process tomography. The results of static fluid tests confirm the viability of MIT in visualising the conductivity contrasts. We also found that the MIT phase measurements show a linear response with respect to electrical conductivity for a given dimension and location of an inclusion, while the phase changes arising from the changing dimensions of an inclusion have a non-linear relationship.

In addition, it is commonplace to have fluids separated into different layers by density, weight or conductivity in industrial process tomography. Tests of non-homogenous conductive fluids suggest that different strata of conductive fluids can be distinguished, and although in this case the distribution of eddy currents could differ from an industrial flow environment, we nevertheless show the potential of MIT in this respect. In industrial environments, there may be bubble flows of gas in the uppermost part of the flow pipe, and water only in the lowest part. The quasi-static experiments demonstrate the capability of MIT in obtaining a 2D image of bubble flow along the axial dimension of various

conductive backgrounds, including water.

These quasi-static experiments also reveal that there is a strong fringing field effect of the MIT sensing region, consistent with similar observations in [203]. This suggests that a 3D MIT system might be more robust compared to a 2D system, particularly in obtaining the axial information of the fluid. Future studies will focus on this aspect with the purpose to design a cost effective 3D system, and subsequently develop real time 3D reconstruction algorithms. For any conductivity contrast lower than the conductivity contrast presented in this study, other contactless imaging techniques such as electrical capacitance tomography might be able to operate. A combined capacitance and inductive tomographic system will be studied in order to image both dielectric and conductive phase contrasts. In our continued effort, we will develop a more robust MIT hardware capable of working in industrial environments, including both the mechanical design of the sensors and improvement in hardware electronics.

Finally, it is worth mentioning that in principle, the inverse problem needs to be solved according to each specific imaging case. As such, the image reconstruction algorithm needs to be applied according to each individual imaging subject. This would introduce additional parameters (i.e., the number of iterations, the regularisation parameters or matrices) to this study, alongside the number, size and position of inclusions, and the conductivity contrast. Therefore, in this study, a universal linear inverse algorithm is used to reconstruct images with pre-calculated regularisation parameters for all cases (equation 2.56). This way, it is guaranteed that any change in the image reconstruction is in fact due to the change in the fluid distribution patterns rather than the image reconstruction software model, although this does suggest that the inverse model might not be optimal for certain cases. In future studies, a nonlinear image reconstruction algorithm might be necessary to enhance the resolution of the two phase contrasts, if it can be developed in such a manner as to computationally efficient for the purpose of real time imaging.

Chapter 8

Conclusions

8.1 Summary

This thesis studies the feasibility and capability of MIT in non-destructive evaluation and process tomography applications. Topic of interests include the inspection of pipelines, identification of hidden defects in carbon fibre reinforced polymers, 3D subsurface imaging of metallic structures and visualisation of two-phase flow. The applications proposed in chapters 3 to 6 are based on the Bath MK-I MIT system, which was designed for imaging materials with conductivity higher than $10^5 S/m$. The application of two-phase flow imaging is presented in chapter 7, which is based on the Bath MK-II MIT system. This system was designed for imaging subjects with conductivity lower than $10 S/m$. Although each chapter studies a specific research topic, they are consistent in several ways. Firstly, the coil arrays are designed specifically for the geometries of the imaging subjects in order to employ the flexibility of MIT in this respect. Secondly, each chapter presents an experimental evaluation of MIT for the proposed application; as such the viability and capability of MIT for its intended use can be demonstrated through experimental results. Thirdly, each chapter provides an insight as to how MIT can be used and further developed towards a commercial technique in each field for the purpose of expanding the wide applicability of MIT.

8.2 Remarks

Chapter 3 shows that MIT is capable of imaging structural damage to pipe samples, an application never before attempted. Both external and internal wall losses on aluninium pipe walls and external damage to steel pipes are inspected using the proposed MIT system. A novel image reconstruction method is developed specifically for this application, which achieves an unprecedented resolution in the field of 2%. The simulated voltages obtained from the forward model are validated against the experimental measurements, ensuring the accuracy of the software model. Altogether, these results demonstrate the

applicability of MIT as an NDE technique for industrial pipeline inspection, as a proof of principle.

Chapter 4 presents a means by which MIT could be employed as a NDE technique for carbon fibre reinforced polymers (CFRPs). This extends the employability of MIT from traditional metallic structures to new composite materials. A dual planar coil array is designed to accommodate the geometry of the imaging subject. The experimental results demonstrate that both single and multiple hidden defects can be inspected, with reconstructed images of sufficient accuracy. It is worth noting that in this study, only CFRPs with an isotropic character are investigated. In a follow up study, one should modify the forward model to accommodate materials with anisotropic characteristics in order to expand the employability of MIT. In addition, further studies should also focus on improving the system imaging speed for real time inspection. These suggest that with continued effort, MIT could evolve be become a rapid inspection tool during the initial manufacturing stage of CFRPs.

In both chapters 3 and 4, the imaging subjects are accessible to the MIT system. Chapter 5 aims to address a challenge whereby there is only limited access to the imaging target, i.e., if the measurements can only be obtained from one surface, as is the case with 3D surface imaging. By developing a planar array to provide volumetric and penetrable measurements beneath the imaging subject, this study provides a means by which 3D surface imaging is demonstrably viable. The detectable depth is shown to be approximately $3-4cm$ underneath the imaging surface. Although seemingly limited, this chapter represents the first 3D experimental planar work in the field, and opens up opportunities for MIT to be used as a subsurface inspection tool. Implementing a multi-frequency MIT could be a solution to improve the penetration depth, which will be studied in a future work.

It is apparent that in a MIT system, limited access to the imaging target results in a restricted number of measurements. As such, chapter 6 explores the relationship between image quality and the number of available measurements in both a qualitative and quantitative manner, the latter by systematically creating missing data scenarios experimentally in 2D. Two scenarios are established by undersampling the data and using limited angle tomography. The interest of this work lies in the fact that these findings could offer insight into how, for large scale MIT with a large quantity of data, undersampling of data may be an efficient means by which rapid data processing can be achieved without compromising image quality. We also extend the limited data concept to 3D imaging, with consistent observations.

Chapter 7 presents an experimental evaluation of MIT in conductive phase flow imaging. Experiments are conducted covering as broad a range of conductivity contrasts as possible, so as to encompass several scenarios of potential interest in industrial flow environments. The fluid experiments include (a) the smallest conductivity contrast in which image reconstruction in various non-conductive and conductive backgrounds is possible,

(b) distinguishing three strata of non-homogenous conductive fluids in free space, and (c) imaging a flow of non-homogenous bubbles of gas in various conductive backgrounds. Taken together, this study demonstrates various capabilities of an MIT system in conductive phase imaging.

8.3 Limitations and Immediate Research

Further development on pipeline inspection using MIT in chapter 3 should focus on system improvement in three aspects. Firstly, the system development should draw attention to the design of an agile MIT sensing array in order to adapt to various pipeline geometries and accurately obtain the measurements for reconstruction. Secondly, a rapid data collection and image reconstruction module are essential to ensure real time inspection. Thirdly, the overall system should be developed so as to be suitable for more diverse industrial environments, such as those characterised by a high temperature, radiation or pressure, undersea conditions or buried pipelines.

As to the future study of the hidden defect identification in carbon fibre reinforced polymers (CFRPs) using MIT in chapter 4, an in-depth study of anisotropic characteristics of CFRP is necessary in order to expand this applicability of MIT to various structures. It is also worth investigating if the impact damage in CFRP can be inspected by MIT. This could require a MIT system that is capable for real time inspection.

In addition to further improve the depth penetration of planar MIT (PMIT) system in chapter 5, the author will investigate what is the smallest volume of metallic structure in an imaging subject that can be detected underneath the sensing array, and the maximum detection depth under these circumstances. To improve the penetration depth, implementing a multi-frequency MIT system could be a suitable approach.

The conclusions made in chapter 6 can be used to provide a guidance as to what extent undersampling the data is viable for achieving fast data collection without compromising the image resolution. In the absence of a large scale MIT system, the author will develop a simulation model of a large scale MIT system - for instance, with 256 coils - to validate the predications made in chapter 6.

Experimental investigation of conductive flow imaging using MIT in chapter 7 reveals that 3D MIT could be the future direction in terms of system design in order to improve the system's ability and to be more efficient in capturing the axial dimension of the flow information. In addition, a classification work is needed to establish the boundaries of MIT in imaging the conductive flow, as well as attempting to carry out testing on industrial flow regimes. This would also require the system to be equipped with real time data collection capability.

The methodologies needed to achieve these goals are summarised in 8.5.

8.4 Contributions to Knowledge

Considering the novel elements of the research undertaken, the following contributions to knowledge are claimed:

- The first proposed use of MIT for industrial pipeline inspection, after establishing the feasibility and capability of MIT in imaging the structures of pipelines.
- The development of a novel image reconstruction algorithm, the narrow pass filtering method, which enables an unprecedented MIT resolution of 2% compared to the traditional resolution of 10-15%.
- The first experimental work conducted on 3D planar MIT for near subsurface imaging, which demonstrates the ability of MIT as a limited access tomographic technique to offer volumetric and penetrative measurements.
- The first experimental characterisation of the missing data effect in MIT based on researching various coil array geometries both qualitatively and quantitatively, and in both 2D and 3D scenarios.
- A demonstration of the capability of MIT in inspecting hidden defects in carbon fibre reinforced materials using 3D experimental results.
- The first experimental evaluation of static fluids, quasi-static fluids and flow rig testing in the field of MIT research, reporting the feasibility of MIT at distinguishing two-phase conductive flow.

During the course of this PhD, the outcomes of this research have been published in 9 journal articles, and presented at several relevant national and international conferences. Detailed publications are attached in appendix A.

8.5 Future Work

8.5.1 Forward and Inverse Problems

MIT resolution suffers from poor spatial resolution as the inverse problem in MIT is inherently an ill-posed problem. In this respect, it is desirable to improve the image resolution of MIT in order to expand the applicability of this technique. Chapter 3 presents pipeline inspection using a narrowband pass filtering method (NPFM) for image reconstruction. This is a case study of limited region tomography. The imaging region is limited to specific pipe geometries by implementing a NPFM. This is an effective approach to improve MIT image resolution by increasing the number of useful pixels in the region of interest. However, this method requires the centre of the pipe to match the centre of the imaging region. This is the main disadvantage of this method, which needs to be addressed if *a*

priori information of the pipe is unknown. As discussed in chapter 6, missing data can further result in a degraded image quality. However, it is also shown that the targeted objects are detectable as long as they are placed within the region of interest, as is the case in several limited angle scenarios. This suggests that limiting the imaging region can compensate for information loss, especially if access to the imaging subject is restricted. Based on the observation obtained from both chapters, it is anticipated that for limited access scenarios, limiting the region could help to improve the image quality.

In future work, the author will aim to overcome the inflexibility of NPFM by using a level set method [48, 168, 170]. The level set method can be used to establish the boundary of the conductive inclusion, and as such, it can provide an estimate of the location and the dimension of the imaging subject. Implementing the level set method would require the use of a non-linear iterative method to solve the forward model, which could be computationally expensive. This also applies when modeling CFRPs with anisotropic characteristics - the forward problem needs to be solved according to a specific case in order to ensure the accuracy of the sensitivity maps. The author proposes that the computational cost can be overcome by implementing graphics processing units (GPUs) for high performance computing [204, 205, 206, 207, 208].

In addition, various MIT geometries such as planar and arc, as well as the limited data in both 2D and 3D cases have been investigated in this thesis. These geometries are studied as each of them has its own potential uses and interests. These geometries have limited measurements, which consequently weakens the MIT resolution. In a future study, the author will aim to develop more sophisticated algorithms specifically for these geometries, which could be of benefit to MIT resolution. More importantly, developing algorithms that can be run in real time is crucial in order to use MIT in an industrial environment.

8.5.2 System Improvements

One should note that there is no universal design approach for all MIT applications, and that the hardware of a MIT system should be catered to its proposed application. Although there are few studies which focus on the specific design of a MIT coil array [94, 209, 210, 211, 212, 213], there is no study reported that covers the design of all sub-components of a MIT system. Although hardware development is not the focus of this thesis, there are several improvements that can be made to the existing systems.

The MK-I system is designed for imaging material with conductivity above $10^5 S/m$. The system was initially designed to accommodate 16 channels, and later expanded to 32 channels by adding an additional multiplexer and an inverter for data switching. This suggests that for an array with more than 32 coils, this system will no longer be suitable, although this is not considered a pressing issue - currently used systems do not exceed 24 coils. In addition to its channel capacity, one disadvantage of this system is that it is not ideal for real time imaging, especially if all 32 channels are utilised. The measurement data has to be collected and stored off-line for image reconstruction. This limitation

needs to be overcome in order to expand the applicability of MIT in NDE applications and process tomography. Furthermore, in this thesis, all the coil arrays, pin connections and cabling were hand made. In an ideal case, these have to be designed in a sophisticated manner to ensure low noise perturbation and better transmission of the signals [214].

The MK-II MIT system was designed for material with conductivity value lower than $10S/m$, therefore it was proposed for conductive flow imaging, a challenging topic in industrial process tomography. In chapter 7, it is shown that there is a strong fringing effect in the sensor region. This suggests that a 3D MIT system might be more robust compared to a 2D system, particularly in obtaining the axial information of the fluid. Future studies will focus on this aspect with the purpose of designing a cost effective 3D system, and subsequently develop real time 3D reconstruction algorithms, in conjunction with section 8.5.1.

8.5.3 Multi-frequency MIT

The electrical conductivity $\sigma = \sigma(x)$ contributes important functional information for many MIT applications. Although for a given system and a targeted problem the frequency is fixed, one should note that the conductivity is frequency dependent, i.e., $\sigma = \sigma(x, \omega)$. Developing an excitation source capable of providing multiple frequencies could enhance the detectability of a MIT system [19, 184, 185]. In chapter 3, inspection of internal damage was found particularly challenging as the chosen frequency cannot penetrate the steel pipe wall. This issue will become more prominent with increasingly thick pipe walls. This issue is also presented in chapter 5 for subsurface imaging. Decreasing the frequency will increase the skin depth, which is used to describe the penetration of magnetic field below the surface of the test object. The skin depth δ, is defined as:

$$\delta = \sqrt{\frac{2}{\omega \mu_0 \mu_r \sigma}}$$

where ω is angular frequency, μ_0 and μ_r are unity and relative magnetic permeability, σ is electrical conductivity. High frequency measurements give information regarding the properties adjacent to the surface, whereas low frequency testing probes deeper inside the test sample [19, 185]. For non-magnetic, electrically conductive metals, i.e., $\mu_r = 1$, a single selected frequency might meet the skin depth requirement. However, for other materials such as steel, where both conductivity and permeability play important roles, using a single selected frequency cannot satisfy the image reconstruction demand. A selection of frequencies for excitation in MIT could improve the information from a MIT system and make it more robust against the depth of the anomaly.

The major challenges of implementing multi-frequency MIT fall on both conditioning electronics and software control. It is desirable to design an excitation channel which provides a selection of frequencies. The signal demodulation also needs to be capable

of demodulating one selected frequency to be fed into an excitation coil from a multi-frequency system. Additionally, enhancing the MIT software to be able to collect multi-frequency data as well as developing a spectral and frequency difference reconstruction are equally important, especially for anisotropic composite structures [215, 216]. Of particular interest is frequency difference imaging, which could be useful if the test subjects show different responses to frequency variation. This study will be carried out in conjunction with the research topics discussed in sections 8.5.1 and 8.5.2.

Appendix A

List of publications

Journal Articles:

1. **Ma, L.**, Hunt, A and Soleimani, M. (2014) Experimental evaluation of conductive flow imaging using magnetic induction tomography. *International Journal of Multiphase Flow*, under review.

2. **Ma, L.**, Banasiak, R and Soleimani, M. (2014) Magnetic induction tomography with high performance GPU implementation. *International Journal of High Performance Computing Applications,* under review.

3. Zhang, M., **Ma, L.** and Soleimani, M. (2014) Magnetic induction tomography guided electrical capacitance tomography imaging with grounded conductors. *Measurement*, 53, pp. 171–181.

4. **Ma, L.** and Soleimani, M. (2014) Hidden defect identification in carbon fibre reinforced polymer plates using magnetic induction tomography. *Measurement Science & Technology*, 25(5), pp. 055404.

5. Evangelidis, M., **Ma, L.**, and Soleimani, M. (2013) High definition electrical capacitance tomography for pipeline inspection. *Progress In Electromagnetics Research*, 141, pp. 1- 15.

6. **Ma, L.**, Wei, H.-Y. and Soleimani, M. (2013) Planar magnetic induction tomography for 3D near subsurface imaging. *Progress In Electromagnetics Research*, 138, pp. 65-82.

7. **Ma, L.** and Soleimani, M. (2012) Limited angle and limited data electromagnetic induction tomography: experimental evaluation of the effect of missing data. *Measurement Science & Technology*, 23 (12), pp. 125406.

8. Wei, H.-Y., **Ma, L.** and Soleimani, M. (2012) Volumetric magnetic induction tomography. *Measurement Science & Technology*, 23 (5), pp. 055401.

9. **Ma, L.** and Soleimani, M. (2012) Electromagnetic imaging for internal and external inspection of metallic pipes. *Insight: Non-Destructive Testing and Condition Monitoring*, 54 (9), pp. 493-495.

10. **Ma, L.**, Wei, H.-Y. and Soleimani, M. (2012) Pipeline inspection using magnetic induction tomography based on a narrowband pass filtering method. *Progress In Electromagnetics Research M*, 23, pp. 65-78.

Conference Articles:

1. **Ma, L.** and Soleimani, M. (2014) Critical evaluation of two phase low conductivity flow imaging using magnetic induction tomography. *In: 5th International Workshop on Process Tomography*, Jeju, South Korea.

2. Zhang, M., **Ma, L.** and Soleimani, M. (2014) Dual modality ECT-MIT three-phase flow imaging. *In: 5th International Workshop on Process Tomography*, Jeju, South Korea.

3. **Ma, L.** and Soleimani, M. (2014) A hybrid image reconstruction for medical magnetic induction tomography: an experimental evaluation. *In: 15th International Conference on Biomedical Applications of Electrical Impedance Tomography*, Gananoque, Canada.

4. **Ma, L.** and Soleimani, M. (2013) Industrial pipeline inspection using magnetic induction tomography. *In: 7th World Congress in Industrial Process Tomography (WCIPT7)*, Krakow, Poland.

5. Zhang, M., **Ma, L.**, Ye, Z., Yang, C. L., Wei, H. Y., Banasiak, R. and Soleimani, M. (2013) Near subsurface 3D imaging using planar array: EIT, ECT, MIT. *In: 7th World Congress in Industrial Process Tomography (WCIPT7)*, Krakow, Poland.

6. **Ma, L.**, Wei, H.-Y. and Soleimani, M. (2012) Cryosurgical monitoring using electromagnetic measurements: a feasibility study for magnetic induction tomography. *In: 13th International Conference in Electrical Impedance Tomography*, Tianjin, China.

7. Wei, H.-Y., **Ma, L.** and Soleimani, M. (2012) Three dimensional magnetic induction tomography imaging using multi-plane coil arrays. *In: 6th International Symposium on Process Tomography*, Cape Town, South Africa.

8. Wei, H., Yang, C., **Ma, L.**, Ye, Z., Yao, A. and Soleimani, M. (2012) Three-dimensional industrial process tomography using electrical and electromagnetic tomography: recent developments. *In: 2012 IEEE I2MTC - International Instrumentation and Measurement Technology Conference*, Proceedings. IEEE, pp. 912-915.

Bibliography

[1] F. J. Dickin, B. S. Hoyle, A. Hunt, S. M. Huang, O. Ilyas, C. Lenn, R. C. Waterfall, R. A. Williams, C. G. Xie, and M. S. Beck. Tomographic imaging of industrial process equipment: techniques and applications. In *Circuits, Devices and Systems, IEE Proceedings G*, volume 139, pages 72–82. IET, 1992.

[2] A. J. Peyton. Electrical tomography for industrial applications (presentation).

[3] H. Griffiths. Magnetic induction tomography. *Measurement Science and Technology*, 12:1126–1131, 2001.

[4] David S. Holder. *Electrical impedance tomography: methods, history, and applications*. CRC Press, Bristol, 2005.

[5] J. G. Webster and P. D. Hughes. Electrical impedance tomography. *Journal of Clinical Engineering*, 16(4):349, 1991.

[6] F. Sattar. Rot detection in wooden poles using electrical impedance tomography. Master's thesis, Department of Electrical Engineering, University of Cape Town, 2005.

[7] S. Liu, Q. Chen, X. Xiong, Z. Zhang, and J. Lei. Preliminary study on ect imaging of flames in porous media. *Measurement Science and Technology*, 19(9):094017, 2008.

[8] Y. Yan, T. Qiu, G.Lu, M. Hossain, G. Gilabert, and S. Liu. Recent advances in flame tomography. *Chinese Journal of Chemical Engineering*, 20(2):389–399, 2012.

[9] R. C. Waterfall, R. He, P. Wolanski, and Z. Gut. Flame visualizations using electrical capacitance tomography (ect). *Process Imaging for Automatic Control*, pages 242–250, 2001.

[10] L.-S. Fan, W. Warsito, and B. Du. Electrical capacitance tomography imaging of gas-solid and gas-liquid-solid fluidized bed systems. *Journal of Visualization*, 7(1):5, 2004.

[11] Z. Yingna and L. Qiang. Review of techniques for the mass flow rate measurement of pneumatically conveyed solids. *Measurement*, 44(4):589–604, 2011.

[12] Z. Y. Huang, B. L. Wang, and H. Q. Li. Application of electrical capacitance tomography to the void fraction measurement of two-phase flow. *IEEE Transactions on Instrumentation and Measurement*, 52(1):7–12, 2003.

[13] H. Griffiths, W. R. Stewart, and W. Gough. Magnetic induction tomography: a measuring system for biological tissues. *Annals of the New York Academy of Sciences*, 873:335–345, 1999.

[14] G. Jin, J. Sun, M. Qin, Q. Tang, L. Xu, X. Ning, J. Xu, X. Pu, and M. Chen. A new method for detecting cerebral hemorrhage in rabbits by magnetic inductive phase shift. *Biosensors and Bioelectronics*, 52:374–378, 2014.

[15] R. Merwa, K. Hollaus, O. Biró, and H. Scharfetter. Detection of brain oedema using magnetic induction tomography: a feasibility study of the likely sensitivity and detectability. *Physiological Measurement*, 25(1):347–354, 2004.

[16] H. Scharfetter, P. Riu, M. Populo, and J. Rosell. Sensitivity maps for low-contrast perturbations within conducting background in magnetic induction tomography. *Physiological Measurement*, 23(1):195–202, 2002.

[17] L. F. Fuks, M. Cheney, D. Isaacson, D. G. Gisser, and J. C. Newell. Detection and imaging of electric conductivity and permittivity at low frequency. *IEEE Transactions on Biomedical Engineering*, 38(11):1106–1110, 1991.

[18] X. Ma, A. J. Peyton, S. R. Higson, A. Lyons, and S. J. Dickinson. Hardware and software design for an electromagnetic induction tomography (emt) system for high contrast metal process applications. *Measurement Science and Technology*, 17(1):111–118, 2006.

[19] X. Ma, A. J. Peyton, S. R. Higson, and P. Drake. Development of multiple frequency electromagnetic induction systems for steel flow visualization. *Measurement Science and Technology*, 19(9):094008, 2008.

[20] A. J. Peyton, Z. Yu, Z. Zhi, S. Al-Zeibak, N. H. Saunders, and A. R. Borges. Electromagnetic imaging using mutual inductance tomography: potential for process applications. *Particle and Particle Systems Characterization*, 12(2):68–74, 1995.

[21] A. Korjenevsky, V. Cherepenin, and S. Sapetsky. Magnetic induction tomography: experimental realization. *Physiological Measurement*, 21(1):89, 2000.

[22] M. Cheney, D. Isaacson, and J. C. Newell. Electrical impedance tomography. *SIAM review*, 41(1):85–101, 1999.

[23] C. Ktistis, D. W. Armitage, and A. J. Peyton. Calculation of the forward problem for absolute image reconstruction in mit. *Physiological Measurement*, 29:S455–S464, 2008.

[24] D. N. Dyck, D. A. Lowther, and E. M. Freeman. A method of computing the sensitivity of the electromagnetic quantities to changes in the material and sources. *IEEE Transactions on Magnetics*, 30:3415–3418, 1994.

[25] C. S. Biddlecombe, E. A. Heighway, J. Simkin, and C. W. Trowbridge. Methods for eddy current computation in three dimensions. *IEEE Transactions on Magnetics*, 18(2):492–497, Mar 1982.

[26] M. V. K. Chari, A. Konrad, M. Palmo, and J. D'Angelo. Three-dimensional vector potential analysis for machine field problems. *IEEE Transactions on Magnetics*, 18(2):436–446, Mar 1982.

[27] T. Morisue. Magnetic vector potential and electric scalar potential in three-dimensional eddy current problem. *IEEE Transactions on Magnetics*, 18(2):531–535, Mar 1982.

[28] D. Rodger and J. F. Eastham. A formulation for low frequency eddy current solutions. *IEEE Transactions on Magnetics*, 19(6):2443–2446, Nov 1983.

[29] W. Renhart, H. Stogner, and K. Preis. Calculation of 3d eddy current problems by finite element method using either an electric or a magnetic vector potential. *IEEE Transactions on Magnetics*, 24(1):122–125, Jan 1988.

[30] M. N. Tek and N. G. Gencer. A new 3d fem formulation for the solution of potential fields in magnetic induction problems. In *Engineering in Medicine and Biology Society, 1997. Proceedings of the 19th Annual International Conference of the IEEE*, volume 6, pages 2470–2473, 1997.

[31] R. Merwa, K. Hollaus, B. Brandstatter, and H. Scharfetter. Numerical solution of the general 3d eddy current problem for magnetic induction tomography (spectroscopy). *Physiological Measurement*, 24(2):545–554, 2003.

[32] O. Biró. Edge element formulations of eddy current problems. *Computer Methods in Applied Mechanics and Engineering*, 169:391–405, 1999.

[33] O. Biró and K. Preis. An edge finite element eddy current formulation using a reduced magnetic and a current vector potential. *IEEE Transactions on Magnetics*, 36(5):3128–3130, 2000.

[34] O. Biró, K. Preis, W. Renhart, K. R. Richter, and G. Vrisk. Performance of different vector potential formulations in solving multiply connected 3d eddy current problems. *IEEE Transactions on Magnetics*, 26(2):438–441, 1990.

[35] A. Kameari. Three dimensional eddy current calculation using edge element for magnetic vector potential. *International Journal of Applied Electromagnetics and Mechanics*, pages 225–236, 1986.

[36] D. C. Barber and B. H. Brown. Applied potential tomography. *Journal of Physics E: Scientific Instruments*, 17(9):723–734, 1984.

[37] N. A. Golias, C. S. Antonopoulos, T. D. Tsiboukis, and E. E. Kriezis. 3d eddy current computation with edge elements in terms of the electric intensity. *The International Journal for Computation and Mathematics in Electrical and Electronic Engineering*, 17(5/6):667–673, 1998.

[38] V. Thomee. *Galerkin Finite Element Methods for Parabolic Problems*. Springer, 2nd ed edition, 2006.

[39] B. Riviere. *Discontinuous Galerkin methods for solving elliptic and parabolic equations: theory and implementation*. Siam, 2008.

[40] M. Soleimani and W. R. B. Lionheart. Absolute conductivity reconstruction in magnetic induction tomography using a nonlinear method. *IEEE Transactions on Medical Imaging*, 25(12):1521–1530, 2006.

[41] M. Soleimani, W. R. B. Lionheart, A. J. Peyton, X. Ma, and S. R. Higson. A three-dimensional inverse finite-element method applied to experimental eddy-current imaging data. *IEEE Transactions on Magnetics*, 42(5):1560–1567, 2006.

[42] M. Soleimani, W. R. B. Lionheart, and A. J. Peyton. Image reconstruction for high-contrast conductivity imaging in mutual induction tomography for industrial applications. *IEEE Transactions on Instrumentation and Measurement*, 56(5):2024–2032, 2007.

[43] H. Igarashi and T. Honma. On convergence of iccg applied to finite-element equation for quasi-static fields. *IEEE Transactions on Magnetics*, 38(2):565–568, 2002.

[44] M. Soleimani and W. R. B. Lionheart. Image reconstruction in three-dimensional magnetostatic permeability tomography. *IEEE Transactions on Magnetics*, 41:1274–1279, 2005.

[45] Z. Z. Yu, A. J. Peyton, and M. S. Beck. Optimum excitation field for non-invasive electrical and magnetic tomography sensors. In *Proceedings of European Concerted Action in Process Tomography*, pages 311–320, Bergen, Norway, 1995.

[46] A. J. Peyton, M. S. Beck, A. R. Borges, J. E. de. Oliveira, G. M. Lyon, Z. Z. Yu, M. W. Brown, and J. Ferrerra. Development of electromagnetic tomography (emt) for industrial applications. part 1: sensor design and instrumentation. In *1st World Congress on Industrial Process Tomography*, pages 306–312, Buxton, UK, 14-17 April 1999.

[47] Z. Z. Yu, A. J. Peyton, and M. S. Beck. Electromagnetic tomography (emt), part i: Design of a sensor and a system with a parallel excitation field. In *IEE Proceedings*

of Science, Measurement and Technology, pages 147–154, Oporto, Portugal, 24-26 March 1994.

[48] M. Soleimani, O. Dorn, and W. R. B. Lionheart. A narrow-band level set method applied to eit in brain for cryosurgery monitoring. *IEEE Transactions on Biomedical Engineering*, 53(11):2257–2264, 2006.

[49] R. S. Blue. *Real-time three-dimensional linearized reconstruction algorithm generalized for multiple planes of electrodes*. PhD thesis, Rensselaer Polytechnic Institute,Troy, NY, 1997.

[50] A. P. Calderon. On an inverse boundary value problem. *Seminar on Numerical Analysis and Its Applications to Continuum Physics, Soc. Brasileira de Matematica, Rio de Janeiro*, pages 65–73, 1980.

[51] M. Cheney, D. Isaacson, and E. L. Isaacson. Exact solutions to a linearized inverse boundary value problem. *Inverse Problems*, 6(6):923–934, 1990.

[52] D. Isaacson and M. Cheney. Current problems in impedance imaging. *Inverse Problems In Partial Differential Equations*, pages 141–149, 1990.

[53] M. Ziolkowski, S. Gratkowski, and R. Palka. Solution of three dimensional inverse problem of magnetic induction tomography using tikhonov regularization method. *International Journal of Applied Electromagnetics and Mechanics*, 30(3 - 4):245–253, 2009.

[54] R. Merwa, P. Brunner, A. Missner, K. Hollaus, and H. Scharfetter. Solution of the inverse problem of magnetic induction tomography (mit) with multiple objects: analysis of detectability and statistical properties with respect to the reconstructed conducting region. *Physiological Measurement*, 27:S249–S259, 2006.

[55] R. Merwa and H. Scharfetter. Magnetic induction tomography: analysis of resolution an object shifting. In *Proceedings of the World Congress on Medical Physics and Biomedical Engineering*, Seoul, Südkorea, 2006.

[56] R. Merwa, K. Hollaus, P. Brunner, and H. Scharfetter. Solution of the inverse problem of magnetic induction tomography (mit). *Physiological Measurement*, 26(2):307–318, 2005.

[57] W. R. B. Lionheart, M. Soleimani, and A. J. Peyton. Sensitivity analysis in 3d magnetic induction tomography. In *Proceedings 3rd World Congress on Industrial Process Tomography*, pages 239–244, Canada, 2003.

[58] G. S. Park and D. S. Kim. Development of a magnetic inductance tomography system. *IEEE Transactions on Magnetics*, 41(5):1932 – 1935, may 2005.

[59] Z. Z. Yu, A. J. Peyton, W. F. Conway, L. A. Xu, and M. S. Beck. Imaging system based on electromagnetic tomography (emt). *Electronics Letters*, 29(7):625–626, 1993.

[60] S. Al. Zeibak and N. H. Saunders. A feasible study of in vivo electromagnetic imaging. *Physics in Medicine and Biology*, 38:151–160, 1993.

[61] A. J. Peyton, Z. Z. Yu, G. Lyon, S. Al-Zeibak, J. Ferreira, J. Velez, F. Linhares, A. R. Borges, H. L. Xiong, N. H. Saunders, and M. S. Beck. An overview of electromagnetic induction tomography: description of three different systems. *Measurement Science and Technology*, 7:261–271, 1996.

[62] F. Santosa and M. Vogelius. A backprojection algorithm for electrical impedance imaging. *SIAM Journal on Applied Mathematics*, 50(1):216–243, 1990.

[63] W. Q. Yang and L. H. Peng. Image reconstruction algorithms for electric capacitance tomography. *Measurement Science and Technology*, 14(1):1–13, 2003.

[64] E. Somersalo, D. Isaacson, and M. Cheney. A linearized inverse boundary value problem for maxwell's equations. *Journal of computational and applied mathematics*, 42(1):123–136, 1992.

[65] J. Lei, S. Liu, Z .H. Li, and M. Sun. Image reconstruction algorithm based on the extended regularized total least squares method for electrical capacitance tomography. *IET Measurement Science and Technology*, 2(5):326–336, 2008.

[66] N. B. Karayiannis and A. N. Venetsanopoulos. Regularization theory in image restoration-the stabilizing function approach. *IEEE Transactions on Acoustics, Speech and Signal Processing*, 38(7):1155–1179, 1990.

[67] M. Cheney, D. Isaacson, J. C. Newell, S. Simske, and J. Goble. Noser: an algorithm for solving the inverse conductivity problem. *International Journal of Imaging Systems and Technology*, 2(2):66–75, 1990.

[68] D. Calvetti, S. Morigi, L. Reichel, and F. Sgallari. Tikhonov regularization and the l-curve for large discrete ill-posed problems. *Journal of Computational and Applied Mathematics*, 123(1):423–446, 2000.

[69] F. Xu, M. Deshpande, and Y-K. Hue. Iterative nonlinear tikhonov algorithm with constraints for capacitance tomography of two-phase system. *IEEE Journal of Selected Topics in Applied Earth Observations and Remote Sensing*, 5(3):707–716, 2012.

[70] L. Jing, S. Liu, L. Z. Hong, and S. Meng. An image reconstruction algorithm based on the extended tikhonov regularization method for electrical capacitance tomography. *Measurement*, 42(3):368 – 376, 2009.

[71] Z. Liu, X. Y. Tan, and W. Jia. An image reconstruction algorithm based on tikhonov regularization in electromagnetic tomography. In *International Conference on Measuring Technology and Mechatronics Automation*, 2010.

[72] Y. Li and W. Q. Yang. Image reconstruction by non-linear landweber iteration for complicated distributions. *Measurement*, 19:094014, 2008.

[73] W. Q. Yang, D. M. Spink, T. A. York, and H. McCann. An image-reconstruction algorithm based on landweber's iteration method for electrical-capacitance tomography. *Measurement Science and Technology*, 10(11):1065, 1999.

[74] B. Brandstatter, G. Holler, and D. Watzenig. Reconstruction of inhomogeneities in fluids by means of capacitance tomography. *COMPEL: The International Jounal for Computation and Mathematics in Electrical and Electronic Engineering*, 22(3):508–519, 2003.

[75] L. Hu, H. X. Wang, B. Zhao, and W. Q. Yang. A hybrid reconstruction algorithm for electrical impedance tomography. *Measurement Science and Technology*, 18(3):813–818, 2007.

[76] T. Widlak and O. Scherzer. Hybrid tomography for conductivity imaging. *Inverse Problems*, 28:084008, 2012.

[77] M. A. Lukas. Robust generalized cross-validation for choosing the regularization parameter. *Inverse Problems*, 22(5):1883, 2006.

[78] M. A. Lukas. Strong robust generalized cross-validation for choosing the regularization parameter. *Inverse Problems*, 24(3):034006, 2008.

[79] G. H. Golub, M. Heath, and G. Wahba. Generalized cross-validation as a method for choosing a good ridge parameter. *Technometricx*, 21(2):215–223, 1979.

[80] L. O. Scherzer. The use of morzov's discrepancy principle for tikhonov regularisation for solving nonlinear ill-posed problems. *Computing*, 51:45–60, 1993.

[81] Per Christian Hansen. *Rank-deficient and discrete ill-posed problems: numerical aspects of linear inversion*, volume 4. Society for Industrial Mathematics, 1987.

[82] P. C. Hansen, T. Jensen, and G. Rodriguez. An adaptive pruning algorithm for the discrete l-curve criterion. *Journal of Computational and Applied Mathematics*, 198:483–492, 2007.

[83] H.-Y. Wei and M. Soleimani. Hardware and software design for a national instrument-based magnetic induction tomography system for prospective biomedical applications. *Physiological Measurement*, 33(5):863–879, 2012.

[84] H. Y. Wei and M. Soleimani. A magnetic induction tomography system for prospective industrial processing applications. *Chinese Journal of Chemical Engineering*, 20(2):406–410, 2012.

[85] S. Watson, R. J. Williams, H. Griffiths, W. Gough, and A. Morris. Frequency downconversion and phase noise in mit. *Physiological Measurement*, 23:189–194, 2002.

[86] G. M. Lyon, Z. Z. Yu, A. J. Peyton, and M. S. Beck. Developments in electromagnetic tomography instrumentation. *IEE Colloquium on Advances in Electrical Tomography (Digest No: 1196/143)*, 12:1–4, June 1996.

[87] S. Ramli and A. J. Peyton. Feasibility study of planar-array electromagnetic inductance tomography (emt). In *1st World Congress on Industrial Process Tomography*, Buxton, Greater Manchester, April 14-17 1999. 1st World Congress on Industrial Process Tomography, Buxton, Greater Manchester.

[88] H. Scharfetter, P. Brunner, and R. Merwa. Magnetic induction tomography: single-step solution of the 3-d inverse problem for differential image reconstruction. *International Journal of Information and System Science*, 2(4):585–606, 2006.

[89] K. Hollaus, C. Magele, R. Merwa, and H. Scharfetter. Numerical simulation of the eddy current problem in magnetic induction tomography for biomedical applications by edge elements. *IEEE Transactions on Magnetics*, 40(2):623–626, 2004.

[90] A. J. Peyton, R. Mackin, D. Goss, W. A. Wan-daud, E. Crescenzo, N. H. Saunders, and H. S. Tapp. Addressing the difficulties in using inductive methods to evaluating human body compositions. *Proceedings of the international conference on robotics, vision, information and signal processing*, 21(1/2):69–77, 2003.

[91] W. He, H. Luo, Z. Xu, and J. Wang. Multi-channel magnetic induction tomography measurement system. In *3rd International Conference on Biomedical Engineering and Informatics*, volume 1, pages 402–405. IEEE, 2010.

[92] L. Ma, H.-Y. Wei, and M. Soleimani. Cryosurgical monitoring using electromagnetic measurements: A feasibility study for magnetic induction tomography. In *13th International Conference in Electrical Impedance Tomography*, Tianjin University, Tianjin., 2012-05-23 - 2012-05-25 2012.

[93] W. Yin, G. Chen, L. Chen, and W. Mi. The design of a digital magnetic induction tomography (mit) system for metallic object imaging on half cycle demodulation. *IEEE Sensors Journal*, 11:2233–2240, 2011.

[94] D. Gursoy and H. Scharfetter. Optimum receiver array design for magnetic induction tomography. *IEEE Transactions on Biomedical Engineering*, 56(5):1435–1441, 2009.

[95] H. Y. Wei and M. Soleimani. Theoretical and experimental evaluation of rotational magnetic induction tomography. *IEEE Transactions on Instrumentation and Measurement*, pp:1–8, 2012.

[96] H. Y. Wei, L. Ma, and M. Soleimani. Volumetric magnetic induction tomography. *Measurement Science and Technology*, 23(5):055401, 2012.

[97] H. Y. Wei and M. Soleimani. Four dimensional reconstruction using magnetic induction tomography: experimental study. *Progress In Electromagnetics Research*, 129:17–32, 2012.

[98] D. Russell and V. Shen. Increased use of remote field technology for in-line inspection of pipelines proves the value of the technology for this application. In *17th World Conference on Nondestructive Testing*, Shanghai, China, 25-28 Oct 2008.

[99] J. Garcia-Martin, J. Gomez-Gil, and E. Vazquez-Sanchez. Non-destructive techniques based on eddy current testing. *Sensors*, 11(3):2525–2565, 2011.

[100] M. Bohacova. Methodology of short fatigue crack detection by the eddy current method in a multi-layered metal aircraft structure. *Engineering Failure Analysis*, 35:597–608, 2013.

[101] D. Placko, T. Bore, and A. Rivollet. Imaging and detection of cracks in metallic structures with eddy current sensors. In *SPIE Smart Structures and Materials + Nondestructive Evaluation and Health Monitoring*, page 86941Y, 2013.

[102] C. Yu, X. Jiang, and D. Zhang. An eddy current sensor array to detect defects on a metal surface. *Advanced Materials Research*, 503-504:1243–1246, 2012.

[103] D. J. Sadler and C. H. Ahn. On-chip eddy current sensor for proximity sensing and crack detection. *Sensors and Actuators A: Physical*, 91(3):340–345, 2001.

[104] A. Washabaugh, S. Haque, D. Jablonski, and N. J. Goldfine. Eddy current sensor arrays for pipeline inspection with and without ccusensor. In *8th International Pipeline Conference*, volume 1, pages 539–548, Calgary, CANADA, 2010.

[105] H. Almostaneer, Z. S. Jones, S. Liu, and D. L. Olson. In-situ repairs of pipelines using metal arc welding under oil (maw-uo) aided by eddy current crack detection. In *AIP Conference Proceedings, Review of Progress in Quantitative Nondestructive Evaluation*, volume 1430, pages 1243–1250, 2012.

[106] T. Takagi, H. Y. Huang, H. Fukutomi, and J. J. Tani. Numerical evaluation of correlation between crack size and eddy current testing signal by a very fast simulator. *IEEE Transactions on Magnetics*, 34(5):2581–2584, 1998.

[107] Z. Y. Xu, X. J. Wu, J. Li, and Y. H. Kang. Assessment of wall thinning in insulated ferromagnetic pipes using the time-to-peak of differential pulsed eddy-current testing signals. *NDT& E International*, 51:24 – 29, 2012.

[108] M. Rourke, Y. Li, and G. Roberts. Multi-tubular corrosion inspection using a pulsed eddy current logging tool. In *International Petroleum Technology Conference*, volume 2, pages 1667–1672, 2013. cited By (since 1996)0.

[109] B. Lebrun, Y. Jayet, and J-C. Baboux. Pulsed eddy current signal analysis: application to the experimental detection and characterization of deep flaws in highly conductive materials. *NDT&E International*, 30(3):163–170, 1997.

[110] Y. Li, L. Udpa, and S. S. Udpa. Three-dimensional defect reconstruction from eddy-current nde signals using a genetic local search algorithm. *IEEE Transactions on Magnetics*, 40(2):410–417, 2004.

[111] M. Afzal and S. Udpa. Advanced signal processing of magnetic flux leakage data obtained from seamless gas pipeline. *NDT&E International*, 35:449–457, 2002.

[112] Y. Li, J. Wilson, and G. Y. Tian. Experiment and simulation study of 3d magnetic field sensing for magnetic flux leakage defect characterization. *NDT& E International*, 40:179–184, 2007.

[113] M. R. Kandroodi, B. N. Araabi, M. N. Ahmadabadi, F. Shirani, and M. M. Bassiri. Detection of natural gas pipeline defects using magnetic flux leakage measurements. In *21st Iranian Conference on Electrical Engineering*, 2013. cited By (since 1996)0.

[114] R. Pohl, A. Erhard, H. J. Montag, H. M. Thomas, and H. W. Stenberg. Ndt techniques for railroad wheel and gauge corner inspection. *NDT&E International*, 37(2):89–94, 2004.

[115] J. C. Drury and A. Marino. A comparison of the magnetic flux leakage and ultrasonic methods in the detection and measurement of corrosion pitting in ferrous plate and pipe. In *Proceedings 15th World Conference on Nondestructive Testing*, 2000.

[116] Q. Song, J. Shuai, X. Wang, and J. Gong. Tridimensional magnetic field analysis for magnetic flux leakage defect characterization. *Advanced Science Letters*, 19(8):2277–2281, 2013.

[117] M. Salama, B. Nestleroth, M. Maes, C. Rodriguez, and D. C. Blumer. Characterization of the accuracy of the mfl pipeline inspection tools. In *Proceedings of the International Conference on Offshore Mechanics and Arctic Engineering*, volume 6, pages 247–251, 2012.

[118] H. S. Khatak and Baldev Raj. *Corrosion of Austenitic Stainless Steel: Mechanism, Mitigation and Monitoring*. Alpha Science International Ltd., 2002.

[119] D. Kim, L. Udpa, and S. Udpa. Remote field eddy current testing for detection of stress corrosion cracks in gas transmission pipelines. *Materials Letters*, 58(15):2102–2104, 2004.

[120] D. Robinson. Identification and sizing of defects in metallic pipes by remote field eddy current inspection. *Tunnelling and Underground Space Technology*, 13, Supplement 2(0):17 27, 1998.

[121] G. L. Burkhardt, T. H. Goyen, A. J. Parvin, R. H. Peterson, and R. F. Tennis. Remote-field eddy current inspection tool for small-diamater unpiggable pipelines. In *IPC2008: Proceedings of the the ASME international pipeline conference-2008*, volume 2, pages 41–44, Calgary, CANADA, 2008.

[122] L. Morgan. The performance of automated ultrasonic testing (aut) of mechanised pipeline girth welds. In *8th ECNDT Proceedings European Conference on Nondestructive Testing Barcelona*, Spain, June 17-21 2002.

[123] E. Ginzel, R. Ginzel, B. Gross, M. Hoff, and P. Manuel. Developments in ultrasonic inspection for total inspection of pipeline girth welds. In *8th Symposium on Pipeline Research*, Houston, Texas, August 1993.

[124] J. Bowers and E. Warren. The application of automatic ultrasonic (aut) inspection for subsea pipelines. In *24th Offshore Pipeline Technology Conference*, Amsterdam, Febuary 2001.

[125] L. H. Lee, R. Rajkumar, L. H. Lo, C. H. Wan, and D. Isa. Oil and gas pipeline failure prediction system using long range ultrasonic transducers and euclidean-support vector machines classification approach. *Expert Systems with Applications*, 40(6):1925 – 1934, 2013.

[126] S. Y. Jing and D. Bo. Research on ultrasonic guided wave testing pipeline corrosion based on wavelet transform. In *25th Chinese Control and Decision Conference*, pages 2802–2805, 2013.

[127] S. B. Krasilnikov and G. I. Sonin. X-ray radiometric inspection of circumferential welded joints in the construction of transmission gas pipelines. *Welding International*, 22(8):570–574, 2008.

[128] X. Zhang, J. Li, and H. Chen. Visual feature recognition of an x-ray based inspection pipeline robot. In *International Conference on Control and Automation*, pages 966–970, 2005.

[129] W. Chen, Z. Miao, and D. Ming. Automated inspection using x-ray imaging. In *IEEE 10th International Conference on Trust, Security and Privacy in Computing and Communications*, pages 1769–1772, 2011.

[130] P. S. Ong, W. L. Anderson, B. D. Cook, and R. Subramanyan. A novel x-ray technique for inspection of steel pipes. *Journal of Nondestructive Evaluation*, 13(4):165–173, 1994.

[131] Z. Deng, F. Xu, X. Zhang, and H. Chen. Key techniques of the x-ray inspection real-time imaging pipeline robot. *High Technology Letters*, 10(2):54–56, 2004.

[132] I. J. Munns and G. A. Georgiou. Ultrasonic and radiographic ndt of butt fusion welded polyethylene pipes. *Insight*, 41(5), 1999.

[133] D. Janda, C. Baet, and L. Bortels. A new approach to pipeline integrity - combining in-line inspection and cathodic protection simulation technology. *NACE - International Corrosion Conference Series*, 2013.

[134] W. R. B. Lionheart. Reconstruction algorithms for permittivity and conductivity imaging (key note). In *Proceedings of the 2nd World Congress on Industrial Process Tomography*, Hannover, Germany, August 2001.

[135] R. D. Adams and P. Cawley. A review of defect types and nondestructive testing techniques for composites and bonded joints. *NDT International*, 21(4):208–222, 1988.

[136] C. C. H. Guyotta, P. Cawleya, and R. D. Adamsb. The non-destructive testing of adhesively bonded structure: a review. *The Journal of Adhesion*, 20(2):129–159, 1986.

[137] D. E. W. Stone and B. Clarke. Ultrasonic attenuation as a measure of void content in carbon-fibre reinforced plastics. *Non-Destructive Testing*, 8:137–145, 1975.

[138] J. L. Rose, M. J. Avioli, and R. Bilgram. A feasibility study on the nondestructive evaluation of an adhesively bonded metal to metal bond: an ultrasonic pulse echo approach. *British Journal of Non-destructive Testing*, 25:67–71, 1983.

[139] S. Yashiro, J. Takatsubo, N. Toyama, T. Okabe, and N. Takeda. Delamination detection in holed cfrp laminates using visualized ultrasound propagation. *Transactions of the Japan Society of Mechanical Engineers Series A*, 72(12):1882–1887, 2006.

[140] A. Diaz, M. Guizar-Sicairos, A. Poeppel, A. Menzel, and O. Bunk. Characterization of carbon fibers using x-ray phase nanotomography. *Carbon*, 67:98–103, 2014.

[141] D. J. Bull, L. Helfen, I. Sinclair, S. M. Spearing, and T. Baumbach. A comparison of multi-scale 3d x-ray tomographic inspection techniques for assessing carbon fibre composite impact damage. *Composites Science and Technology*, 75:55–61, 2013.

[142] U. Hassler, M. Rehak, and R. Hanke. Carbon fibre preform inspection by circular x-ray tomosynthesis. *IEEE Nuclear Science Symposium Conference Record*, pages 590–592, 2008.

[143] S. A. Grammatikos, E. Z. Kordatos, T. E. Matikas, C. David, and A. S. Paipetis. Current injection phase thermography for low-velocity impact damage identification in composite laminates. *Materials and Design*, 55:429–441, 2014.

[144] G. Zauner, G. Mayr, and G. Hendorfer. Comparative defect evaluation of aircraft components by active thermography. In *Image Processing: Machine Vision Applications II*, volume 7251, 2009.

[145] M. P. De Goeje and K. E. D. Wapenaar. Non-destructive inspection of carbon fibre-reinforced plastics using eddy current methods. *Composites*, 23(3):147 – 157, 1992.

[146] H. Heuer, M. H. Schulze, and N. Meyendorf. High resolution inspection of carbon fiber materials by eddy current techniques. *2nd International Symposium on NDT in Aerospace*, Mo.2.A.3:1–13, 2010.

[147] M. H. Schulze, H. H. Heuer, M. Kuttner, and N. Meyendorf. High-resolution eddy current sensor system for quality assessment of carbon fiber materials. *Microsystem Technologies*, 16(5):791–797, 2010.

[148] K. Koyama, H. Hoshikawa, and G. Kojima. Eddy current nondestructive testing for carbon fiber-reinforced composites. *Journal of Pressure Vessel Technology, Transactions of the ASME*, 135(4):041501–041505, 2013.

[149] G. Mook, R. Lange, and O. Koeser. Non-destructive characterisation of carbon-fiber-reinforced plastic by means of eddy-currents. *Composites Science and Technology*, 61:865–873, 2001.

[150] A. Baltopoulos, N. Polydorides, L. Pambaguian, A. Vavouliotis, and V. Kostopoulos. Damage identification in carbon fiber reinforced polymer plates using electrical resistance tomography mapping. *Jounal of composites materials*, 47(26):3285–3301, 2012.

[151] B. R. Loyola, T. M. Briggs, L. Arronche, K. J. Loh, V. L. Saponara, G. O'Bryan, and J. L. Skinner. Detection of spatially distributed damage in fiber-reinforced polymer composites. *Structural Health Monitoring*, 12(3):225–239, 2013.

[152] R. Schueler, S. P. Joshi, and K. Schulte. Damage detection in cfrp by electrical conductivity mapping. *Composites science and technology*, 61:921–930, 2001.

[153] A. Renner, W.-J. Fischer, and U. Marschner. A new imaging approach for in-situ and ex-situ inspections of conductive fiber reinforced composites by magnetic induction tomography (mit). *Journal of Intelligent Material Systems and Structures*, 25(9):1149–1162, 2014.

[154] M. Soleimani. Improving the temporal resolution of magnetic induction tomography for molten metal flow visualization. *IEEE Transactions on Instrumentation and Measurement*, 59(3):553–557, 2010.

[155] R. Casanas, H. Scharfetter, A. Altes, A. Remacha, P. Sarda, J. Sierra, R. Merwa, K. Hollaus, and J. Rosell. Measurement of liver iron overload by magnetic induction using a planar gradiometer: preliminary human results. *Physiological measurement*, 25(1):315, 2004.

[156] L. Janousek. Influence of selected parameters on eddy currents attenuation in nondestructive inspection. *Komunikacie*, 15(2A):102–106, 2013.

[157] D. Gursoy and H. Scharfetter. Imaging artifacts in magnetic induction tomography caused by the structural incorrectness of the sensor model. *Measurement Science and Technology*, 22(1):015502, 2011.

[158] R. Merwa and H. Scharfetter. Magnetic induction tomography: evaluation of the point-spread-function and analysis of resolution and image distortion. *Physiological measurement*, 28:313–324, 2007.

[159] L. Ma, H.-Y. Wei, and M. Soleimani. Planar magnetic induction tomography for 3d near subsurface imaging. *Progress In Electromagnetics Research*, 138:65–82, 2013.

[160] A. Todoroki. Skin effect of alternating electric current on laminated cfrp. *Advanced Composite Materials*, 21(5-6):477–489, 2012.

[161] T. A. Ezquerra, M. T. Connor, S. Roy, M. Kulescza, J. Fernandes-Nascimento, and F. J. Balta-Calleja. Alternating-current electrical properties of graphite, carbon-black and carbon-fiber polymeric composites. *Composites Science and Technology*, 61:903–909, 2001.

[162] L. Ma, H. Y. Wei, and M. Soleimani. Pipeline inspection using magnetic induction tomography based on a narrowband pass filtering method. *Progress In Electromagnetics Research M*, 23:65–78, 2012.

[163] S. C. Mukhopadhyay. Quality inspection of electroplated materials using planar type micromagnetic sensors with post processing from neural network model. *IEE Proceedings Science, Measurement and Technology*, 149:165–171, 2002.

[164] S. C. Mukhopadhyay. Saxophone reed inspection employing planar electromagnetic sensors. *IEEE Transactions on Instrumentation and Measurement*, 56(6):2492–2503, 2007.

[165] S. C. Mukhopadhyay. A novel planar mesh-type microelectromagnetic sensor. part i. model formulation. *IEEE Sensors Journal*, 4(3):301–307, 2004.

[166] S. C. Mukhopadhyay, C. P. Gooneratne, S. Demidenko, and G. S. Gupta. Low cost sensing system for dairy products quality monitoring. In *Proceedings of the IEEE Instrumentation and Measurement Technology Conference*, volume 1, pages 244–249. IEEE, 2005.

[167] W. Yin and A. J. Peyton. A planar emt system for the detection of faults on thin metallic plates. *Physiological Measurement*, 17(8):2130–2135, 2006.

[168] M. R. Hajihashemi and M. El-Shenawee. Inverse scattering of three-dimensional pec objects using the level-set method. *Progress In Electromagnetics Research*, 116:23–47, 2011.

[169] W.-K. Park. On the imaging of thin dielectric inclusions via topological derivative concept. *Progress In Electromagnetics Research*, 110:237–252, 2010.

[170] R. Banasiak, Z. Ye, and M. Soleimani. Improving three-dimensional electrical capacitance tomography imaging using approximation error model theory. *Journal of Electromagnetic Waves and Applications*, 23(2-3):411–421(11), 2012.

[171] S. A. AlShehri, S. Khatun, A. B. Jantan, R. S. A. Raj Abdullah, R. Mahmood, and Z. Awang. 3d experimental detection and discrimination of malignant and benign breast tumor using nn-based uwb imaging system. *Progress In Electromagnetics Research*, 116:221–237, 2011.

[172] S. Ren, W. Chang, T. Jin, and Z. Wang. Automated sar reference image preparation for navigation. *Progress In Electromagnetics Research*, 121:535–555, 2011.

[173] S. J. Wei, X. L. Zhang, J. Shi, and G. Xiang. Sparse reconstruction for sar imaging based on compressed sensing. *Progress In Electromagnetics Research*, 109:63–81, 2010.

[174] Y. L. Chang, C. Y. Chiang, and K. S. Chen. Sar image simulation with application to target recognition. *Progress In Electromagnetics Research*, 119:35–57, 2011.

[175] O. Dorn, H. Bertete-Aguirre, J. G. Berryman, and G. C. Papanicolaou. A nonlinear inversion method for 3d-electromagnetic imaging using adjoint fields. In *Inverse Problems*, pages 1523–1558, 1999.

[176] A. Adler, J. H. Arnold, R. Bayford, A. Borsic, B. Brwon, P. Dixon, T. J. C. Faes, I. Frerichs, H. Gagnon, Y. Garbr, B. Grychtol, G. Hahn, W. R. B. Lionheart, A. Malik, R. P. Patterson, J. Stocks, A. Tizzard, N. Weiler, and G. K. Wolf. Greit: a unified approach to 2d linear eit reconstruction of lung images. *Physiological Measurement*, 30:S33–S55, 2009.

[177] L. Ma and M. Soleimani. Limited angle and limited data electromagnetic induction tomography: experimental evaluation of the effect of missing data. *Measurement Science and Technology*, 23(12):125406, 2012.

[178] L. Ma and M. Soleimani. Electromagnetic imaging for internal and external inspection of metallic pipes. *Insight-Non-Destructive Testing and Condition Monitoring*, 54(9):493–495, 2012.

[179] M. Soleimani, H. G. Wang, Y. Li, and W. Q. Yang. A comparative study of 3d electrical capacitance tomographic. *International Journal of Information and System Sciences*, 3(2):292–306, 2007.

[180] H. Scharfetter, K. Hollaus, J. Rosell, and R. Merwa. Single step 3-d image reconstruction in magnetic induction tomography: theoretical limits of spatial resolution and contrast to noise ratio. *Annals of Biomedical Engineering*, 34:1786–1798, 2006.

[181] G. A. Oldenborger and P. S. Routh. The point-spread function measure of resolution for the 3-d electrical resistivity experiment. *Geophysical Journal International*, 176:405–414, 2009.

[182] A. Javaherian and M. Soleimani. Compressed sampling for boundary measurements in three-dimensional electrical impedance tomography. *Physiological Measurement*, 34:1133–1149, 2013.

[183] W. Daily and A. Ramirez. Environmental process tomography in the united states. *The Chemical Engineering Journal and the Biochemical Engineering Journal*, 56(3):159 – 165, 1995.

[184] J. Rosell-Ferrer, R. Merwa, P. Brunner, and H. Scharfetter. A multifrequency magnetic induction tomography system using planar gradiometers: data collection and calibration. *Physiological Measurement*, 27:S271–S280, 2006.

[185] H. Scharfetter, H. K. Lackner, and J. Rosell. Magnetic induction tomography: hardware for multi-frequency in biological tissue. *Physiological Measurement*, 22(1):131–146, 2001.

[186] A. V. Korzhenevsky and S. A. Sapetsky. Visualization of the internal structure of extended conducting objects by magnetoinduction tomography. *Magnetoinduction tomography Bull. Russian Academy of Sciences Physics*, 65:1945–1949, 2001.

[187] B. U. Karbeyaz and N. G. Gencer. Electricalconductivity imaging via contactless measurements: an experimental study. *IEEE Transactions on Medical Imaging*, 22:627–635, 2003.

[188] C. H. Igney, S. Watson, R. J. Williams, H. Griffiths, and O. Dossel. Design and performance of a planar-array mit system with normal sensor alignment. *Physiological Measurement*, 26:S263–S278, 2005.

[189] S. Watson, A. Morris, R. J. Williams, W. Gough, and H. Griffiths. The cardiff magnetic induction tomography system. In *Proceedings of the International Federation for Medical and Biological Engineering EMBEC 02 Part 1*, page 116, Vienna, Austria., December 04-08 2002.

[190] N. G. Gencer and M. N. Tek. Imaging tissue conductivity via contactless measurements: a feasibility study. *Elektrik*, 6(3):183–200, 1998.

[191] H. Jin, Y. Lian, S. Yang, G. He, and G. Guo. The parameters measurement of air-water two phase flow using the electrical resistance tomography (ert) technique in a bubble column. *Special Issue IWPT-4 in Flow Measurement and Instrumentation*, 31:55–60, 2013.

[192] L. Su, Z.-P. Song, B.-S. Wang, and L. Ding. Research on void fraction of gas-liquid two-phase flow based on comsol and matlab. *Journal of Ship Mechanics*, 17(5):460–467, 2013.

[193] J. Zhang and F. Ma. Application of electrical resistance tomography to ice-water two-phase flow parameters measurement. *Key Engineering Materials*, 562-565:686–690, 2013.

[194] N. Terzija, W. Yin, G. Gerbeth, F. Stefani, K. Timmel, T. Wondrak, and A. J. Peyton. Use of electromagnetic induction tomography for monitoring liquid metal/gas flow rregime on a model of an industrial steel caster. *Measurement Science and Technology*, 22:015501, 2011.

[195] R. Thorn, G. A. Johansen, and B. T. Hjertaker. Three-phase flow measurement in the petroleum industry. *Measurement Science and Technology*, 24:012003, 2013.

[196] M. Zhang, L. Ma, and M. Soleimani. Magnetic induction tomography guided electrical capacitance tomography imaging with grounded conductors. *Measurement*, 53:171–181, 2014.

[197] R. A. Albrechtsen, Z. Z. Yu, and A. J. Peyton. Preliminary experiments on the investigation of the inductive technique for measuring water content in multiphase flow. In *Proc. ECAPT*, pages 205–213, Bergen, 1995.

[198] E. A. Hammer and G. Fossdal. A new water-in-oil monitor based on high frequency magnetic field excitation. In *Proceedings of the 2nd international symposium on process tomography*, pages 9–16, Wroclaw, Poland, 2002.

[199] Z. Liu, M. He, and H.-L. Xiong. Simulation study of the sensing field in electromagnetic tomography for two-phase flow measurement. *Flow Measurement and Instrumentation*, 16(2):199 – 204, 2005.

[200] S. Watson, R. J. Williams, W. Gough, and H. Griffiths. A magnetic induction tomography system for samples with conductivities below 10 s/m. *Measurement Science and Technology*, 19(4):045501, 2008.

[201] H. Y. Wei and M. Soleimani. Two-phase low conductivity flow imaging using magnetic induction tomography. *Progress In Electromagnetics Research*, 131:97–115, 2012.

[202] J. T. Sun and W. Q. Yang. Fringe effect of electrical capacitance and resistance tomography sensors. *Measurement Science and Technology*, 24(7):074002, 2013.

[203] M. Vauhkonen, M. Hamsch, and C. H. Igney. Image reconstruction approaches for philips magnetic induction tomograph. In *IFMBE Proceedings:13th International Conference on Electrical Bioimpedance and the 8th Conference on Electrical Impedance Tomography*, volume 17, 2007.

[204] A. Borsic, E. A. Attardo, and R. J. Halter. Multi-gpu jacobian accelerated computing for soft field tomography. *Physiological Measurements*, 33:1703–1715, 2012.

[205] R. S. Tavares, T. C. Martins, and M. S. G. Tsuzuki. Electrical impedance tomography reconstruction through simulated annealing using a new outside-in heuristic and gpu parallelization. *Journal of Physics Conference Series*, 407(Conference 1):012015, 2012.

[206] P. Kapusta, M. Majchrowicz, D. Sankowski, and R. Banasiak. Application of gpu parallel computing for acceleration of finite element method based 3d reconstruction algorithms in electrical capacitance tomography. *Image Processing and Communications*, 17(4):339–346, 2013.

[207] Y. Maimaitijiang, M. A. Roula, S. Watson, R. Patz, R. J. Williams, and H. Griffiths. Parallelization methods for implementation of a magnetic induction tomography forward model in symmetric multiprocessor systems. *Parallel Computing*, 34(9):497 – 507, 2008.

[208] Y. Maimaitijiang, M. A. Roula, S. Watson, G. Meriadec, K. Sobaihi, and R. J. Williams. Evaluation of parallel accelerators for high performance image reconstruction for magnetic induction tomography. *Journal of Selected Areas in Software Engineering*, 1-7, January Edition 2011.

[209] D. Goss, R. O. Mackin, E. Crescenzo, H. S. Tapp, and A. J. Peyton. Understanding the coupling mechanisms in high frequency emt. In *3rd World Congress on Industrial Process Tomography*, pages 364–369, Banff, Canada, September 2003.

[210] H. Griffiths, M. Zolgharni, P. D. Ledger, and S. Watson. The cardiff mk2b mit head array: optimising the coil configuration. In *Journal of Physics: International Conference on Electrical Bioimpedance*, volume Conference Series 224, page 012046, 2010.

[211] S. Watson, C. H. Igney, O. Dossel, R. J. Williams, and H. Griffiths. A comparison of sensors for minimizing the primary signal in planar-array magnetic induction tomography. *Physiological Measurement*, 26:1–13, 2005.

[212] R. Merwa and H. Scharfetter. Magnetic inductiontomography: the influence of the coil configuration on the spatial resolution. In *13th International Conference on Electrical Bioimpedance and the 8th Conference on Electrical Impedance Tomography IFMBE Proceedings*, volume 17, pages 456–459, 2007.

[213] H. Scharfetter, R. Merwa, and K. Pilz. A new type of gradiometer for the receiving circuit of magnetic induction tomography (mit). *Physiological Measurement*, 26:S307–S318, 2005.

[214] C. H. Riedel, M. Keppelen, S. Nani, R. D. Merges, and O. Dossel. Planar system for magnetic induction conductivity measurement using a sensor matrix. *Physiological measurement*, 25:403–411, 2004.

[215] M. D. V. Hari Kishore, B. N. Singh, and M. K. Panditbr. Nonlinear static analysis of smart laminated composite plate. *Aerospace Science and Technology*, 15(3):224–235, 2011.

[216] B. M. Kolundzija. Electromagnetic modeling of composite metallic and dielectric structures. *IEEE Transactions on Microwave Theory and Techniques*, 47:1021–1032, 1999.